UNIVERSITY OF CALIFORNIA
Santa Barbara

A Search for Resonant Z Pair Production

A dissertation submitted in partial satisfaction
of the requirements for the degree of

Doctor of Philosophy

in

Physics

by

Antonio Boveia

Committee in Charge:

Professor David Stuart, Chair

Professor Claudio Campagnari

Professor Mark Srednicki

December 2008

The dissertation of
Antonio Boveia is approved:

Professor Claudio Campagnari

Professor Mark Srednicki

Professor David Stuart, Committee Chairperson

December 2008

A Search for Resonant Z Pair Production

by

Antonio Boveia

Curriculum Vitae

Antonio Boveia

Education

2004–2008 Ph.D. in Physics, University of California, Santa Barbara

2001–2004 M.A. in Physics, University of California, Santa Barbara

1997–2001 B.S. in Physics, Mathematics, and Astronomy,
summa cum laude, Phi Beta Kappa, University of Iowa

Selected Publications

· *Search for New Heavy Particles Decaying to $ZZ \to eeee$ in $p\bar{p}$ Collisions at $\sqrt{s} = 1.96$ TeV*, Phys. Rev. D **78** 012008 (2008).

· *Status and Performance of the CDF Run II Silicon Detector*, PoS **HEP2005** 377 (2006).

· *Chiral Supergravitons Interacting with a 0-Brane N-Extended NSR Super-Virasoro Group*, Phys. Lett. B **529** 222-232 (2002).

Professional Employment

· 2003–2008: Research Assistant, Prof. David Stuart, Department of Physics, UC Santa Barbara.

· 2001–2003: Teaching Assistant, Department of Physics, UC Santa Barbara.

Awards and Honors

· Outstanding Teaching Assistant (single award), UCSB Physics Dept., 2002-2003

· James A. Van Allen Award, 2001

· Stevens Phi Beta Kappa Scholarship, 2000-2001

· Waldo Edward and Martha Althaus Smith Award, 2000

· Phi Beta Kappa (Junior Election), Spring 2000

Acknowledgements

I thank my committee for reviewing this thesis, the DOE and taxpayers for financial support, and the CDF Collaboration for building both a terrific detector and a lively and comfortable home for it. For his patience, guidance, and perspective, my advisor David Stuart deserves most of the credit and none of the blame for my work.

I also owe thanks to my brother Joe and to my parents, Gary and Beverly, for three decades of encouragement and support—and for a work ethic that I hope shows through this hastily-written document.

Most importantly, I'm grateful to Dana, for waiting so long.

Of course, I've incurred debts to many, many other people to get here.

From Santa Barbara, I thank Mark Srednicki, Claudio Campagnari, Gary Horowitz, Jim Hartle, and Joe Incadela for very memorable classes; Ben Brau for many years of invaluable advice at all stages of this work; Chris Hill, Slava Krutelyov, Victor Pavlunin, Cigdem Issever, Maria Spiropulu, Adam Scott, Corrinne Mills, and Ford Garberson for discussions and advice; and, among others, Gus Bosse, Tae Min Hong, Mike Hermele, Dave Wood, Jing Xu, Henriette Elvang, and Eric Luckwald for entertaining distractions.

From CDF, the only way to be sure I haven't forgotten anyone would be to include the entire author list. Aseet Mukherjee, Matt Herndon, Rainer Wallny, Mircea Coca, Chris Hays, Pasha Murat, Rick Snider, Tom Phillips, Ashutosh Kotwal, Paolo Mastrandrea, Bo-Young Han, Jiyeon Han, Giorgio Chiarelli, Oliver Stelzer-Chilton, Ulrich Husemann, Song Ming Wang, and Doug Glenzinski gave crucial feedback during my tracking work, and many of them helped put together the new tracking software used here. Monica D'Onofrio, Conor Henderson, Aron Soha, Eiko Yu, Sasha Pronko, and the rest of the Exotics group provided helpful criticism of my ZZ analysis. All participants in silicon operations helped to provide vital data for the depletion voltage studies, and I thank Rick Tesarek and Steve Worm for their input, Marcel Stanitzki for opportunities to show the results, and Oscar González and Roberto Martinez

Ballarin for continuing the analysis. I add David Clark and Ankush Mitra to thank for the massive amounts of coffee; Aart Heijboer and Burkard Reisert for the occasional movies; Steve Hahn, Larry Nodulman, Ben Kilminster, Jared Yamaoka, Andy Hocker, and Louise Oakes for the musical interludes; and Ted Liu, Vadim Rusu, Tom Wright, Jaco Konigsberg, Ingyin Zaw, Jason Nielsen, Rob Roser, Elliot Lipeles, Angela Wyatt, Beate Heinemann, and Avi Yagil for some particularly influential conversations.

Abstract

A Search for Resonant Z Pair Production

Antonio Boveia

I describe a search for anomalous production of Z pairs through a new massive resonance X in 2.5–2.9 fb^{-1} of $p\bar{p}$ collisions at $\sqrt{s} = 1.96$ TeV using the CDFII Detector at the Fermilab Tevatron. I reconstruct Z pairs through their decays to electrons, muons, and quarks. To achieve perhaps the most efficient lepton reconstruction ever used at CDF, I apply a thorough understanding of the detector and new reconstruction software heavily revised for this purpose. In particular, I have designed and employ new general-purpose algorithms for tracking at large η in order to increase muon acceptance. Upon analyzing the unblinded signal samples, I observe no $X \to ZZ$ candidates and set upper limits on the production cross section using a Kaluza-Klein graviton-like acceptance.

Contents

1 Introduction **1**

2 The Standard Model **4**
2.1 Z bosons . . . 6
2.2 ZZ production . . . 8
2.3 Electrons and muons at high energy . . . 9
2.4 Jets and the strong interaction . . . 10
2.5 New physics in the ZZ sector? . . . 12

3 Randall-Sundrum scenarios **19**
3.1 RS gravitons at the Tevatron . . . 22

4 The CDF experiment **26**
4.1 The accelerator . . . 26
4.2 Overview of the CDF Detector . . . 28
4.3 Contributions to detector operations . . . 30
4.4 Track reconstruction and contributions . . . 32
4.5 "Backward" tracking . . . 36
4.6 Other tracking contributions . . . 45

5 Search for $X \to ZZ$ **48**
5.1 Outline of method . . . 48
5.2 Data samples . . . 50
5.2.1 Triggers . . . 50
5.2.2 Data quality requirements and luminosity . . . 54
5.2.3 Simulated samples . . . 55
5.3 Data reprocessing . . . 62
5.4 Lepton and jet selection . . . 65

5.4.1 Electron ID . . . 67
5.4.2 Muon ID . . . 73
5.4.3 Lepton selection comparison . . . 86
5.4.4 Jet ID . . . 90
5.5 Energy corrections . . . 91
5.6 Z and X construction . . . 96
5.6.1 Cosmic removal . . . 98
5.6.2 Z cross section measurement . . . 100
5.6.3 Examination of low M_X control regions . . . 120
5.7 Background estimation . . . 121
5.7.1 Four-lepton non-resonant background estimate . . . 121
5.7.2 Four-lepton background cross checks . . . 139
5.7.3 Dijet non-resonant background estimate . . . 143
5.7.4 Background summary . . . 158
5.8 Expected limits . . . 164
5.9 Observed limits . . . 171
5.9.1 Investigation of signal candidates . . . 188

6 Conclusion **199**

Bibliography **201**

Chapter 1

Introduction

Our best description of nature is the Standard Model (SM), a quantum field theory built on $SU(3) \times SU(2) \times U(1)$ gauge invariance and a puzzling concoction of quarks, leptons, and bosons. That is, to explain a century of experiments, we've carefully pieced together a empirical model, consisting of the particles we find in the laboratory, a set of rules for how they interact, and a toolbox of techniques for calculating its predictions. The model has explained the results of nearly every experiment done by a generation of particle physicists [1, 2]. However, it does not incorporate gravity, and it does not explain dark matter or dark energy, or the abundance of matter and inabundance of antimatter. Many aspects of it seem ad hoc or otherwise "inelegant," such as its cocktail of particles and gauge symmetries and their relationships. Most importantly, the mechanism

for breaking its electroweak symmetry is unconfirmed; this depends on a "Higgs" particle which has not yet been observed.

Attempts to extend the theory tend to focus on solutions to one or more of these problems, postulating new phenomena beyond (and often just beyond) the boundaries of the experimental data in order to regulate unwanted behavior or introduce more "elegant," preferred behavior. One can then develop tests for these new phenomena that may support or contradict the extension.

Rather than look to confirm or refute a specific extension or otherwise begin with theoretical motivations, as is the most often-used approach, I choose to search for experimental evidence that could further development of the Standard Model by providing new phenomena to explain. This thesis describes a test of the SM for which exploring far in one direction is possible, provided certain experimental problems can be solved: the $q\bar{q} \rightarrow ZZ$ process at the highest center of mass energies presently reachable, 1.96 TeV at the Fermilab Tevatron. Here, the Standard Model predicts a very low rate and a broad, non-resonant mass spectrum for ZZ pair production. Because of the low rate, the prediction has only been tested near the ≈ 180 GeV pair production threshold. At higher ZZ masses, both the diboson prediction and experimental backgrounds become negligible. One might then discover a new heavy particle decaying to ZZ with only a few candidates.

I search for this evidence of one or more narrow ZZ mass resonances via the Z boson decays to electrons, muons, or jets at the Collider Detector at Fermilab (CDF). While others at CDF have sought similar signatures, such as the lower-mass SM ZZ process, I achieve greater sensitivity by reoptimization of the established techniques for reconstructing leptons, including development of new charged particle tracking algorithms and of new methods for lepton identification and background estimation.

I begin with a review of the Standard Model and of its widely-recognized problems in Chapter 2. Chapter 3 discusses a specific class of extensions to the model, "Randall-Sundrum" scenarios, which could contribute to the ZZ mass spectrum. Chapter 4 describes the experimental apparatus and my contributions to it. Chapter 5 describes the search, and Chapter 6 summarizes the results.

Chapter 2

The Standard Model

The theory of the electroweak forces and the theory of quantum chromodynamics, together called "the Standard Model," consists of a set of fundamental spin-1/2 fermions and a set of spin-1 gauge bosons detected or inferred from fermion scattering experiments, plus a spin-0 "Higgs" boson to generate a mass for each particle. While it is often epistemically or pedagogically useful to focus on the completed model in its modern, refined form, it is also important to remember that the discovery process was very messy and long. The fermions in the model were uncovered over a century of confusing and contradictory experiments:

- the negatively-charged electron (1897) [3, 4], and the oppositely-charged positron (1932) [5].

- a similar but heavier muon (1937) [6] and anti-muon.
- another similar but much heavier tau (1975) [7] and anti-tau.
- six corresponding charge-neutral neutrinos, with crucial first observations in 1956 [8], 1962 [9], and 2000 [10].
- six quarks [11, 12, 13]: u, d, s, c, b, and t.

Groupings containing a negatively-charged lepton (the electron-like particles), its positively-charged partner, and the two related neutrinos are now termed "generations." The quarks also come in three generations and a total of six "flavors," inferred from decades of numerous observations of composite particles such as the proton (discovered about 1920), the neutron (1932) [14], the pion and the kaon (1947) [15, 16, 17], the J/ψ (1974) [18, 19], and the upsilon (1977) [20]. After incorporating these data into the Standard Model, it predicted the sixth ("top") quark which was finally discovered at the Tevatron [21, 22].

The arrangements of the fermions and their interactions are now partially understood as consequences of a $SU(3) \times SU(2) \times U(1)$ local gauge symmetry. This specific idea (and, as should be remembered, concepts like "a quantum field theory" and "gauge symmetry") was developed in tandem with observations of the many ways fundamental fermions may behave. The electroweak sector consists of four bosons: the massless photon (γ), two charged vector bosons ($W^{\pm}$),

and a neutral vector boson (Z), all resulting from the spontaneous breaking of the $SU(2) \times U(1)$ weak-isospin+hypercharge symmetry via the Higgs mechanism. The strong "color" sector consists of eight gluons (g) corresponding to the generators of $SU(3)$. The Lagrangian dictating permitted interactions among the fermions and the bosons is a specific, renormalizable linear combination of the most general possible gauge-invariant set of terms that can be constructed from the fermion and boson fields.

This theory tries to explain everything in the known universe, so a complete description of all interactions predicted by it is certainly beyond the scope of this work[1]. I will emphasize some details which are relevant to the discussion in subsequent chapters.

2.1 Z bosons

The interactions mediated by the Z boson were not noticed until about a half-century ago, when observations of non-leptonic decay modes of strange mesons first hinted at the need to complement the earlier $V - A$ theory with a neutral intermediate boson [26]. By 1967, however, it was a key unobserved piece of the near-modern electroweak theory [27]. Thereafter, the Gargamelle ex-

[1] See instead [23, 24, 25, 1] and references therein.

periment (1973) saw persuasive evidence for it in neutrino-nucleon collisions, where lepton-less neutral current collisions accompanied the charged current $\nu_l + \text{nucleon} \rightarrow l^- + \text{hadrons}$ events predicted by the $V - A$ theory [28]. With its direct observation at the UA1 experiment in 1983 [29] as a few resonant events in the dielectron mass spectrum, detailed studies of the Z's properties began.

The Z is a charge-neutral particle and, with a mass of 91.1876(21) GeV/c^2 [1], the heaviest gauge boson, with the exception of the postulated Higgs. It couples to all SM fermions[1], decaying to various pairs of states as shown in Table 2.1 but not mixing lepton or quark generations. The decays to quark pairs of a given flavor each occur with a 10–15% branching ratio, with the exception of top quark pairs which are kinematically suppressed.

The Z is an important ingredient of the unconfirmed Higgs mechanism (discussed below), and so its continued study is of great interest. The Fermilab Tevatron produces single Z bosons through the process shown in Figure 2.1. The "Drell-Yan" decay to two leptons [30] is well-studied, with a scattering cross section of 251.3 ± 5.0 pb for $66 < M_{l\bar{l}} < 116$ GeV/c^2 for each lepton mode [31]. This is equivalent to an expectation of about $744,000 \pm 15,000$ total $p\bar{p} \rightarrow Z \rightarrow e^+e^-$ collisions for the dataset used in this thesis.

[1] i.e. massive neutrinos are an extension to the SM in this work.

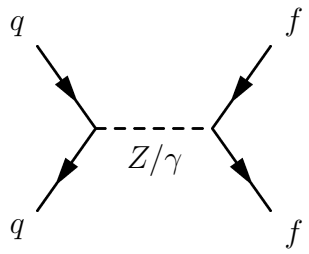

Figure 2.1: Tree-level Feynman diagram for Z boson production at the Tevatron.

2.2 ZZ production

At the Tevatron, production of two Z bosons (see Figure 2.2) is much less frequent than single Z processes. The inclusive Standard Model cross section for $M_{f\bar{f}}^{(1)}$, $M_{f\bar{f}}^{(2)} > 15$ GeV/c^2 is 1.4 ± 0.1 pb [32]. Most of the events produced decay to four or two jets and are hidden by higher-rate QCD and single-Z background processes. Only very recently have the two Tevatron collaborations become sensitive to the very rare four-lepton ZZ decays [33, 34]. In contrast, ZZ processes have been well-studied at the LEP experiments [35], which observed no significant deviation from the Standard Model expectation up to an e^+e^- center-of-mass energy of 207 GeV/c^2. The LEP data can place only indirect constraints on heavier, resonant ZZ production [36], and direct production constraints at high ZZ masses are limited to the publication of earlier, partial results of this work with approximately 40% of the dataset analyzed here [37].

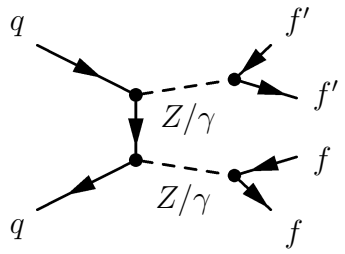

Figure 2.2: Tree-level t-channel Feynman diagram for ZZ boson production at the Tevatron.

2.3 Electrons and muons at high energy

The charged leptons couple electromagnetically and weakly but do not feel the strong nuclear force. As a consequence, the experimental backgrounds for four jet ZZ decays are much larger than decay channels containing a charged lepton. From a collider experimentalist's perspective, electrons and muons are therefore equally attractive, except for one important difference: the mass of the muon is about 106 MeV (measured to an accuracy of about 40 parts per billion) while the mass of the electron is 511 keV (measured to 25 parts per billion) [38], about 207 times lighter. This leads to properties and detector signatures for the two types of particles that are different.

Electrons lose energy by interacting electromagnetically with the atoms of the detector components. At the momenta typical of Z decay products, the energy loss is in the form of bremsstrahlung photons. Dense modern calorimeters exploit this to convert incoming high-energy electrons into showers of e^+e^- pair

production [39]. To a good approximation, the electron loses its energy as an exponential function of the distance it traverses in the calorimeter, characterized by the material "radiation length" X_0, and measurements of the shower depth and intensity provide an estimate of the initial energy. Eventually the energy of the shower constituents falls into an ionization-dominated regime and the shower dies out.

The typical Z decay momenta are not high enough for muons to enter a bremsstrahlung-dominated regime, so these lose energy mainly through ionization. At relativistic momenta, the Bethe-Block mean rate of energy loss with depth dE/dx is roughly independent of energy and close to its minimum; hence muons are sometimes referred to as "minimum-ionizing" [1]. The amount of calorimeter material required to stop minimum-ionizing muons is much greater than that required for electrons. In practice, muons pass completely through the CDF calorimeter and exit the detector, eventually decaying (unobserved) to lighter states via the charged weak current.

2.4 Jets and the strong interaction

The gluons carrying the strong force couple only to quarks (and other gluons). For present purposes, the most important property of this coupling is that it

is "asymptotically free"—the strength of the coupling is proportional to the inverse log of the energy scale of the interaction. The first evidence of this phenomenon was observed in electron-proton scattering experiments in the late 1960s [40], but the most dramatic examples are the "jets" [41] now ubiquitous at hadron collider experiments. $p\bar{p}$ collisions often produce bare partons which then quickly hadronize to form color-neutral states ("QCD confinement"). One observes sprays of copious hadrons, mostly pions, directed along the momentum vector of the original parton. This is by far the dominant result of a scatter between two hadrons at the Tevatron, about seven orders of magnitude more frequent than ZZ production. Because of the larger coupling at lower energies and consequent non-perturbative scattering amplitudes, the detailed calculations of hadronization require lattice QCD and are not fully understood. Nevertheless, jets are an important background to lower-rate lepton processes, and through data-driven background estimation techniques, one can use their prevalence to understand them.

While heavy, charged constituents of jets interact electronically with detector components in a manner similar to muons, the more important energy loss mechanism is through strong interactions with nuclei. The details of how hadronic showers develop and die out are more complex than electromagnetic showers, but a similar exponential energy loss approximation holds over a scale set by

the "nuclear interaction length" of the material [1]. Hadronic calorimeters are generally designed to contain almost all of the shower, subject to budget and time constraints. Combining this feature with further ionization detectors provides an additional way to separate muons from charged hadrons which happen to leave a lower than average energy deposition in the calorimeters.

2.5 New physics in the ZZ sector?

The $SU(2) \times U(1)$ electroweak gauge symmetry disallows boson and fermion mass terms in the Lagrangian [42, 43, 44]. A major focus of current research is the means by which the $SU(2) \times U(1)$ electroweak gauge symmetry is broken and the fields acquire mass. In the Standard Model, this is the Higgs mechanism [44, 45, 46, 47, 48, 27, 49].

As illustrated in [24], one introduces the eponymous spin-0 field (ϕ) and forces it to acquire a vacuum expectation value of the form

$$< \phi > = \frac{1}{\sqrt{2}} \begin{pmatrix} 0 \\ v \end{pmatrix}$$

In the Lagrangian, the kinetic term for ϕ

$$\begin{aligned}|D_\mu\phi|^2 &= |(\partial_\mu - igA^a_\mu\tau^a - i\frac{1}{2}g'B_\mu)\phi|^2 \\ &= ... + \frac{1}{2}\frac{v^2}{4}\big(g^2(A^1_\mu)^2 + g^2(A^2_\mu)^2 + (-gA^3_\mu + g'B_\mu)^2\big) \\ &= ... + \frac{1}{2}\frac{v^2}{4}\big(2g^2W^+_\mu W^-_\mu + (g^2+g'^2)Z^2_\mu + 0\cdot A^2_\mu\big)\end{aligned}$$

produces a series of mass terms for the new gauge fields of the "spontaneously-broken" electroweak symmetry:

- $W^\pm_\mu = (A^1_\mu \mp iA^2\mu)/\sqrt{2}$ (the charged weak current, with mass $M_W = gv/2$),
- $Z_\mu = (gA^3_\mu - g'B_\mu)/\sqrt{g^2+g'^2}$ (the neutral weak current, with mass $M_Z = v\sqrt{g^2+g'^2}/2$), and
- $A_\mu = (g'A^3_\mu + gB_\mu)/\sqrt{g^2+g'^2}$ (the massless photon.)

Fermions acquire masses through gauge-invariant $ff\phi$ interaction terms which assume vacuum expectation values

$$-\frac{\lambda_f}{\sqrt{2}}\, v\bar{f}_L f_R + \text{hermitian conjugate}$$

where λ_f is a new coupling constant to the Higgs set by the observed mass of the particle,

$$m_f = \frac{1}{\sqrt{2}}\lambda_f v$$

.

One can then split the fermion sector of the Lagrangian into chiral pieces and choose the gauge group representation for each piece that produces observed reality. The requisite representations[1] are three generations of left-handed weak-isospin SU(2) doublets

$$\begin{pmatrix}\nu_e\\ e\end{pmatrix}_L \qquad \begin{pmatrix}\nu_\mu\\ \mu\end{pmatrix}_L \qquad \begin{pmatrix}\nu_\tau\\ \tau\end{pmatrix}_L$$
$$\begin{pmatrix}u\\ d'\end{pmatrix}_L \qquad \begin{pmatrix}c\\ s'\end{pmatrix}_L \qquad \begin{pmatrix}t\\ b'\end{pmatrix}_L,$$

a CKM mixing matrix to convert from the gauge eigenstate (d'_L) to the mass eigenstate (d_L) basis, and three generations of right-handed singlets

$$e_R \qquad \mu_R \qquad \tau_R$$

$$u_R \qquad c_R \qquad t_R$$

$$d_R \qquad s_R \qquad b_R$$

.

However, the model now requires a gauge boson ϕ that has not been observed. A major goal of the Large Hadron Collider experiments is direct observation of this Standard Model Higgs at whatever the mass may be, but there may not be a Higgs at all, or there may be an entire Higgs sector, or the real mechanism for electroweak symmetry breaking is more clever than our best theorists. Without

[1] until the observation of neutrino oscillations

further evidence, such as the discovery of the particles responsible, we have no way of excluding any of these possibilities. Thus, the search for the Higgs or its equivalent has claimed the attention of most of the particle physics community. The LEP experiments, in searches for the process $e^+e^- \rightarrow ZH$, exclude the Standard Model Higgs for masses less than 114.4 GeV/c^2 [50] [1]. Global fits to various correlated and uncorrelated Standard Model parameters indirectly exclude the SM Higgs above 182 GeV/c^2 [51], and, most recently, the Tevatron collaborations have directly excluded the SM Higgs at 170 GeV/c^2 [52, 53][2].

A very heavy or bosophilic non-SM Higgs, or alternatively some unimagined mechanism, might show up in high mass ZZ decays at the Tevatron. But there are also many widely-recognized reasons to expect that the SM is missing important pieces, even beyond its obvious inability to explain dark matter [54, 55, 56] or dark energy [57, 58, 59]. For instance, recent persuasive evidence of neutrino mixing [60, 61, 62, 63] implies by analogy with the CKM mechanism that neutrinos have a small mass. In the Standard Model, neutrinos are massless, but this is simply one of its many ad hoc properties. If the analogy is meaningful, one must then augment the SM fields described above with an additional right-handed neutrino in order to introduce a quadratic mass term to the Lagrangian.

[1] though the ALEPH Collaboration saw hints of signal at 115 GeV/c^2.

[2] All three exclusions described claim 95% confidence.

Since the right-handed neutrino has never been observed, one has some freedom to concoct idiosyncratic revisions to the neutrino sector such as the "see-saw" mechanism, which includes both Dirac and Majorana mass of terms and hides the right-handed neutrinos at inaccessible energies [1]. The sustained activity around these and other questions makes contemporary neutrino research exciting, but also suggests that the weak interactions are not so well understood as we have thought. Thus, it is important to scour the electroweak sector for hints of new physics.

Another frequent argument against the Standard Model is that no convincing explanation exists for many of its properties. For example, the masses of each of the 6 quarks and 6 leptons, the three mixing angles and the CP-violating phase of the CKM matrix, the various couplings, and the Higgs mass are all free parameters. The gauge group and the field representations are arbitrary. Though anomaly cancellation requires an equal number of quark and lepton generations [24], there is no reason for the number of generations observed [1]. The masses of $W^{\pm}$, Z, and top quark, and apparently the Higgs mass and vacuum expectation value, all lie near the "electroweak scale" which seems to be special

[1]For certain assumptions, current experimental limits exclude b' quarks with masses below 268 GeV/c^2, t' quarks below 256 GeV/c^2, and fourth-generation charged leptons below 100.8 GeV/c^2 [64, 65, 66].

somehow, and well above the masses of ordinary quarks [67]. This is known as the "hierarchy problem." Absent new unexpected particles or interactions to drive their development, theories of physics beyond the SM often attract proponents in part because their potential to explain one or more of these properties.

I discuss one particular class of theories, "Randall-Sundrum" (RS) scenarios, in more detail in Chapter 3 because it happens to provide a convenient example of the massive ZZ production for which I search. But the model is also interesting on theoretical grounds, not only because it addresses the hierarchy problem, but also because it provides a framework for incorporating quantized gravity into our explanations of nature. Attempts to combine quantum field theory with the successful macroscopic theory of gravitation, general relativity, predict one or more spin-2 particles to mediate an attractive force with the observed properties of gravity [68]. These "gravitons" have not been observed, and gravity is not part of the Standard Model. The experimental difficulty is that gravity is very weak in comparison to the Standard Model forces, or, alternatively, the energy scale at which one expects quantum gravitational effects to become important, $M_p = \sqrt{\hbar c/G_N} = 1.2 \times 10^{19}\mathrm{GeV}/c^2$, is much higher than the electroweak scale [1]. The gigantic energy necessary makes probes of gravity impossible at present particle colliders. Or perhaps not.

[1] This is often described as another aspect of the hierarchy problem.

Decay Mode	Branching Ratio
e^+e^-	0.03362(42)
$\mu^+\mu^-$	0.03662(66)
$\tau^+\tau^-$	0.0370(8)
$\nu\bar{\nu}$	0.2000(6)
$q\bar{q}$	0.6991(6)

Table 2.1: Z decay branching ratios [1].

Chapter 3

Randall-Sundrum scenarios

In [69, 70], Randall and Sundrum propose a now-popular scenario in which we live on one of two 3-branes in 4+1-dimensional non-factorizable spacetime separated in the extra spatial dimension by a distance πr_c. In the original scenario, Standard Model particles remain confined to either our "TeV" brane or the opposite "Planck" brane, but gravitational modes can propagate through the extra dimension, which is very small and highly warped by a factor e^{-kr_c}. An intriguing consequence is that on our brane we will measure a mass of

$$m = e^{-k\pi r_c} m_0 \tag{3.1}$$

for a mass parameter m_0 in the 4+1-dimensional Lagrangian. Here k, described below, is on the scale of the higher-dimensional Planck mass M_5 and r_c is the

compactification "radius" between the two branes. The Planck mass in 3+1 dimensions, $M_{Pl} \sim 10^{19}$ GeV, and the Planck mass in 4+1 dimensions obey the relation

$$M_{Pl}^2 = \frac{M_5^3}{k} \cdot (1 - e^{-2\pi k r_c}) \tag{3.2}$$

If $kr_c \approx 12$, the model offers an appealing reformulation of the hierarchy problem: the electroweak-scale fundamental masses we have observed in four dimensions are effective versions of much larger fundamental masses in the higher-dimension space, all of which have values at the M_5 scale. While these special "stable" values of k and the radius of the extra dimension must now be explained, one can argue that progress has been made, if the idea turns out to be correct.

One can make difficult table-top tests of the gravitational inverse square law in order to search for the dilution of gravity by extra dimensions. However, whereas the results of these experiments [71, 72, 73, 1] can constrain ADD-type scenarios where the extra dimension is large, the RS model depends only on the exponential of r_c, and the extra dimension can be very small and still create the necessary hierarchy.

Nevertheless, the RS scenario's viability as a solution of the hierarchy problem is intimately linked to collider phenomenology, and it makes a prediction that can be tested. The non-trivial gravitational modes are boxed in by the two branes, quantizing their momentum in the extra dimension. This shows up on

the TeV brane in a "Kaluza-Klein" tower of discrete, massive spin-2 excitations, unevenly spaced along the Bessel zeroes of $J_1(x)$ according to

$$m_n = e^{-k\pi r_c} \cdot kx_n = \frac{k}{M_{Pl}} \cdot \Lambda_\pi \cdot x_n \tag{3.3}$$

where the first two values of x_n are 3.83 and 7.02 and the graviton mass scale on our brane $\Lambda_\pi = e^{-k\pi r_c} M_{Pl}$, using the notation in [36]. k, related to the brane and bulk cosmological constants, sets the higher-dimensional graviton mass scale. In solving Einstein's equations, the results in [69, 70, 36] assume k is "small" compared with M_5 to keep the bulk curvature under control. While [36, 74] use comparisons with string theory or a model of gauge unification in the Randall-Sundrum scenario to argue for $0.01 \leq k/M_{Pl} \leq 0.1$, in general the parameters have no theoretical constraints.

The uniform coupling of graviton modes to the Standard Model sector [36,70] is the inverse of the graviton mass scale,

$$\frac{1}{\Lambda_\pi} = \frac{x_n}{m_n} \frac{k}{M_{Pl}} \tag{3.4}$$

In the same case $kr_c \approx 12$ where the RS model explains the weak-Planck hierarchy, Λ_π is at the TeV scale. Thus, whatever the values of k or r_c, the first massive graviton resonance $m_G = m_1$ must appear strongly coupled to the Standard Model at energies accessible to the Tevatron and/or LHC in order for

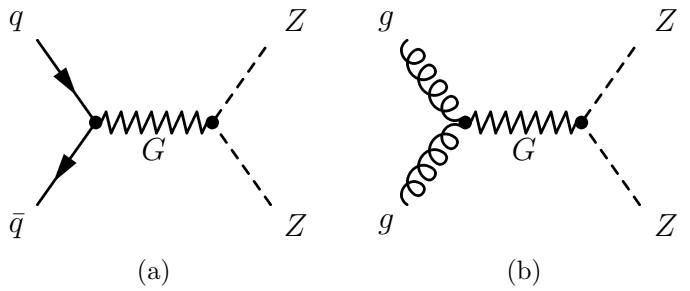

Figure 3.1: Feynman diagrams for ZZ production

the attractive hierarchy to appear. This offers the possibility that CDF may see evidence of graviton production at the Tevatron during Run II [1].

3.1 RS gravitons at the Tevatron

$p\bar{p} \to G \to ZZ$ production at the Tevatron would proceed through both $q\bar{q}$ and gg components. Figure 3.2 shows the expected production cross sections for various combinations of k/M_{Pl} and m_G, and Figure 3.3 shows the quasi-model-independent expected branching ratios for any spin-2 graviton into various channels as a function of graviton mass (and assuming no other undiscovered particles.) CDF has an excellent chance to observe gravitons with m_G less than about 1 TeV if the coupling k/M_{Pl} is at least as large as the suggested $0.01 \leq k/M_{Pl} \leq 0.1$ range, and searches in the diphoton and dilepton modes [76, 77, 78]

[1] Note that, because the coupling is proportional to k and inversely proportional to the graviton mass on our brane, a small region of the parameter space is available to CDF.

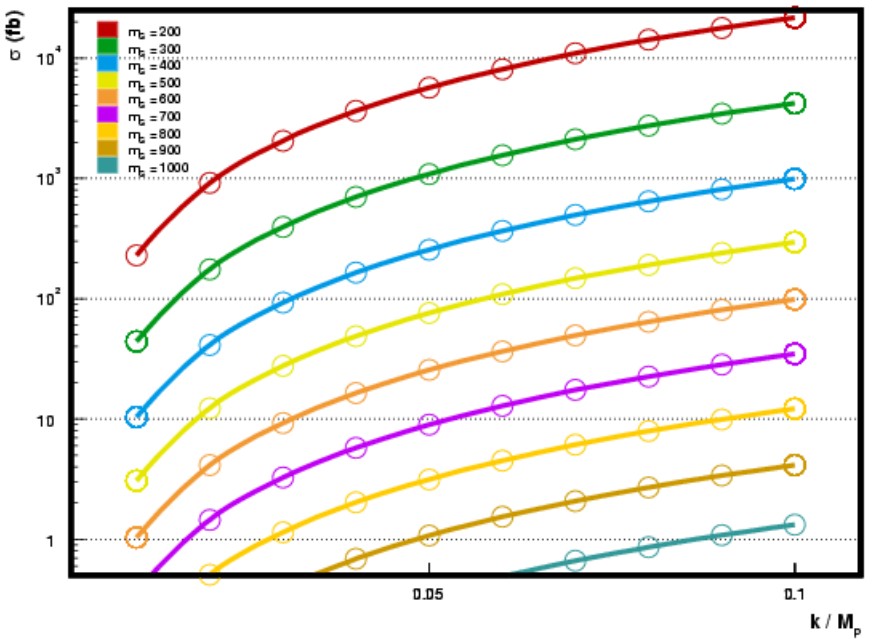

Figure 3.2: $G \rightarrow ZZ$ cross sections computed using HERWIG 6.5 (masses in GeV).

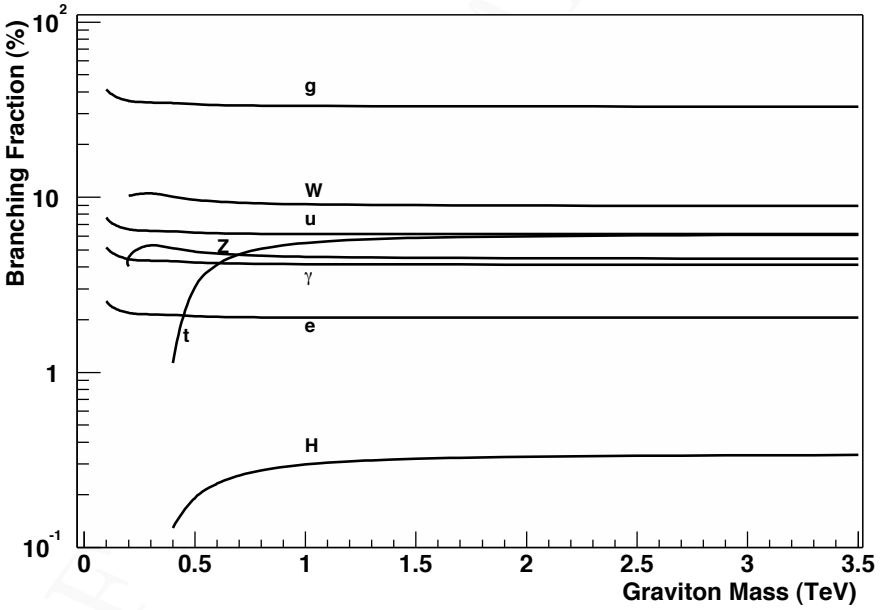

Figure 3.3: Graviton branching fractions [75]. For the unexplored mass range accessible at the Tevatron (0.2 to 1.0 TeV), virtual gravitons mostly decay into two jets. The remaining modes are W^+W^- (10%), ZZ (5%), $\gamma\gamma$ (5%), and ll (2% per lepton).

have already ruled out the first $k/M_{Pl} = 0.1$ graviton in the tower for masses $M_G < 921$ GeV/c^2.

While the $G \to ZZ$ branching fraction is nearly the same as the fraction to diphotons and to stable dileptons, the diboson modes considered in this work must pay an additional $O(10^{-1})$ penalty for each $Z \to ll$ decay, making competition with the existing searches difficult for scenarios where the uniform (or "democratic") coupling holds. However, ZZ and other decay modes can become crucial in modified "bulk" RS scenarios, where arbitrary Standard Model fields can propagate in the extra dimension(s). This introduces the freedom to localize some SM states on the TeV and others on the Planck brane, enhancing or suppressing their effective coupling to the graviton [79, 1].

Regardless, the RS scenario is useful as it provides a widely-studied example of a massive, narrow resonance decaying to ZZ pairs. The $p\bar{p} \to G \to ZZ$ process is included in several widely-available Monte Carlo generators, notably HERWIG and PYTHIA, and is therefore well-suited as a benchmark for communicating search results to the scientific community. Though the search described in the following pages aims at model-independence, it will use RS gravitons in this way.

Chapter 4

The CDF experiment

This search for a massive resonance via $X \rightarrow ZZ$ takes place at the upgraded Collider Detector at Fermilab, a general purpose experiment to study the results of $\sqrt{s} = 1.96$ TeV $p\bar{p}$ collisions at the Fermilab Tevatron [80]. In this chapter I briefly summarize the accelerator chain which produces the collisions, the detector which observes their byproducts, and some aspects of the software which reconstructs their topologies, with detail on my contributions.

4.1 The accelerator

The Fermilab accelerator chain starts with a bottle of hydrogen gas. This hydrogen is then accelerated in series by a 750 keV Cockcroft-Walton accelerator

[81, 82, 83] and a 400 MeV Linac. At injection to the "booster" synchrotron, the hydrogen is stripped of its electrons and accelerated to 8 GeV. The next stage, the Main Injector, accelerates protons to 150 GeV for "shots" into the Tevatron. For unknown reasons, anti-matter is not easy to find, and so anti-protons are created by 120 GeV proton shots from the Main Injector into a nickel target and placed into two storage rings, called the "accumulator" and the "recycler," until the Tevatron has been loaded with protons. The Tevatron then performs the final acceleration of both to 979 GeV. The main factors limiting the number of collisions provided for experimental analysis are the rate at which anti-protons can be produced and the efficiency for collecting and moving them through the accelerator chain into the Tevatron.

In the Tevatron, a 1-km-radius synchrotron, protons and anti-protons are each arranged into 3 trains of 12 "bunches." From an aerial view, protons circulate clockwise and anti-protons circulate counterclockwise. With this arrangement, p's and $\bar{p}$'s from the two trains are made to collide every "bunch crossing" (396 ns) at two interaction points. The CDF detector surrounds one of these points.

4.2 Overview of the CDF Detector

Figure 4.1 shows a cross section of half of the CDF detector. The other half is a mirror image along the right vertical edge of the figure, and the detector has rough cylindrical symmetry about the beam pipe, shown running horizontally across the center of the figure. The cylindrical CDF coordinate system is centered on the center of the detector with the z axis running along the beam pipe. Protons approach the interaction point moving in the $+z$ direction and anti-protons in the $-z$ direction. The detector consists of millions of parts, arranged into dozens of subsystems described in [80, 84] and elsewhere. I will avoid describing each one and concentrate on my contributions.

A combination of tracking systems reconstructs the trajectories and measures the transverse momenta of charged particles using an eight-layer silicon microstrip vertex detector [85, 86, 87] and a 96-layer open-cell drift chamber [88]. The tracking chambers are surrounded by a superconducting solenoid generating a 1.4 T magnetic field. The first silicon detector element, L00, lies mounted directly on the beam pipe at radii between 1.3 and 1.6 cm. Two additional silicon subsystems, SVX and ISL, make measurements at radii from 2.5-29 cm and $|\eta| < 1.8$[1]. All three silicon subsystems are arranged in barrel geometries and segmented into ϕ wedges. The drift chamber, the COT, makes trajectory mea-

[1] $\eta = -ln\ tan\ \frac{\theta}{2}$

surements at large radii $43 < r < 132$ cm and $|z| < 155$ cm, with full coverage for $|\eta| < 1.5$ and partial coverage for $|\eta| < 2.0$. The latter is fully exploited for the first time in this work. Section 4.5 describes this in more depth.

Outside the solenoid, segmented electromagnetic (EM) lead-scintillator and hadronic (HAD) iron-scintillator sampling calorimeters measure particle energies [89, 90, 80, 91, 92]. The central $|\eta| < 1.1$ calorimeters (CEM,CHA,WHA) are arranged in a projective cylindrical geometry about the interaction point, with 15° wedges which measure EM energies with a resolution $\sigma^2_{\rm CEM} = 0.135^2 E + 0.015^2 E^2$. The forward (or "plug") calorimeters are arranged in an azimuthally-symmetric disk geometry and measure EM energies with a resolution $\sigma^2_{\rm PEM} = 0.16^2 E + 0.01^2 E^2$. Wire chambers and precision scintillating strips embedded in the calorimeters at $6\ X_0$, the depth of typical shower maximum, provide more precise position measurements of shower development throughout the central EM calorimeter and in the forward EM calorimeters for $1.13 < |\eta| < 3.5$ [93].

Beyond the calorimeters lie various muon drift cells and scintillators to note particles which traverse the entire inner and outer detectors [94, 80]. In the present study, only the muon chambers with inputs to the trigger are relevant. The CMU lies just outside the central hadronic calorimeter with ϕ-dependent coverage of $0.03 < |\eta| < 0.63$ and the CMX covers $0.65 < |\eta| < 1.0$. The CMP

augments the CMU coverage in ϕ and lies behind another ≈ 3 interaction lengths of steel.

Most of the data acquired by these detectors is discarded. At each bunch crossing, a three-level trigger system analyzes the detector output and decides whether or not the "event" is interesting enough to record. Successful events are stored to tape, then processed by 7.2 million lines of event reconstruction source code and analyzed by the collaboration. The total number of collisions delivered is determined relative to the inelastic $p\bar{p}$ cross section using Gas Cerenkov detectors to check for collision byproducts at $3.7 < |\eta| < 4.7$ [95].

4.3 Contributions to detector operations

My involvement in day-to-day data collection has been primarily with the operation and maintenance of the silicon detectors. Inside the collision hall, I helped maintain the detector and supporting infrastructure. For example, along with Adam Scott and Ben Brau, I repaired 1/7 of the central ISL coverage after it had been given up for dead. Outside of the collision hall, I led a group of students and postdocs in monitoring raw data quality and diagnosing readout problems, and I supervised two computer science students while upgrading control room real time raw data monitoring software.

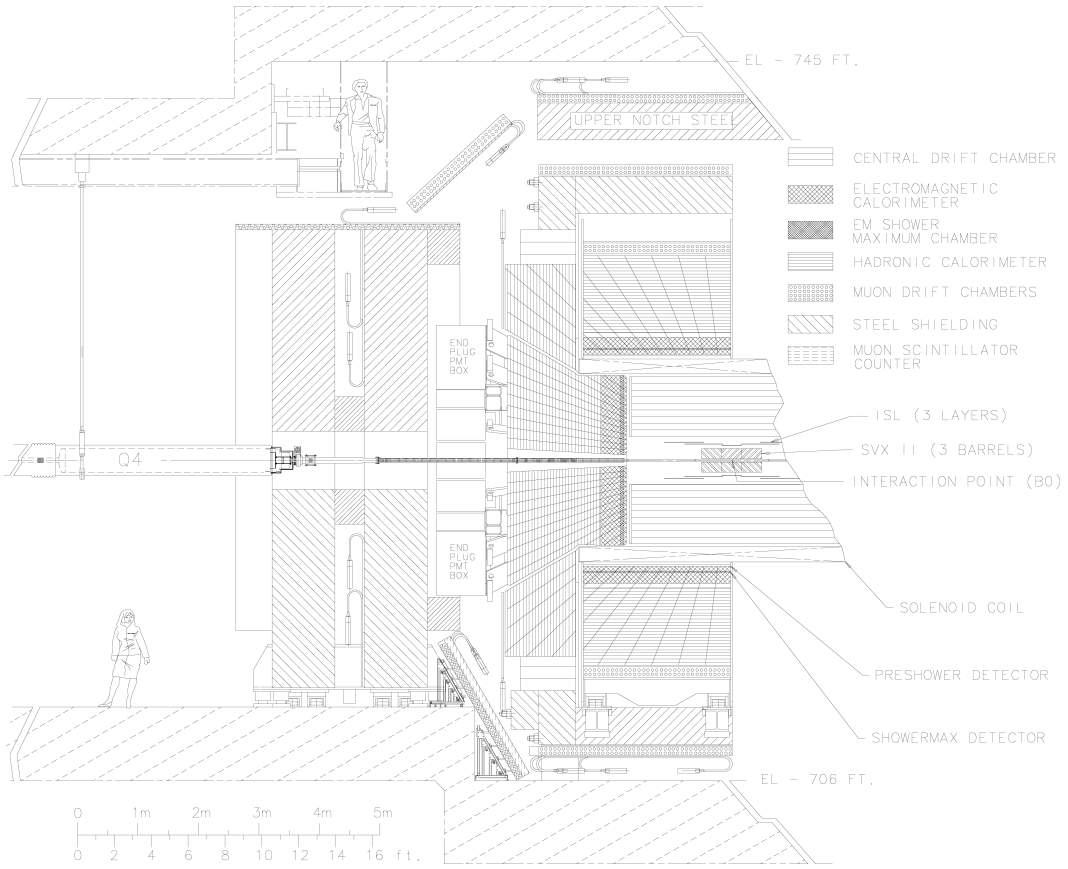

Figure 4.1: Elevated view of half of the CDF detector [80].

With Ben Brau and David Stuart, I developed procedures to monitor the depletion voltages of the various silicon sensors as they evolve under irradiation, in order to assess the operable lifetime of the detectors [96, 97, 98]. Figure 4.2 illustrates the separate methods used for single-sided L00 silicon and the double-sided SVX and ISL silicon. Our "signal" method studies the charge distribution of clusters attached to high quality tracks as a function of the bias voltage applied to the L00 sensors, while our "noise" method monitors the interstrip shot noise opposite the junction side as the depletion zone grows. Figure 4.3 summarizes our initial results after analyzing regular scans of all functioning detector components taken between 0.2 and 1.3 fb^{-1} of delivered luminosity. An extrapolation well past the 1.3 fb^{-1} data to 5-8 fb^{-1} suggests that known limitations on our ability to bias the inner silicon layers are not likely to affect their operation through the end of the experiment. To date, the Tevatron has delivered approximately 5.4 fb^{-1}, and the silicon operations group continues to use our methods to monitor the depletion voltages, with similar results.

4.4 Track reconstruction and contributions

I made large changes to the CDF track reconstruction software in order to greatly improve its performance in the forward $1 < |\eta| < 2$ region and maintain

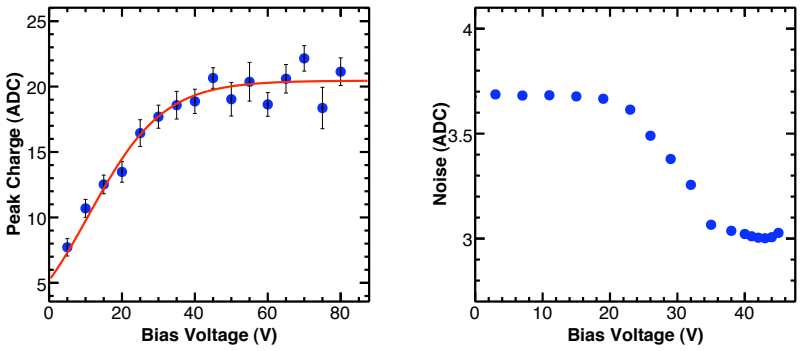

(a) (b)

Figure 4.2: Example scans for (a) a single L00 DAQ unit and (b) a single SVX L0 DAQ unit.

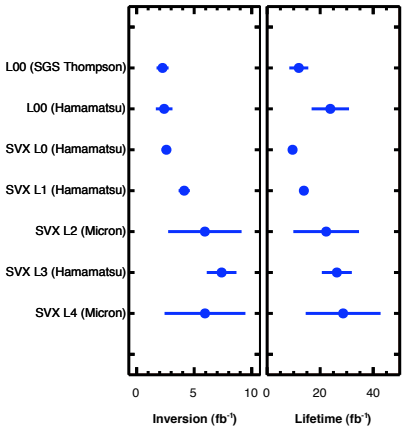

Figure 4.3: Depletion voltage analysis results with 1.3 fb^{-1} [96], showing the mean and RMS of individual DAQ unit predictions for type inversion and, under a same-rate assumption, maximum operable lifetime.

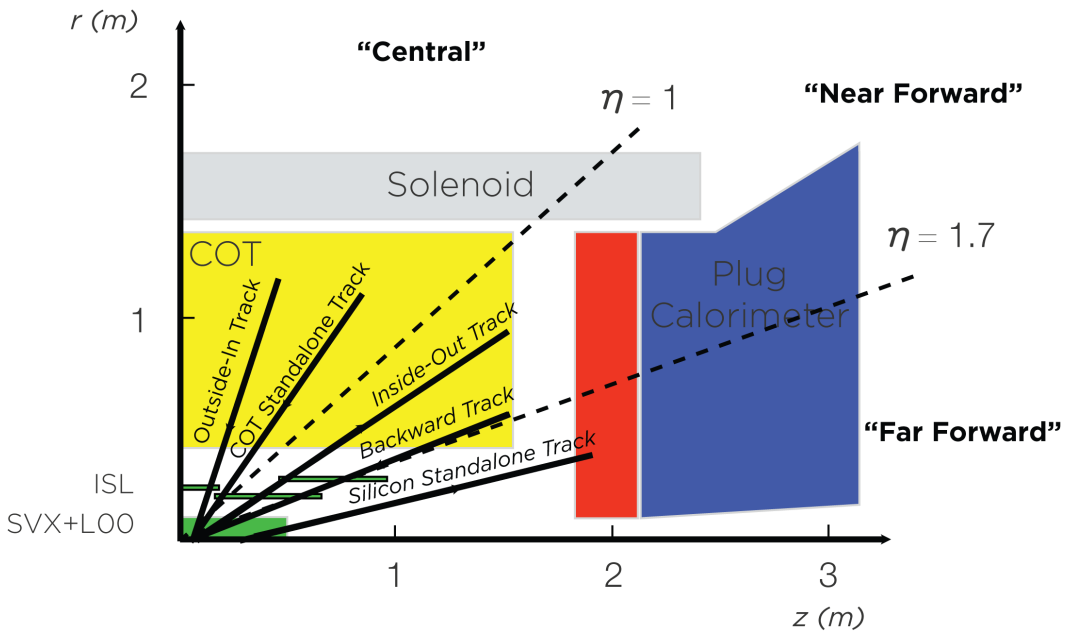

Figure 4.4: Schematic of the tracking system.

its overall efficiency in later and higher-luminosity data. The subsequent software release, labeled within the collaboration as "Gen-7," also incorporates several subsequent spin-off projects, in all of which I played a critical role, and includes changes to most of the approximately 900,000 lines of tracking source code. This thesis uses that new software for the first time.

Figure 4.4 shows an $r-z$ schematic of the tracking volume. Charged particles originating at $r = z = 0$ with momentum such that $|\eta| < 1.01$ traverse 7 of 8 silicon layers and the entire 96-layer COT, passing through 8 groupings of 12 sense wires called "superlayers."

In the silicon, the applied bias voltage sweeps charges freed along the trajectory toward readout strips on one or both sides of the active volume. Identical strips running parallel to the z axis on the junction side allow a ϕ position measurement of this ionization with a resolution of 10–200 μm. On 3 of the 5 layers of SVX, strips running perpendicular to the z axis opposite the junction side make z position measurements with 20–200 μm resolution. The ISL and remaining SVX layers have "small angle stereo" strips tilted 1.2° with respect to the z axis and, when combined with the ϕ-side information, allow "3D" $\phi - z$ measurements. In all cases, the charge on each strip is recorded and is an important part of the position measurement.

In the COT, the charges freed along the trajectory are swept to the nearest of its 30,240 total sense wires which run nearly parallel to the z axis. The wires in four of the eight superlayers are tilted at a 2° angle to allow stereo position measurements once the ϕ trajectory is known. The charges drift from the ionization site toward the sense wires at a velocity of about 50 μm/ns, arriving in a cascade that is then transmitted down the length of the sense wire (up to 310 cm.) At the end of the sense wire, readout electronics (TDCs) measure the resultant pulse arrival time and width. Depending on the distance from the ionization site to the sense wire and other geometric factors, this then provides a ϕ position measurement with a resolution of 140–200μm.

For each event, the collection of up to 750k recorded silicon strip and COT sense wire data must be analyzed to reconstruct position measurements ("hits") and the charged particle trajectories ("tracks") and their momenta. While I'm familiar with nearly every detail of the analysis, a full discussion could easily double the length of this thesis. I will therefore concentrate on a single feature of the new software and only briefly highlight my other contributions.

4.5 "Backward" tracking

CDF uses two main approaches to reconstruct tracks. Central tracking ($|\eta| < 1$) starts in the COT and assembles piecewise "segments" in each superlayer, fits them, and matches them in pairs together to form "CT" tracks. The "Outside-In" silicon algorithm then attempts to attach at least three silicon hits in ISL and SVX, moving inward. Tracks which fail to acquire silicon hits are called "COT standalone" tracks. The results are clustered into a collection of primary interaction vertices distinct in z. Afterward, "silicon standalone" tracking ($|\eta| > 1$) tries to form tracks starting with all possible combinations of three unattached silicon hits (two 3D hits and one additional ϕ hit) and all z vertices. Successful silicon standalone tracks are then projected into the COT. If any higher-radius

measurements are found there, the track is converted to a "Inside-Out" track with improved momentum resolution.

Prior to my involvement, these approaches resulted in low combined efficiency in the $1 < |\eta| < 2$ region. Though very efficient when full COT coverage is available, above $|\eta| = 1$ the high-quality central tracking algorithms lose efficiency nearly linearly with $|\eta|$ until zeroing out around $|\eta| = 1.6$. The silicon fully covers $|\eta| < 1.8$ to compensate for the falling COT efficiency, but the existing silicon-driven algorithms, developed by several university groups over half a decade, were never more than 40% efficient and produced low-quality or spurious tracks with poor momentum resolution.

There was a sole successful forward tracking algorithm. The "Phoenix" tracking algorithm uses the forward calorimeter energy measurement, the more precise shower maximum position measurement, and the 3D position of the highest sum p_T z vertex to construct two track hypotheses (one for each charge.) Those hypotheses are then fed into the Outside-In silicon search as if they were CT tracks. The additional constraints drastically simplify the search problem, producing an algorithm which reconstructs 80% of electron tracks at $|\eta| = 1$, falling to 50% at $|\eta| = 2$. But because it depends on shower measurements in the calorimeter, it applies only to $E_T > 5$ GeV electrons.

Superlayer	Radius (cm)	Measurement Type	Maximum $\|\eta\|$ Coverage
7	131	ϕ	1.01
6	119	stereo	1.08
5	106	ϕ	1.17
4	94	stereo	1.27
3	82	ϕ	1.39
2	70	stereo	1.54
1	58	ϕ	1.71
0	46	stereo	1.93

Table 4.1: COT $|\eta|$ coverage by superlayer.

There is another way to constrain the silicon search. Table 4.1 shows the angular coverage of the COT at each superlayer. Tracks originating from $z = 0$ with $|\eta| < 1.7$ will leave traces of their passage in the lowest-radii superlayers of the COT.

I developed a new algorithm, "backward" tracking, from this idea. Figure 4.5 illustrates the idea with a very simple case where either superlayer 1 or superlayer 3 provide the necessary traces. Backward tracking starts by searching the COT for hits unused by the central CT algorithm and constructing segments in each superlayer of no more than 12 hits. At this stage, the position measurements

contain a drift sign ambiguity (red and blue in the figure) and important drift time corrections are completely unknown (e.g. z-dependent corrections such as the time of flight and the propagation time down the sense wire to the readout.) The CT segment-finding algorithm therefore makes assumptions which are appropriate for central tracks but which, for measurements at large z, can lead to position mistakes as large as 1 mm [1]. To compensate, backward tracking uses a heavily-modified version of the original segment pattern recognition, custom-designed for tracking at low radius (high hit density) and near the COT endplates [2].

Once all segments are found, the algorithm then fits the hits on each segment to obtain a five-parameter helix which intersects the highest sum p_T z vertex. In order to produce a useful track parameter estimate from a small number of COT hits, the fit must carefully account for effects which can be neglected by the central tracking as well as accurately estimate fit parameter uncertainties and correlations. The primary technique employed to handle z-dependent timing corrections is the "split-drift fit." The drift sign ambiguity is resolved by computing both possible positions and minimizing the χ^2 of a linear fit. The hits are then split into two sets by their drift sign, spurious or mismeasured hits

[1] Recall the typical hit resolution is a couple hundred microns.

[2] This has been subsequently merged into a later rewrite of the original by Aseet Mukherjee.

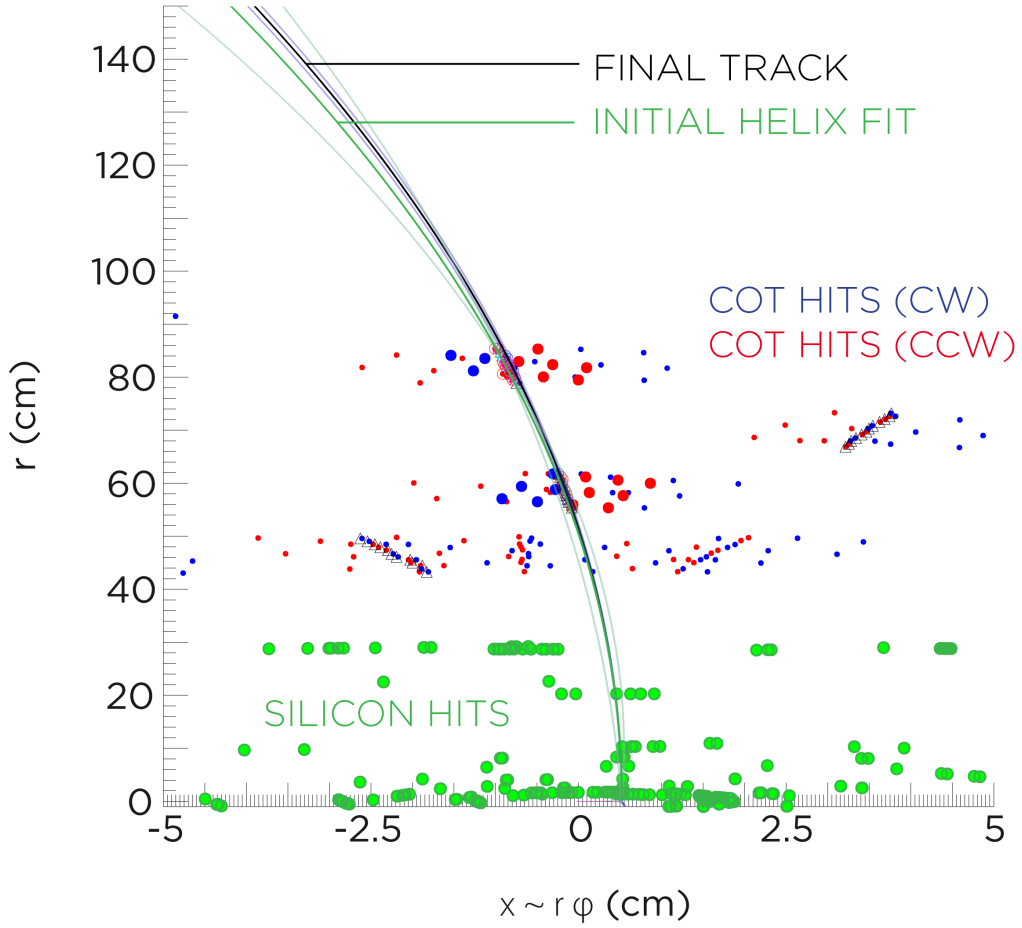

Figure 4.5: Rotated and skewed $r - \phi$ view of the tracking volume, illustrating backward tracking for a very simple situation in $Z \rightarrow \mu\mu$ simulation.

are pruned, and the remaining sets are fit to two separate lines. If each hit's drift time shares a common offset, the two line fits will not coincide and their separation is used to iteratively correct the offset. After completing the corrections and the final linear fit to the entire segment, the fit uncertainty is determined from a combination of the expected hit resolutions and the distributions of the residual "N-1" fit parameters.

After obtaining initial segment fits, the algorithm begins the silicon hit search. The segments are considered sequentially, beginning with the highest-p_T hypothesis on the highest-radius superlayer. Initially, each track's longitudinal angle (θ) is unknown. The silicon detectors are segmented in z into barrels, so the search proceeds in the outer layer of each barrel simultaneously using a list of hypotheses. For each barrel, the COT segment is refit with drift time corrections appropriate for an approximate θ hypothesis and the fit is extrapolated to all wedges compatible with the fitted trajectory. Any silicon hits consistent with a 4σ road around the extrapolated positions generate new, refitted hypotheses which are added to the initial list. Hits having ionization inconsistent with the fitted trajectory as well as hits used by central tracks or by higher-p_T backward tracks are ignored. The search then moves to incrementally lower radii. At each stage, an internal material model is used to correct each hypothesis's energy and parameter uncertainties for multiple scattering, and hypotheses with few

attached hits are discarded while candidates with more attached hits are kept. Once a single hit is attached, the fit is allowed to follow subsequent hits away from the initial vertex-constrained hypothesis. After searching all layers, quality criteria based on hit pattern are applied to the remaining hypotheses, and then all hypotheses except that with the most hits are discarded. Finally, the COT is searched for any remaining information, the track's COT and silicon hits are marked as used, and the procedure is repeated for the remaining segments.

The new algorithm has been validated on a variety of samples, with emphasis on large samples of $Z \to ee$ and $Z \to \mu\mu$ simulation and data. Figure 4.6 shows the efficiency to reconstruct muon tracks in a sample of simulated $Z \to \mu\mu$ decays for either the Outside-In or the backward algorithm, or alternatively the Outside-In algorithm alone. Figure 4.7 shows the improvement in muon-triggered data $Z \to \mu\mu$ yield involving higher-quality forward tracks with COT hits for a small subset of the data used for this thesis. The red curve represents the dimuon mass spectrum for the combination of a central trigger muon tracked with the Outside-In algorithm and a forward COT muon tracked with the Inside-Out algorithm in the old software. The black curve shows the same spectrum in the new software, where backward tracking has largely superseded the Inside-Out algorithm. With a modest increase in combinatoric background, the peak yield has improved by about 260%.

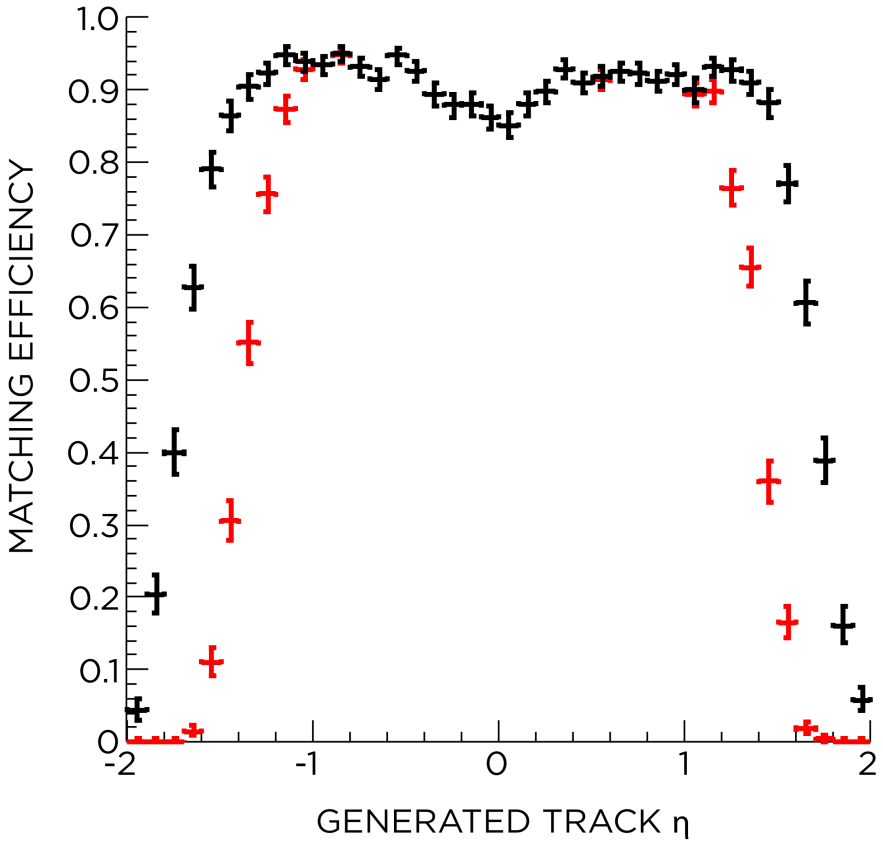

Figure 4.6: Efficiency to reconstruct generated charged particles with $p_T >$ 10 GeV in $Z \to \mu\mu$ simulation vs track η with (red) the Outside-In reconstruction algorithm and (black) the backward and Outside-In reconstruction algorithms. Prerelease version of the new software.

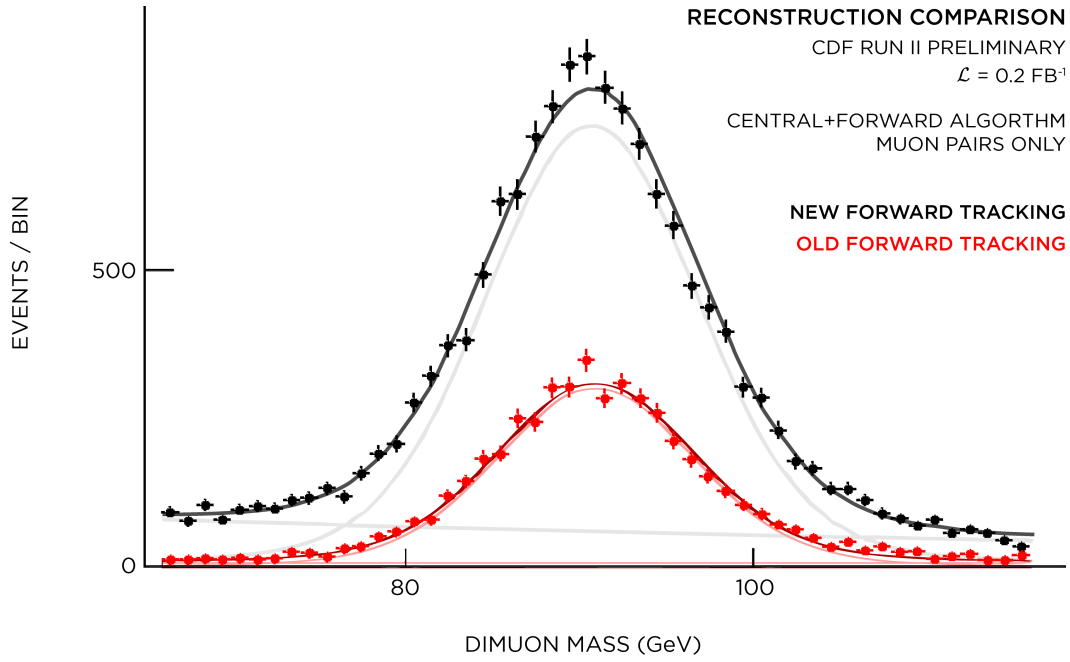

Figure 4.7: Dimuon mass spectrum for Outside-In central trigger + backward or Inside-Out forward muons using the old and new reconstruction software on approximately 175 pb^{-1} of muon-triggered data. Selective event reprocessing (discussed in Chapter 5) was not used. Prerelease version of the new software.

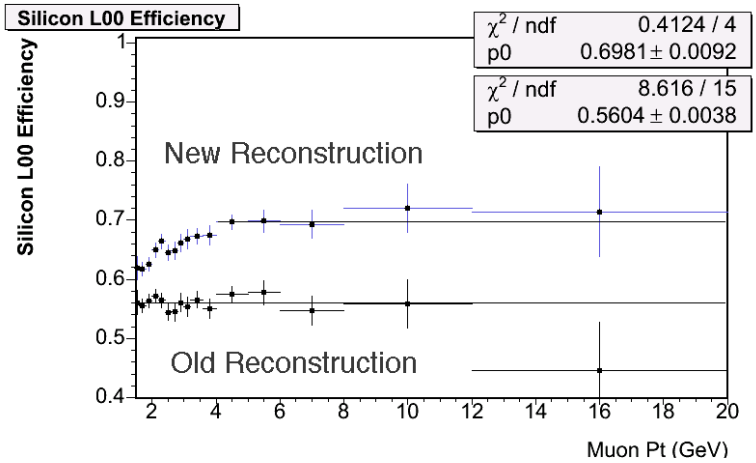

Figure 4.8: Efficiency for attaching L00 silicon hits to tracks in $J/\psi \to \mu\mu$ data (plot provided by Matt Herndon).

4.6 Other tracking contributions

My work on the backward algorithm stimulated other interest in solving long-standing tracking problems and preparing the software for the future. My contributions to the resultant software release include:

- Reoptimization of L00 usage with Ben Brau, Matt Herndon, and Rick Snider. Figures 4.8 and 4.9 compare the efficiency to attach a L00 cluster to an Outside-In track between reconstruction versions. These and further studies indicate the new software attaches L00 hits to an additional 15% of isolated tracks without degrading their impact parameter or other measurements. Below the 15-30 GeV region containing electrons in the

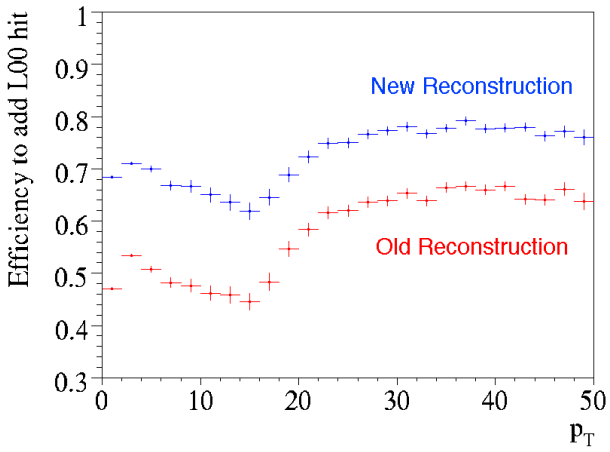

Figure 4.9: Efficiency for attaching L00 silicon hits to tracks in $Z \rightarrow ee$ data (plot provided by Ben Brau).

radiative tail of the $Z \rightarrow ee$ data, the increased rate of L00 attachment to $p_T < 15$ GeV tracks in the recoil jet suggests a potentially larger increase in dense environments.

- A bottom-up rewrite of the COT tracking code by Aseet Mukherjee, author of the original Run I CTC software. Along with his many other changes, we worked together to increase standard segment finding efficiency in the inner superlayers at high instantaneous luminosity or track density.

- Measurement of silicon cluster resolutions for the first time with the new Run II detector with Ben Brau.

- With Matt Herndon, a factor of 10 CPU time reduction for silicon standalone tracking, making a higher-efficiency algorithm possible.

- Too many other improvements to mention.

It is satisfying to note that my ideas regarding silicon standalone optimization have been propagated back into older versions of the software, halving the CPU requirements for the entire reconstruction of high luminosity events.

The following analysis makes use of all of the new software for the first time.

Chapter 5

Search for $X \to ZZ$

With motivation and background in hand, I now turn to the specific search for $X \to ZZ$ at high M_X where the contributions from known processes are almost nonexistent. Again, this is a signature-based search; my motivation is the low background and potential for sensitivity rather than any compelling theory.

5.1 Outline of method

I begin the search with data from high E_T electron and high p_T muon triggers and, working independently from the rest of the collaboration, reprocess these data with the new offline software (referred to here as "7.1.0"). After baseline quality cuts, I select electrons and muons with very efficient lepton identification

criteria and jets with criteria standard to CDF. I check my understanding of this selection and of 7.1.0-based simulation by comparing dilepton spectra built from various combinations of leptons. I then reconstruct signal X candidates consisting of triggerable four-body combinations of electrons, muons, and jets. While developing the method, I blind myself to four lepton combinations[1] with total mass exceeding 300 GeV and Z + jets combinations with $M_X > 300$ GeV where the dijet mass is consistent with a Z (65–120 GeV.) I estimate the low-rate diboson backgrounds with simulation and all other fake lepton and non-resonant backgrounds with sideband data samples. I then perform a counting experiment in the blinded mass region, computing expected limits assuming zero signal, before finally unblinding the hidden data. Upon unblinding, I observe no excess of events consistent with a narrow ZZ resonance and set 95% confidence level limits on the $X \to ZZ$ cross section using acceptance from a HERWIG Monte Carlo RS graviton process.

[1]The first 1.1 fb^{-1} of four electron data were unblinded by the previous iteration of this analysis but are treated as blind here.

5.2 Data samples

5.2.1 Triggers

A pair of high E_T electron triggers and a pair of high p_T muon triggers feed the CDF standard BHEL and BHMU datasets, respectively. I analyze data collected during Runs 141544–261005, Periods[1] 0–17 (March 2002–April 2008), which constitutes a little less than 3 fb^{-1} of integrated luminosity. I require all data fire one of four trigger "paths." Each trigger path consists of a different set of requirements at each of the three trigger levels. The variables are described elsewhere and in Section 5.4 in some detail. The paths are:

- ELECTRON_CENTRAL_18
  - L1 - A central electron cluster with $E_T > 8$GeV, $E_{HAD}/E_{EM} < 0.125$, and an associated $p_T > 8.34$ GeV XFT[2] track.
  - L2 - A central electron cluster with $E_T > 16$ GeV, $E_{HAD}/E_{EM} < 0.125$, and an associated $p_T > 8$ GeV XFT track.
  - L3 - A central electron cluster with $E_T > 18$ GeV, $E_{HAD}/E_{EM} < 0.125$, $L_{SHR} < 0.4$, and an associated $p_T > 9$ GeV L3 track that

[1] These run "periods" constitute arbitrary chunks of O(100 pb^{-1}) integrated luminosity.

[2] A COT tracking hardware for the trigger.

extrapolates to the CES within 8 cm in z of the cluster position. The E_T calculation uses the track angle.

- ELECTRON70_L2_JET
  - L1 - A central or forward jet cluster with $E_T > 10\,\text{GeV}$.
  - L2 - A jet cluster with $E_T > 90\,\text{GeV}$ and $|\eta| < 3.6$.
  - L3 - A central electron cluster with $E_T > 70\,\text{GeV}$, $E_{HAD}/E_{EM} < 0.2$, $L_{SHR} < 0.4$, and an associated $p_T > 15\,\text{GeV}$ L3 track.
- MUON_CMUP18 or an equivalent with events that satisfy
  - L1 - An XFT track with $p_T > 4$ GeV associated with both a CMU and a CMP stub.
  - L2 - An XFT track with $p_T > 14.77$ GeV associated with both a CMU and a CMP stub.
  - L3 - A minimum ionizing track with $p_T > 18\,\text{GeV}$ associated CMU and CMP stubs, $|\Delta X_{\text{CMU}}| < 20\,\text{cm}$, and $|\Delta X_{\text{CMP}}| < 10\,\text{cm}$.
- MUON_CMX18 variant with events that satisfy
  - L1 - An XFT track with $p_T > 8.34$ GeV associated with a CMX stub and CSX scintillator information.

- L2 - An XFT track with $p_T > 14.77$ GeV associated with a CMX stub.
- L3 - A minimum ionizing track with $p_T > 18$ GeV associated with a CMX stub with $|\Delta X_{\rm CMX}| < 10\,{\rm cm}$.

From Period 9 through Period 14, roughly half of the total data, alternate paths with various combinations of prescales and luminosity-enables were introduced to control the muon trigger rates at high instantaneous luminosity. Tables 5.1 and 5.2 list the single CMUP path and the single CMX path which provide the largest integrated luminosity for a given run range. These are the trigger paths I use.

Note that ELECTRON70_L2_JET serves as a fall-back path for the ELECTRON_CENTRAL_18 trigger, which may not fire for $E_T > 150$ GeV electrons because of saturation of the EM compartment fast readout electronics at Level 2. Figure 5.1, the dielectron mass spectrum for events which fire ELECTRON70_L2_JET but not ELECTRON_CENTRAL_18, shows that the backup path may indeed contribute additional high E_T events to the analysis.

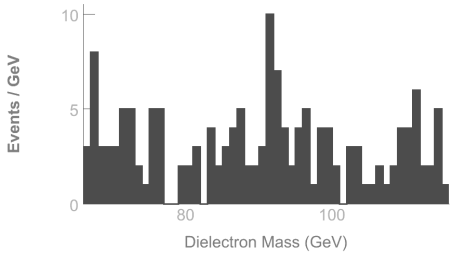

Figure 5.1: Dielectron mass distribution for events which fire ELECTRON70_L2_JET but not ELECTRON_CENTRAL_18, Periods 0–17.

Run Range		Trigger Path
138425	201349	MUON_CMUP18
201350	233111	MUON_CMUP18_L2_PT15
233133	261005	MUON_CMUP18

Table 5.1: CMUP trigger paths used.

Run Range		Trigger Path
138425	201349	MUON_CMX18
201350	223189	MUON_CMX18_L2_PT15
223233	226224	MUON_CMX18_L2_PT15_LUMI_200
226246	228596	MUON_CMX18_L2_LOOSE_LUMI_200
228664	237795	MUON_CMX18_LUMI_250
237845	256824	MUON_CMX18_DPS
256840	261005	MUON_CMX18

Table 5.2: CMX trigger paths used.

5.2.2 Data quality requirements and luminosity

My data quality criteria begin with version 23 of the CDF "good run lists" describing detector quality with standardized set of criteria. I identify electrons only during runs in the "em nosi" list (with active calorimetry and COT tracking) and muons only for runs in the "mu si" list (with active central muon chambers and silicon tracking). The latter choice simplifies bookkeeping but discards one excellent four muon SM ZZ candidate present in the early data. Table 5.3 lists the luminosity for each final state combination and trigger, integrated at fine time granularity using the "run sections" actually processed. I neglect the small

difference in luminosity between the two electron triggers. The luminosities involving CMX triggers are lower because of dynamic prescales and other rate suppression techniques discussed above. Luminosity differences are treated as additional channel inefficiencies in the final combination.

After imposing run quality criteria, I require the fitted position of the highest sum p_T reconstructed z vertex lie within 60 cm of the coordinate origin. This suppresses non-collision backgrounds and removes events with abnormal calorimeter topologies which might violate assumptions implicit in the standard jet energy corrections. Section 5.6.2 describes the efficiency of this requirement.

5.2.3 Simulated samples

To accompany the data, I simulate the samples listed in Table 5.4 for further checks, graviton signal acceptance estimates, and resonant background evaluation. For all samples, I have developed and use a version of the CDF event generation and simulation software, mcPRODUCTION 7.1.0 patch A, which includes the new calorimeter and other simulation improvements developed by others as well as the new tracking simulation and reconstruction. The new tracker simulation is important because of changes to the COT wire geometry description in the new reconstruction. I find that the new simulation adequately models all relevant aspects of the data, though I make small energy corrections

Final State	DQM Bits	Trigger	L (pb^{-1})
$ee\ ee$	em nosi	ELECTRON_CENTRAL_18	2932
$ee\ ee$	em nosi	ELECTRON70_L2_JET	2931
$ee\ \mu\mu$	em mu si	ELECTRON_CENTRAL_18	2662
$ee\ \mu\mu$	em mu si	ELECTRON70_L2_JET	2661
$ee\ jj$	em nosi	ELECTRON_CENTRAL_18	2932
$ee\ jj$	em nosi	ELECTRON70_L2_JET	2931
$\mu\mu\ \mu\mu$	mu si	MUON_CMUP18	2662
$\mu\mu\ \mu\mu$	mu si	MUON_CMX18	2545
$\mu\mu\ ee$	em mu si	MUON_CMUP18	2633
$\mu\mu\ ee$	em mu si	MUON_CMX18	2517
$\mu\mu\ jj$	mu si	MUON_CMUP18	2662
$\mu\mu\ jj$	mu si	MUON_CMX18	2545

Table 5.3: Integrated luminosities by final state and trigger combination for good run lists version 23.

noted below. The analysis is generally insensitive to the calorimeter simulation improvements.

The run dependence of my samples is simple. I generate an equal number of events to represent periods 0–13[1] with 14 runs which roughly characterize the detector conditions and average luminosity, as shown in Table 5.5. Note that the single Z samples are small relative to those used for precision measurements but provide the statistical precision on scale factors and acceptances than my analysis requires. Though I do not apply further weights to account for the luminosity or time profiles of my data samples, the small variations introduced by the run dependence are such that I can absorb the reweighting into various data/simulation ID scale factors.

[1] I had technical problems simulating events for Periods 14–17 and find the earlier periods sufficiently model the later periods.

Process	Simulation Version	Events Generated
SM $ZZ \to llll^a$	7.1.0 patch A	134000
SM $ZZ \to llll$ [a]	6.1.4 patch N	134000
SM $ZZ \to lljj$ [a]	7.1.0 patch A	134000
SM $ZZ \to lljj$ [a]	6.1.4 patch N	134000
SM $W^{\pm}Z \to ffll^b$	7.1.0 patch A	134000

continued on the next page...

[a] $l = e, \mu$; $M_Z > 15$ GeV

[b] $l = e, \mu$

continued from the previous page...

Process	Simulation Version	Events Generated
SM $W^{\pm}Z \to ffll$ [b]	6.1.4 patch N	134000
$Z \to ee$ [a]	7.1.0 patch A	135000
$Z \to \mu\mu$ [a]	7.1.0 patch A	135000
$Z \to \mu\mu$ [a]	6.1.4 patch N	135000
$G \to ZZ \to eeee$ [b], Herwig	7.1.0 patch A	13000
$G \to ZZ \to eeee$ [b], Herwig	6.1.4 patch A	13000
$G \to ZZ \to \mu\mu\mu\mu$ [b], Herwig	7.1.0 patch A	13000
$G \to ZZ \to \mu\mu\mu\mu$ [b], Herwig	6.1.4 patch N	13000
$G \to ZZ \to llll$ [b], Herwig	7.1.0 patch A	13000
$G \to ZZ \to llll$ [b], Herwig	6.1.4 patch N	13000
$G \to ZZ \to lljj$ [b], Herwig	7.1.0 patch A	13000
$G \to ZZ \to lljj$ [b], Herwig	6.1.4 patch N	13000
$G \to ZZ \to llll$ [c], Pythia	7.1.0 patch A	13000
$G \to ZZ \to llll$ [c], Pythia, More ISR	7.1.0 patch A	13000
$G \to ZZ \to llll$ [c], Pythia, Less ISR	7.1.0 patch A	13000

continued on the next page...

[a] $M_Z > 30$ GeV

[b] $M_G = 200, 300, ..., 1000$ GeV

[c] $M_G = 200, 500, 800$ GeV

continued from the previous page...

Process	Simulation Version	Events Generated
$G \to ZZ \to llll$ [c], Pythia, More FSR	7.1.0 patch A	13000
$G \to ZZ \to llll$ [c], Pythia, Less FSR	7.1.0 patch A	13000
$G \to ZZ \to lljj$ [c], Pythia	7.1.0 patch A	13000
$G \to ZZ \to lljj$ [c], Pythia, More ISR	7.1.0 patch A	13000
$G \to ZZ \to lljj$ [c], Pythia, Less ISR	7.1.0 patch A	13000
$G \to ZZ \to lljj$ [c], Pythia, More FSR	7.1.0 patch A	13000
$G \to ZZ \to lljj$ [c], Pythia, Less FSR	7.1.0 patch A	13000

Table 5.4: Simulated samples. The signal samples contain the number of events listed for each graviton mass.

Period	Run	Simulated Luminosity ($10^{30}\text{cm}^{-2}\text{sec}^{-1}$)
0	185542	87
1	193051	85
2	198082	94
3	198882	95
4	202771	93
5	206537	125
6	207079	133
7	211337	176
8	222271	202
9	224521	197
10	231179	228
11	235056	270
12	239230	233
13	242791	256

Table 5.5: The crude run dependence of all simulated samples.

5.3 Data reprocessing

I use my "backward tracking" algorithm for forward muon coverage and so must reprocess all relevant events with the new reconstruction. I estimate the CPU required to reprocess the entirety of both electron- and muon-triggered datasets is about 9600 CPU-Days, prohibitively large for a single person on practical timescales.

I therefore selectively reprocess only the subset of events relevant to my analysis. I first identify electron-triggered events for which the older software reconstructs a trigger electron plus either an additional electron or an anti-selected electron, as defined in Section 5.4. I also identify muon-triggered events with two tracks having either $p_T > 10$ GeV or $2 < p_T < 10$ GeV with a muon stub attached. Table 5.6 lists the fraction of benchmark signal events reconstructed selected by this procedure. I take the reprocessing procedure to be fully efficient for both *llll* and *llqq* modes.

I modify the internals of the data-retrieval software (APPFileInputModule) to reject events by comparing run and events numbers from the event header without reading the event data. The official APPFileInputModule reads events no faster than O(1 Hz) on a typical analysis farm node. Therefore, even

the null case in which no processing is done would take approximately 2600 CPU-Days without this modification. With it, that overhead is zero.

After testing the full procedure–with comparisons of exact event numbers requested and processed, dilepton (and anti-selected) mass spectra in the old and new versions of the data, etc.–I then run 7.1.0 Production on the 227,871,143 events in the 3 fb^{-1} trigger datasets using the modified APPFileInputModule to select only the 7,656,215 events of interest. Table 5.7 summarizes event counts for the various samples.

Graviton Mass (GeV)	*llll* Fraction	*llqq* Fraction
200	$0.99937^{+0.00036}_{-0.00058}$	$0.99613^{+0.00082}_{-0.00096}$
300	$0.99976^{+0.00018}_{-0.00037}$	$0.99605^{+0.00082}_{-0.00095}$
400	$0.99981^{+0.00014}_{-0.00029}$	$0.99806^{+0.00051}_{-0.00062}$
500	$0.99949^{+0.00025}_{-0.00037}$	$0.99863^{+0.00039}_{-0.00049}$
600	$1.00000^{+0}_{-0.00016}$	$0.99984^{+0.00011}_{-0.00023}$
700	$0.99984^{+0.00011}_{-0.00023}$	$0.99973^{+0.00015}_{-0.00025}$
800	$1.00000^{+0}_{-0.00014}$	$0.99972^{+0.00016}_{-0.00026}$
900	$1.00000^{+0}_{-0.00018}$	$0.99952^{+0.00023}_{-0.00034}$
1000	$1.00000^{+0}_{-0.00019}$	$0.99942^{+0.00028}_{-0.00042}$

Table 5.6: Fraction of 7.1.0-reconstructed benchmark four-body graviton events which meet the 6.1-based two-lepton reprocessing criteria. The $\mu\mu\mu\mu$ ratio drops with increasing mass as the fraction of near-forward muons increases.

5.4 Lepton and jet selection

Searches at CDF often start with standard object reconstruction and identification, then optimize signal to background by introducing cuts on the event topology and kinematics. That approach fails this signature for two reasons. The first is that there are no backgrounds to suppress, and the second is that with the CDF standard lepton criteria there is no signal.

My optimization strategy comes from the following consideration. If to identify a lepton candidate one applies ten uncorrelated cuts, each 99% efficient for real leptons, the combined efficiency of those cuts is about 90%. To select four leptons in this way, the combined efficiency is $0.99^{40} = 67\%$. If each cut is instead 95% efficient, the combined efficiency for four leptons is 13%. Thus, small increases in reconstruction and identification efficiency can be very important, and it is crucial to make no more cuts than necessary.

It is also important to note that large M_X leads to a pair of highly boosted Z bosons. When one of these Z bosons decays perpendicular to the Z flight direction, the decay products are both moderately boosted to 100 GeV-scale energies in the detector frame. However, when the decay occurs nearly parallel to the Z flight direction, the two particle energies are asymmetric. The particle decaying in the flight direction gets boosted to very high energy and the particle decaying

Sample	Number of Events	Number Selected	Fraction Selected
BHEL0D Period 0	26499559	617946	0.023
BHEL0H Periods 1–4	20026640	596966	0.029
BHEL0I Periods 5–9	28940435	850132	0.029
BHEL0J Periods 10–13	43850838	1220035	0.028
BHEL0K Periods 14–15	13704080	281802	0.021
BHEL0K Period 16	9238392	152974	0.017
BHEL0K Period 17	14219411	226422	0.016
BHMU0D Period 0	6629079	261702	0.039
BHMU0H Periods 1–4	5769255	293126	0.051
BHMU0I Periods 5–9	8853061	507854	0.057
BHMU0J Periods 10–13	17292745	945610	0.055
BHMU0K Periods 14–15	10820945	559701	0.052
BHMU0K Period 16	9026593	455235	0.050
BHMU0K Period 17	13000110	686710	0.053
Total BHEL	156479355	3946277	0.025
Total BHMU	71391788	3709938	0.052

Table 5.7: Events meeting reprocessing criteria by sample.

opposite the flight direction gets boosted to very low energy. For example, for $M_X = 500$ GeV the boost can produce one lepton with $p_T > 200$ GeV and the other with $pT < 10$ GeV. Thus, for the analysis to remain efficient at very high M_X, the lepton reconstruction must be sensitive to both extremes.

Sections 5.4.1 and 5.4.2 discuss the resultant selection criteria for electrons and muons reconstructed in the various subdetectors. Each event must contain a single lepton satisfying ID criteria slightly tighter than the trigger. After the trigger lepton selection, I select any other leptons using simple cuts which are generally more efficient than the trigger lepton selection. I continue to use the very loose electron selection designed during the earlier published $X \rightarrow ZZ \rightarrow eeee$ search [37]. This electron selection was primarily the work of Ben Brau, a former UCSB postdoc. To it, I add new, very loose muon identification criteria which increase multilepton signal efficiency for both central and forward muons and use my contributions to the track reconstruction for greater forward muon acceptance.

5.4.1 Electron ID

The electron criteria are almost identical to the earlier published analysis. Electrons are reconstructed by clustering the energy in contiguous calorimeter towers, or by isolated tracks pointing to cracks in the calorimeter. For central

CEM electrons, the highest p_T track pointing to the calorimeter cluster is also used. The transverse energy computation, $E_T = Esin\theta$, uses the polar angle obtained from the track. Forward PEM electrons without a track obtain the polar angle from the highest sum p_T z vertex and the cluster position. The calorimeter selection employs two calorimeter energy variables: the ratio of HAD to EM compartment energies and the ratio of the "isolation" energy in a cone surrounding the cluster to the electron energy. Jet constituents will tend to spread energy throughout the isolation cone and, as discussed earlier, shower predominantly in the hadronic calorimeter. Electron showers are spatially narrow and occur mainly in the EM compartment. Thus, both variables will be large for jets and small for electrons. The track-only electrons employ a single track-based isolation variable. Several ancillary variables are applied to electrons with tracks in order to reject particles not originating from the collision vertex.

The salient differences with the published analysis are:

1. I constrain the track to pass through the time-averaged transverse beam position (the "beamline") and correct the curvature in the same way as muons.

Central Electron Selection
CEM Cluster Only
Matching PAD Track
Fiducial = 1
$E_T^{cal} > 5\,\text{GeV}$
$\lvert z_0^{trk} \rvert < 60\,\text{cm}$
$E_{HAD}/E_{EM} < 0.055\,\text{GeV} + 0.00045 * E^{cal}$
$Isol^{cal}/E^{cal} < 0.2$

Table 5.8: Central electron selection.

2. The energy resolution function now incorporates an uncertainty which is linear in the electron energy. This term should not be neglected for high energy electrons.

Forward Electron Selection
PEM Cluster Only
$\lvert\eta_{det}\rvert < 2.5$
$E_T^{cal} > 5\,\text{GeV}$
$E_{HAD}/E_{EM} < 0.05\,\text{GeV}$
$Isol^{cal}/E^{cal} < 0.2$

Table 5.9: Forward electron selection.

Track Electron Selection
PAD Track Only
Track is Not Fiducial in the CES
$\Delta r_{\eta\phi} > 0.2$ with all other electrons
$p_T \geq 10\,\mathrm{GeV}$
$\lvert z_0 \rvert < 60.\,\mathrm{cm}$
Axial COT Segments ≥ 3
Stereo COT Segments ≥ 2
$\lvert d_0 \rvert < \begin{cases} 200\,\mu m & \text{if } N_{si} > 0 \\ 2\,mm & \text{if } N_{si} = 0 \end{cases}$
$Isol^{trk}/p_T^{trk} > 0.9$

Table 5.10: Track electron selection.

Trigger Electron Selection
CEM Cluster Only
Matching PAD Track
Fiducial = 1
$E_T^{cal} > 20\,\text{GeV}$
$p_T^{trk} > 10\,\text{GeV}$
$\lvert z_0^{trk} \rvert < 60\,\text{cm}$
$E_{HAD}/E_{EM} < 0.055\,\text{GeV} + 0.00045 * E^{cal}$
$Isol^{cal}/E^{cal} < 0.2$
$Lshr_{trk} < 0.4$
$\lvert \Delta z_{trk-CES} \rvert < 8.0\,\text{cm}$

Table 5.11: Trigger electron selection.

5.4.2 Muon ID

My muon selection makes no muon chamber requirements (except when required to fire the trigger) and relies on relatively loose minimum-ionization, isolation calorimeter, and track quality requirements to reject fake backgrounds. The cut values for the calorimeter cuts are simply double the CDF "Joint Physics" recommended values. This provides small but important increases in their overall efficiencies and partially stabilizes the effects of the cuts at high luminosity and low momentum. Since I reconstruct some non-trigger muons through tracking algorithms never before used in an analysis, I have carefully studied purity and momentum resolution while developing the algorithms and apply that knowledge here. My track quality criteria reject tracks with obviously bad fit probability and poorly-measured tracks indistinguishable from a straight line. I make no direct COT hit requirements other than the quality cuts imposed within the algorithms themselves, some of which were designed with this search in mind. The remainder of the track quality requirements ensure each track originates at the primary interaction vertex.

Muon Selection

$$p_T^{trk} > 2(10) \text{ GeV with(without) stub}$$

$$\kappa/\sigma_\kappa > 2.5$$

$$p(\chi^2, ndof) > 10^{-10}$$

$$|z_0^{trk}| < 60 \text{ cm}$$

$$|d_0| < \begin{cases} 200\ \mu m & \text{if } N_{si} > 0 \\ 2\ mm & \text{if } N_{si} = 0 \end{cases}$$

$$E_{EM} < 4 + max(0, 0.0115 * (\frac{p^{trk}}{\text{GeV}} - 100)) \text{ GeV}$$

$$E_{HAD} < 12 + max(0, 0.028 * (\frac{p^{trk}}{\text{GeV}} - 100)) \text{ GeV}$$

$$Isol/p^{trk} < 0.2$$

Table 5.12: Basic muon selection. Note that, for $p_T > 10$ GeV, there are no muon detector requirements.

CMUP Trigger Muon Selection

CT or OI Tracking Algorithms Only

CMU and CMP Stubs

CMP Stub $\notin$ bluebeam OR run ≥ 154449

$|\Delta x_{cmu}| < 10$ cm

$|\Delta x_{cmp}| < 20$ cm

$p_T^{trk} > 20\,\text{GeV}$

$\kappa/\sigma_\kappa > 2.5$

$p(\chi^2, ndof) > 10^{-10}$

$|z_0|60$ cm

$$|d_0| < \begin{cases} 200\,\mu m & \text{if } N_{si} > 0 \\ 2\,mm & \text{if } N_{si} = 0 \end{cases}$$

$Isol/p^{trk} < 0.2$

$E_{EM} < 4 + max(0, 0.0115 * (\frac{p^{trk}}{\text{GeV}} - 100))$ GeV

$E_{HAD} < 12 + max(0, 0.028 * (\frac{p^{trk}}{\text{GeV}} - 100))$ GeV

Table 5.13: CMUP trigger muon selection.

CMX Trigger Muon Selection

CT or OI Tracking Algorithms Only

CMX Stub

Run $\geq$ 150144

CMX Stub $\notin$ keystone OR run $\geq$ 186598

CMX Stub $\notin$ miniskirt OR (run $\geq$ 186598 AND wedge!=15,20)

$|\Delta x_{cmx}| < 10\,\text{cm}$

$p_T^{trk} > 20\,\text{GeV}$

$\kappa/\sigma_\kappa > 2.5$

$p(\chi^2, ndof) > 10^{-10}$

$|z_0|60\,\text{cm}$

$$|d_0| < \begin{cases} 200\,\mu m & \text{if } N_{si} > 0 \\ 2\,mm & \text{if } N_{si} = 0 \end{cases}$$

$Isol/p^{trk} < 0.2$

$E_{EM} < 4 + max(0, 0.0115 * (\frac{p^{trk}}{\text{GeV}} - 100))\ \text{GeV}$

$E_{HAD} < 12 + max(0, 0.028 * (\frac{p^{trk}}{\text{GeV}} - 100))\ \text{GeV}$

Table 5.14: CMX trigger muon selection.

Forward Muon ID Checks

Though the forward tracking algorithms make use of fewer hits in the COT, the resulting muons are consistent with being very pure. Comparisons of low-level muon and track variables between central and forward muons support this statement. I divide the muon acceptance into central ($|\eta_{trk}| < 1$), near forward ($1 < |\eta_{trk}| < 1.7$), and far forward ($1.7 < |\eta_{trk}| < 2$) regions. Figures 5.2 through 5.9 show individual muon ID and other quality variables after all other cuts have been applied. Note that all variables for both near and far forward muons closely resemble the distribution one expects for real muons. In particular, the hadronic calorimeter energy distribution for forward tracks has the expected shape, and the minimum-ionizing peak is qualitatively the same as the peak for central muons[1].

[1]One should not expect an exact match; the forward calorimeter design differs from the central calorimeter design, and the average forward tower energy is higher because of the underlying event and other backgrounds.

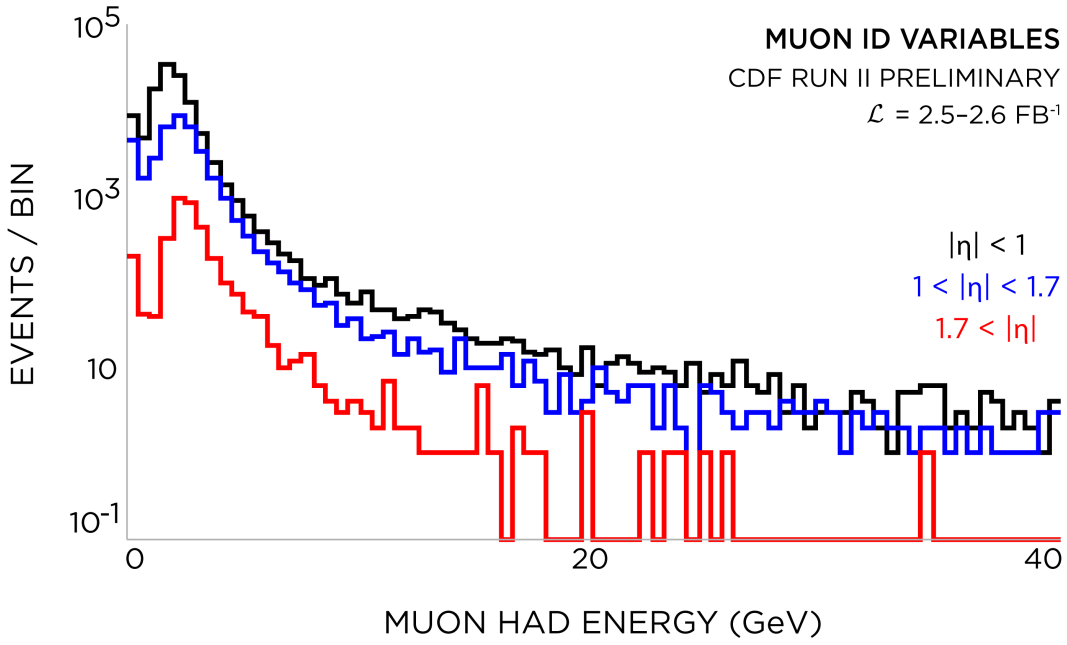

Figure 5.2: Comparison of HAD energy (GeV) for (black) central (blue) near forward and (red) far forward muons, all other cuts applied.

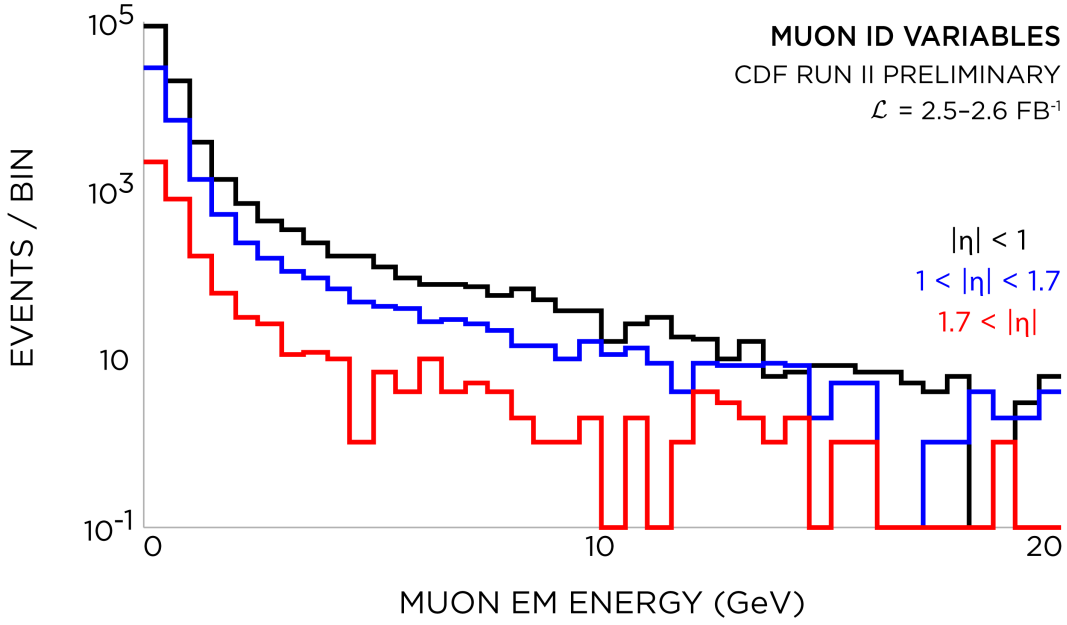

Figure 5.3: Comparison of EM energy (GeV) for (black) central (blue) near forward and (red) far forward muons, all other cuts applied.

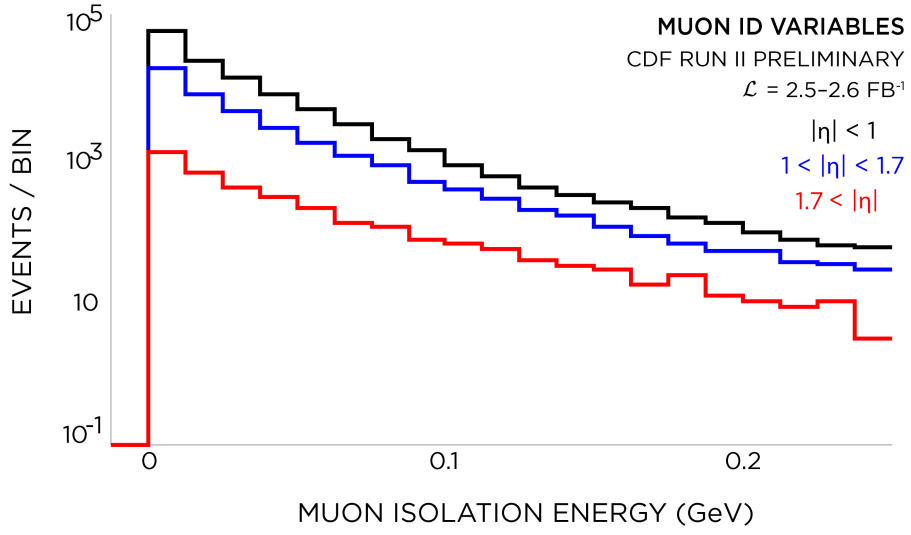

Figure 5.4: Comparison of isolation ratio for (black) central (blue) near forward and (red) far forward muons, all other cuts applied.

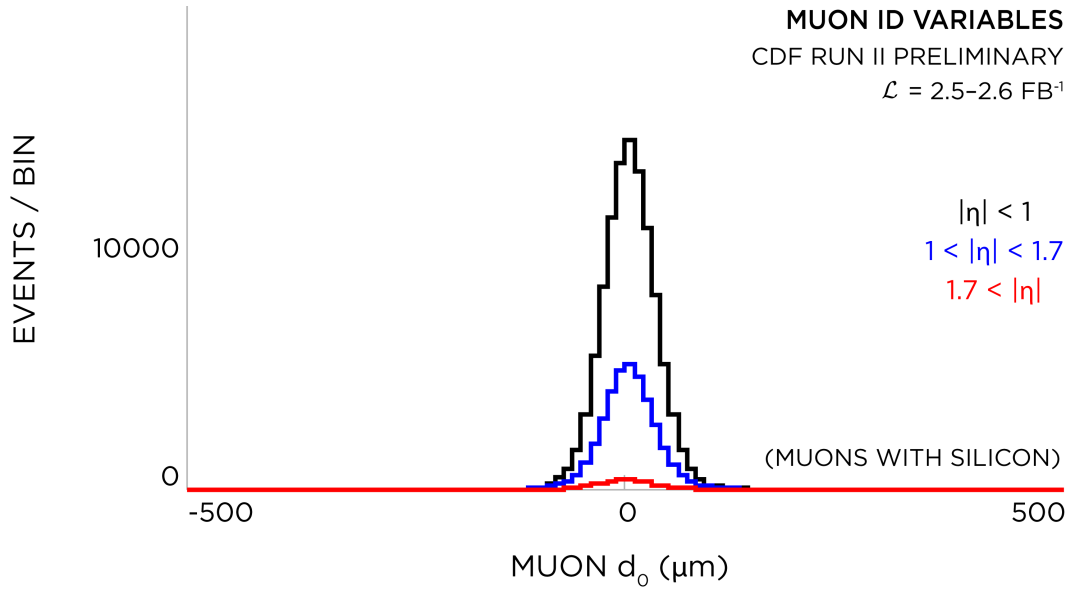

Figure 5.5: Comparison of d_0 (cm) for (black) central (blue) near forward and (red) far forward muons, all other cuts applied.

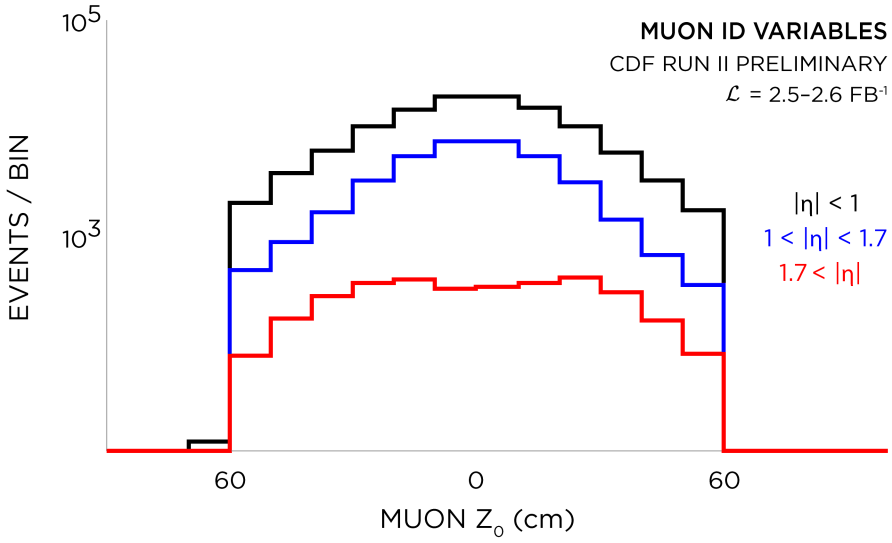

Figure 5.6: Comparison of z_0 (cm) for (black) central (blue) near forward and (red) far forward muons, all other cuts applied.

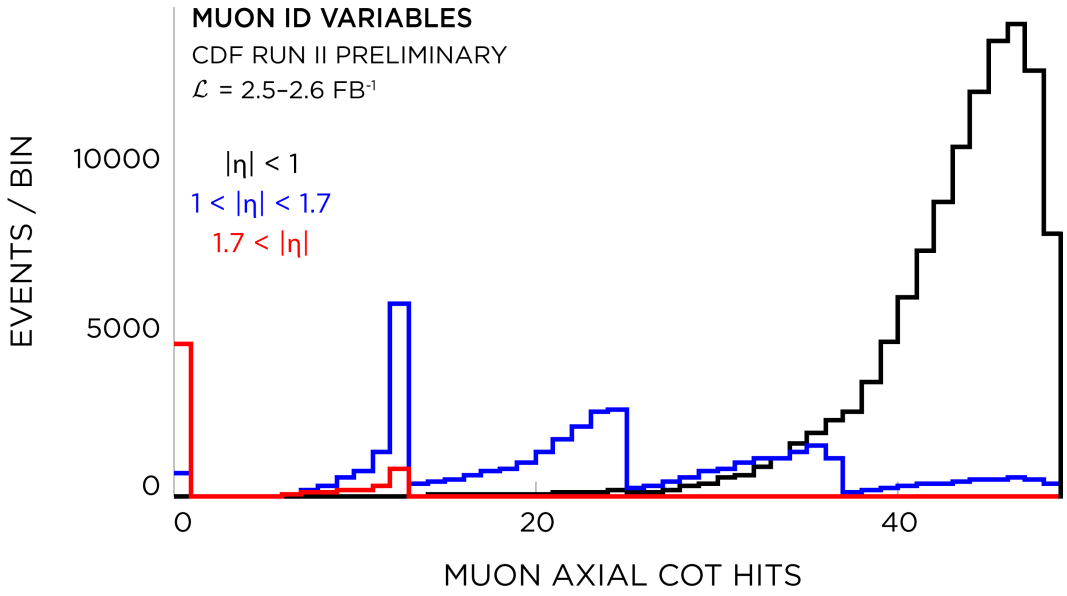

Figure 5.7: Comparison of COT axial hit multiplicity for (black) central (blue) near forward and (red) far forward muons, all other cuts applied.

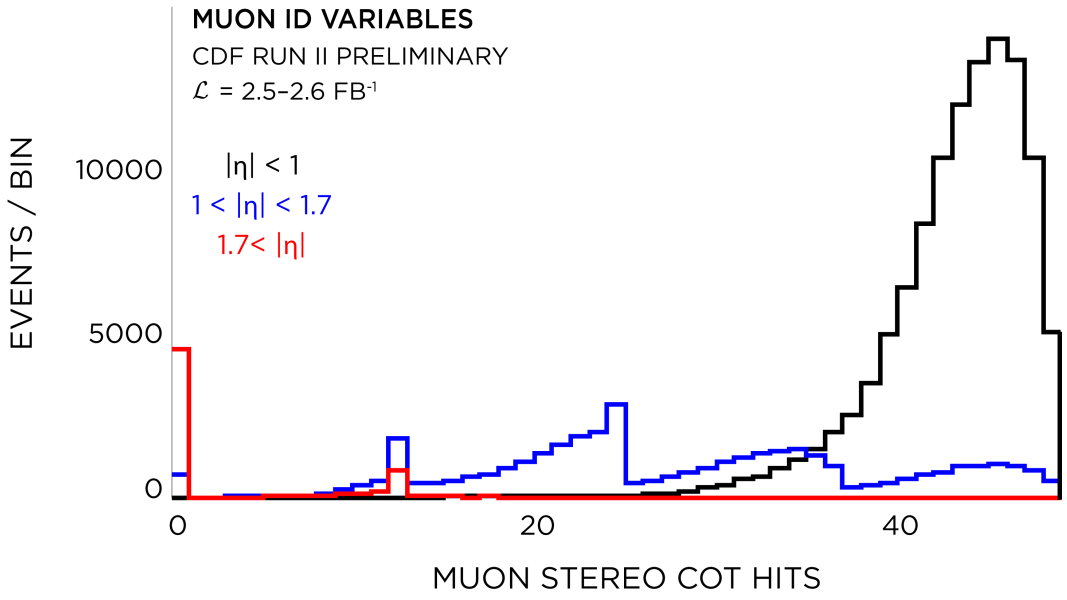

Figure 5.8: Comparison of COT stereo hit multiplicity for (black) central (blue) near forward and (red) far forward muons, all other cuts applied.

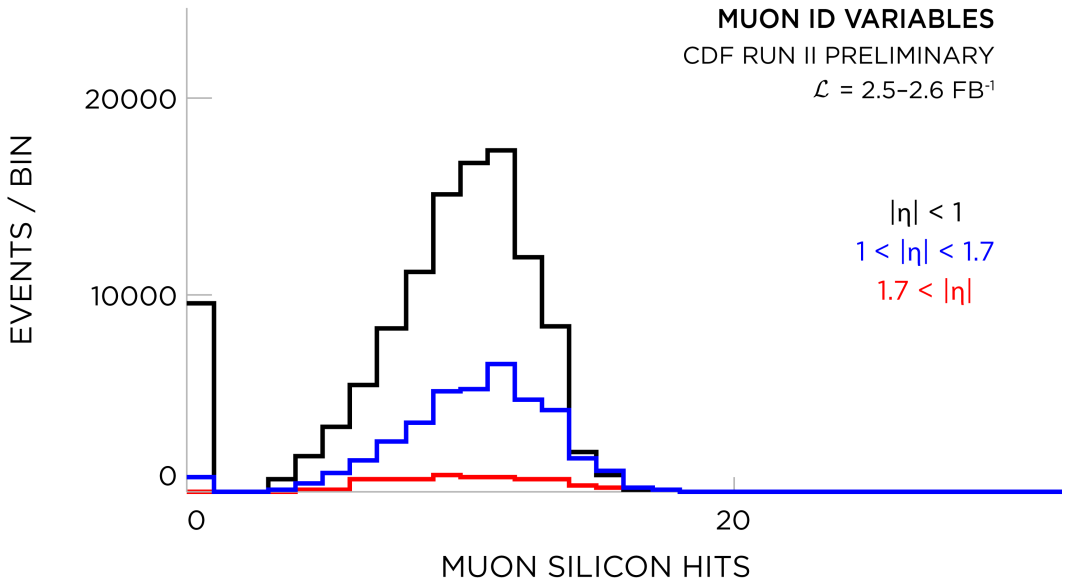

Figure 5.9: Comparison of silicon hit multiplicity for (black) central (blue) near forward and (red) far forward muons, all other cuts applied.

5.4.3 Lepton selection comparison

Figures 5.10 and 5.12 compare the dilepton mass spectra resulting from this selection with that of the widely-used[1] electron and muon criteria. Note that the lack of muon chamber requirements does not result in a large combinatoric background which would indicate a high muon fake rate; muon-like calorimeter ID cuts can suppress most fake muon background without making use of the muon chambers for non-trigger muons. By dropping those requirements, muon acceptance is limited only by tracking efficiency and calorimeter coverage.

[1] e.g. [2]

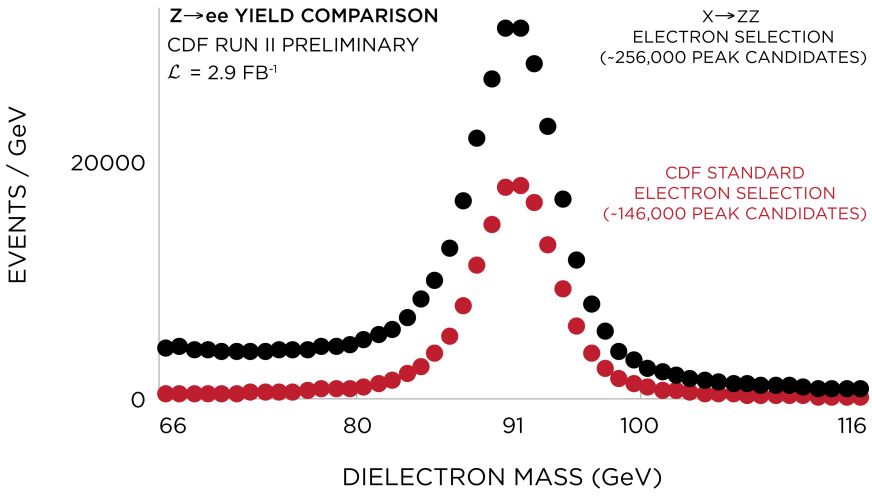

(a)

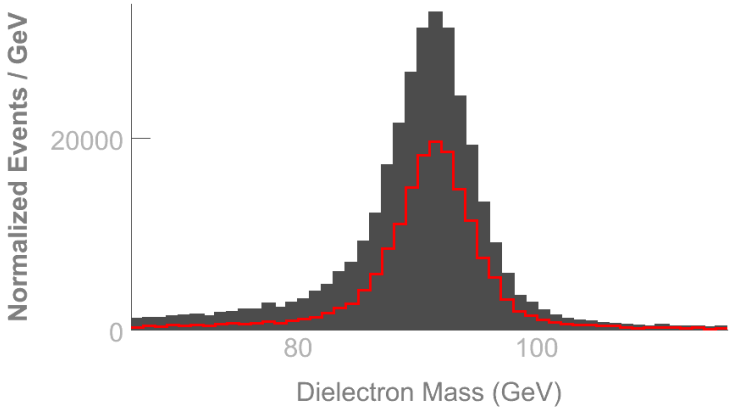

(b)

Figure 5.10: Dielectron mass distribution in (a) data and (b) simulation for my selection (black/gray) and the standard loose CDF selection (red).

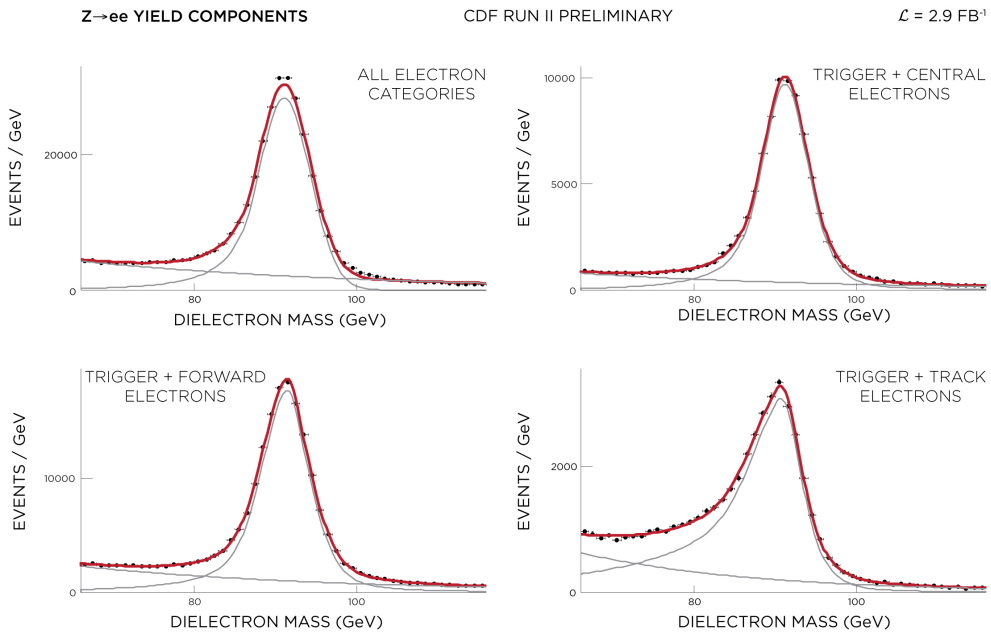

Figure 5.11: Dielectron mass spectra split by electron categories.

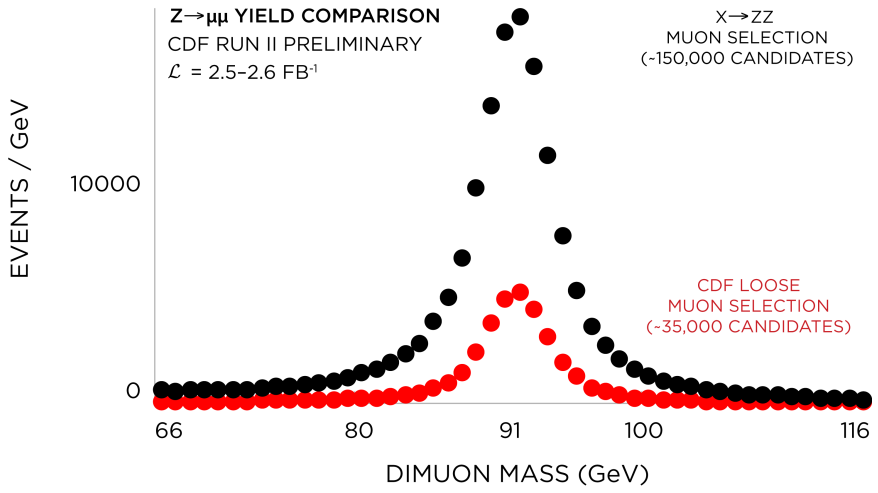

(a)

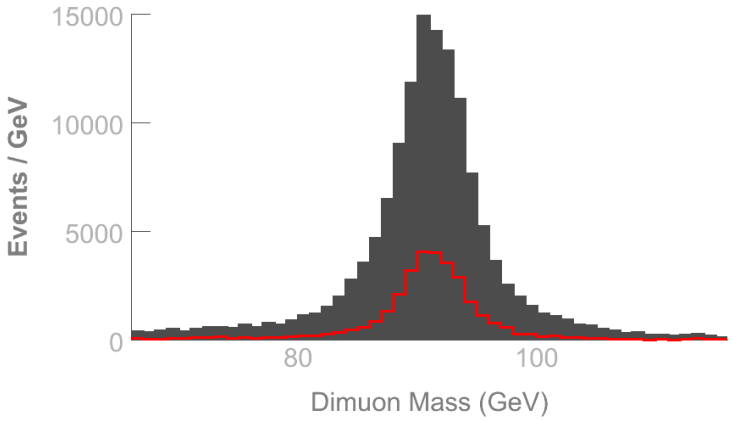

(b)

Figure 5.12: Dimuon mass distribution in (a) data and (b) simulation for my selection (black/gray) and the standard CMUP and CMX CDF selections (red) removing cosmics as described in Section 5.6.1.

5.4.4 Jet ID

I consider jet candidates when reconstructing the dilepton + jets decay modes of ZZ pairs but do not make any jet requirements when reconstructing other modes. From the output of the JETCLU 0.4 cone algorithm [99], I require $E_T^{raw} > 10$ GeV and $|\eta_{\text{jet centroid}}| < 3.64$. Clustering algorithms can also build jets out of electron clusters, so I discard any candidates having

$$\sqrt{(\eta_{\text{jet centroid}} - \eta_{\text{ele}})^2 + (\phi_{\text{jet centroid}} - \phi_{\text{ele}})^2} < 0.4$$

with an electron candidate and any jet candidates with over 95% of the total raw jet energy in the electromagnetic portion of the calorimeter.

When the high mass $X \rightarrow ZZ$ signature produces low E_T jets, the boost is such that the four-body mass is sensitive to the angular distribution but insensitive to the energy of the low E_T daughters. Thus it is important to maintain efficiency, but not necessarily energy resolution, at low jet E_T. At such low energies, disassociated calorimeter activity may result in spurious low-E_T "jets," and my background estimation consists of fits to sideband data which include this component.

5.5 Energy corrections

After reprocessing my data with the new reconstruction, I observe that the peak of the CEM + CEM dielectron mass spectrum occurs between about 90.2 and 91.2 GeV, with apparently random variation between the 4 arches and the 18 run periods. A mistake of this order is large enough to affect the χ^2_{ZZ} calculation, so I correct for this effect by scaling all CEM electron four-momenta by a period-dependent factor listed in Table 5.15. These rescale the mean of fits to a Breit-Wigner $\otimes$ Gaussian signal PDF and an exponential background PDF. After applying the CEM correction, the CEM + PEM dielectron spectra behave similarly, and therefore I multiply PEM electron four-momenta by the period-dependent data/simulation scale factors also listed in Table 5.15.

I constrain all track electrons and muons to pass through the beamline, regardless of silicon attachment, except when the track is a "forward" track (the backward, Inside-Out, and silicon standalone algorithms). The latter often have few or no COT hits and therefore the beam constraint is either unreliable or inapplicable. I apply "Larry" momentum corrections, obtained from the 2.4 fb^{-1} W mass analysis and the recent high mass dimuon search, to all beam-constrained tracks in order to compensate for COT twists and other geometric effects not removed by the internal alignment. After making this correction, I observe the Z

peak position varies by 0.5–2 GeV and so apply period- and algorithm-dependent scale factors listed in Table 5.16. The silicon standalone momentum resolution is much worse than the resolution of the other algorithms (and/or the sample is virtually all background), making a peak correction unnecessary. All other corrections are the result of fits to pairs of one Outside-In track and one track of the relevant algorithm after first correcting the $OI + OI$ spectrum.

After correcting the data, I derive separate, period-independent scale factors for my simulation through an identical procedure. Table 5.17 shows these scale factors.

I correct all jets using the full set of standard CDF jet energy corrections ("Level 7") using the most recent version of the software ("JetUser version jetCorr15").

Period	CEM	West PEM	East PEM
0	1.002	1.006	1.009
1	1.005	1.010	1.010
2	1.006	1.007	1.008
3	1.004	1.007	1.011

continued on the next page...

continued from the previous page...

Period	CEM	West PEM	East PEM
4	1.007	1.007	1.006
5	1.006	1.007	1.008
6	1.003	1.007	1.008
7	1.004	1.009	1.008
8	1.005	1.009	1.012
9	1.006	1.009	1.009
10	1.008	1.007	1.009
11	1.007	1.008	1.009
12	1.011	1.006	1.008
13	1.010	1.007	1.007
14	1.005	1.006	1.010
15	1.010	1.007	1.009
16	1.008	1.009	1.011
17	1.008	1.009	1.008

Table 5.15: Calorimeter four-momenta scale factors.

Period	Outside-In	COT St.	Backward	Inside-Out
0	1.00349	0.99923	1.0021	1.00743
1	1.00382	1.00933	0.99737	1.01271
2	1.00437	1.00000	1.01148	1.00099
3	1.00470	0.99912	0.99235	1.01408
4	1.00382	1.00165	1.00420	1.01611
5	1.00404	1.00199	1.00088	0.99802
6	1.00371	0.99912	1.00765	1.03005
7	1.00382	1.00487	1.01023	1.00933
8	1.00437	1.00154	0.99901	1.00210
9	1.00437	1.00033	0.99989	1.00878
10	1.00404	1.00011	1.00821	0.98825
11	1.00404	1.00044	1.00699	1.00132
12	1.00393	1.00232	1.00743	0.98836
13	1.00382	1.00165	1.01124	0.99279
14	1.00305	0.99923	1.02376	1.00787
15	1.00338	1.00099	1.01011	0.99214

continued on the next page...

Algorithm	Scale Factor
OI	1.004
COT	1.00654
BW	1.00783
IO	0.999783

Table 5.17: Simulation track four-momenta scale factors.

continued from the previous page...

Period	Outside-In	COT St.	Backward	Inside-Out
16	1.00349	1.00431	1.00077	1.00409
17	1.00316	1.00044	1.01000	1.01678

Table 5.16: Track four-momenta scale factors for Outside-In, COT standalone, Backward, and Inside-Out tracks.

5.6 Z and X construction

After identifying and correcting electrons, muons, and jets, I construct all possible dielectron, dimuon, and dijet combinations, here labeled generically as Z bosons despite the lack of a requirement that the two-body mass lie in any window. I discard all two-track dielectron and dimuon pairs with inconsistent z production positions ($|\Delta z_0| > 5$ cm.) When considering a single Z per event, at least one lepton must satisfy the tighter trigger lepton selection. I do not require that any track pair is charge-neutral.

For $X \to ZZ$ reconstruction, only one Z must contain a trigger lepton. I also require that $dr = \sqrt{\Delta\eta^2 + \Delta\phi^2}$ between any two final states satisfy $dr > 0.2$ and that each Z have $M_Z > 20$ GeV. Both of these latter criteria suppress pairs of collinear, low-momentum tracks which would otherwise populate the sideband samples I use to estimate fake lepton backgrounds.

I calculate the invariant mass after applying the energy corrections described above (Section 5.5). For the lepton channels, I determine a total mass uncertainty for each Z by propagating the measurement uncertainties on each lepton.

- The CEM electron energy uncertainty is $\sigma^2_{\mathrm{CEM}} = 0.135^2 E + 0.015^2 E^2$.
- The PEM electron energy uncertainty is $\sigma^2_{\mathrm{PEM}} = 0.16^2 E + 0.01^2 E^2$.

- The track electron and muon energy uncertainties come from the fitted track curvature uncertainty after applying an algorithm-dependent scale factor. I measure each scale factor in $Z \to \mu\mu$ events. Though track resolution is a complicated function of track kinematics and detector acceptance, the mass pull distribution is roughly Gaussian, and I iteratively adjust the scale factor until the pull distribution for each algorithm has a unit width core.

Each Z mass uncertainty is then the sum in quadrature of the mass uncertainty derived from the above and a constant term $\sigma_\Gamma = 3.25$ accounting for the non-Gaussian Z line shape.

When more than one Z combination exists for an event, I choose the combination which minimizes

$$\chi^2_Z = \Big(\frac{|M_Z - 91.187 \text{ GeV}|}{\sqrt{\sigma^2_M + \sigma^2_\Gamma}}\Big)^2$$

for single Z studies.

For all $X \to ZZ \to llll$ combinations, I compute the ZZ mass χ^2

$$\chi^2_{ZZ} = \frac{(M^{(1)}_Z - 91.187 \text{ GeV})^2}{\sigma^2_{M^{(1)}} + \sigma^2_\Gamma} + \frac{(M^{(2)}_Z - 91.187 \text{ GeV})^2}{\sigma^2_{M^{(2)}} + \sigma^2_\Gamma}$$

quantifying resemblance to a pair of pole Z bosons. When more than one $X \to ZZ \to llll$ combination exists for an event, I select the lowest χ^2_{ZZ} combi-

nation. My blinded search region is then $M_X > 300\ GeV$ and $\chi^2_{ZZ} < 50$, which is equivalent to a 5σ Z mass cut on each of the dilepton masses.

For the $X \to ZZ \to lljj$ search, I define the signal region to be $\chi^2_Z(Z \to ll) < 25$ (5σ), $65 < M_{qq} < 120$ GeV, and $M_X > 300$ GeV. There are often more than two jets with $E_T > 5$ GeV found in Z events, increasing the chance that one can find a pair with dijet mass near the Z pole, and thus the lowest χ^2_{ZZ} choice biases the M_{qq} spectrum of the background[1]. When reconstructing more than one $X \to ZZ \to lljj$ combination in an event, I avoid this bias by choosing the $Z \to ll$ pairing with the smallest Z mass pull and the $Z \to jj$ pairing with the two highest E_T jets.

5.6.1 Cosmic removal

Cosmic ray muons passing through the tracking volume will be reconstructed as one or more minimum-ionizing tracks, a potential background for the muon and track electron selection. If the entire muon trajectory is reconstructed, the result will be two oppositely-charged tracks, one inward-moving leg and one outward-moving leg. While my non-resonant background estimation procedure

[1]In the four lepton modes this effect is negligible because five or more leptons are rarely reconstructed.

will include this contribution, I nevertheless use COT timing to reject Z candidates constructed from track pairs.

Figure 5.13a shows a distribution of the unsigned difference between the per-muon track production times (t_0) fitted from the COT drift times of their constituent hits. There are two populations. Z decays dominate the population peaked near zero, with a width set by the longitudinal extent of the interaction region. Cosmics comprise the population peaked near 6 ns (the time taken for a typical cosmic to cross the COT). As in [64], I reject muon and track electron pairs with $\Delta t_0 > 3$ ns. To illustrate the effect of the cut, the mass distributions for dimuon events in the first ≈ 330 pb^{-1} of data passing and failing this cut appear in Figure 5.13b for all events in the unfiltered sample processed with the older "6.1" software.

I construct the above distributions for each data period in the reprocessed sample and, observing no statistically significant time dependence, treat all periods collectively (Figure 5.14.) I measure the fraction of dimuon pairs with $66 < M_Z < 116$ GeV which survive the veto to be $0.99509^{+0.00018}_{-0.00018}$ in data and $0.99904^{+0.00018}_{-0.00020}$ in simulation, resulting in a scale factor of 0.99604 ± 0.00027. In a cosmics-enriched subsample of events with exactly two reconstructed tracks[1],

[1]Recall that the 7.1.0 reprocessing filter requires at least two tracks with collision-like impact parameter cut.

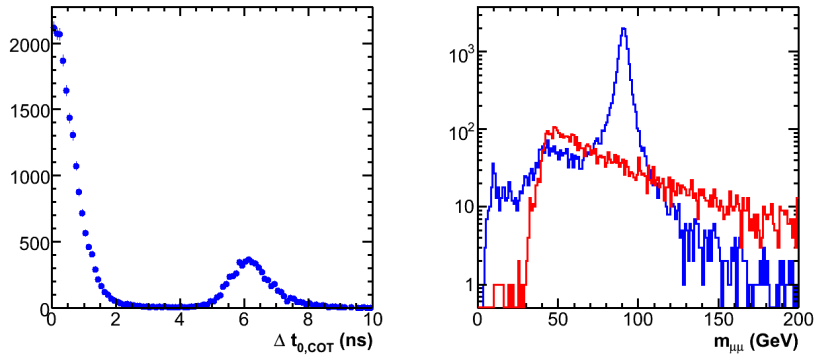

(a) (b)

Figure 5.13: Cosmic rejection in unfiltered 6.1 data: (a) Δt_0 distribution for dimuon pairs in HIGH_PT_MUON data (bhmu0d only) for the trigger+minimal selection (b) dimuon mass distribution for $\Delta t_0 < 3$ ns (blue) and $\Delta t_0 > 3$ ns (red).

I find that, outside the 66–116 GeV window where there is a small Z peak, the fraction of events which survive the veto is $0^{+0.002}_{0}$. Therefore I take the surviving cosmic ray background to be zero for both the $X \to ZZ \to llll$ and $X \to ZZ \to lljj$ channels.

5.6.2 Z cross section measurement

As a test of my understanding of the dilepton data and simulation, I measure the Z cross section in the 66–116 GeV dilepton mass range for both electron-

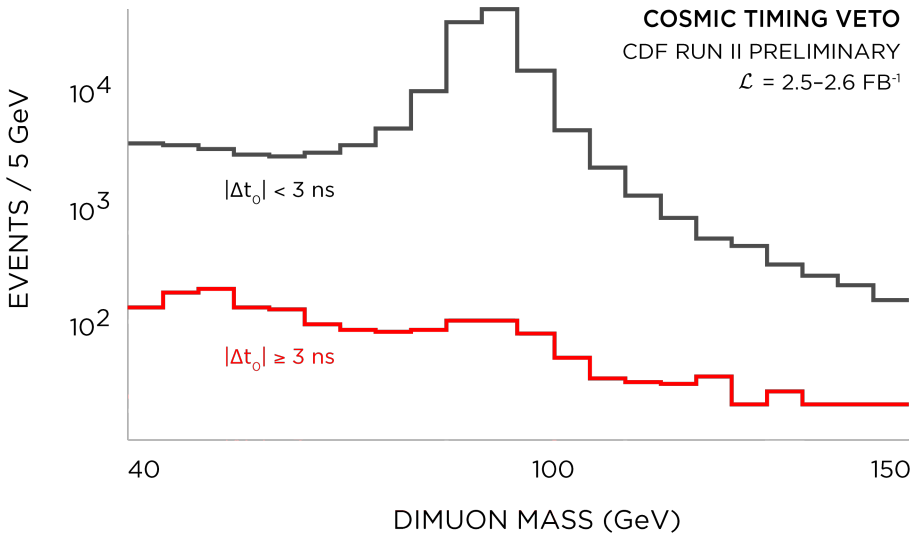

Figure 5.14: Dimuon mass distribution for (gray) $\Delta t_0 < 3$ns and (red) $\Delta t_0 > 3$ns, Periods 0–17.

and muon-triggered samples. The cross section is given by

$$\sigma(Z \to ll, 66\text{–}116) = \frac{N_{obs}}{L \times \mathrm{acc}_{mc} \cdot \epsilon_{mc} \times \epsilon_{data/mc}}$$

where

$$\epsilon_{data/mc} = \epsilon_{trig} \times \mathrm{sf}_{\text{id,CEM trigger}} \times \mathrm{sf}_{\text{id,electron}} \times \mathrm{sf}_{\text{ZVERTEX}} \times \mathrm{sf}_{\text{cosmic veto}} \times \mathrm{sf}_{\text{avg},\Delta z_0}$$

for the dielectron measurement and

$$\epsilon_{data/mc} = \epsilon_{trig} \times \mathrm{sf}_{\text{id,CMUP trigger}} \times \mathrm{sf}_{\text{id,muon}} \times \mathrm{sf}_{\text{ZVERTEX}} \times \mathrm{sf}_{\text{cosmic veto}} \times \mathrm{sf}_{\Delta z_0}$$

for the dimuon measurement, N_{obs} is the number of signal events observed in data, L is the sample luminosity, $\mathrm{acc}_{mc} \cdot \epsilon_{mc}$ is the acceptance · efficiency from simulation, ϵ_{trig} is the average trigger efficiency weighted by acceptance, and sf_i is the scale factor associated with a particular set of cuts. I compute scale factors for each lepton selection, the z vertex requirement, the cosmic veto, and the track pair Δz_0 requirement. The track pair scale factors compare efficiencies weighted by the fraction of simulated events for which two tracks are present. Except for the cosmic veto scale factor taken from Section 5.6.1, all scale factors are treated as period-dependent.

Electron Trigger Efficiency

The standard CEM electron trigger efficiency has been measured to be 0.979 ± 0.003. My trigger electron selection is sufficiently similar, and the two-

electron trigger efficiency sufficiently high, that I assume this value. The cross section measurement is a check of this assumption.

Muon Trigger Efficiencies

Since both the tracking algorithms and the muon reconstruction changed between the old and new software releases, I remeasure the CMUP and CMX trigger efficiencies by selecting pairs of triggerable muon candidates in the 81–101 GeV dimuon mass range, requiring one muon fire the relevant trigger, and recording the efficiency for the other muon to fire the appropriate trigger. This is essentially the same procedure CDF uses to measure the standard trigger efficiencies and produces compatible numbers when applied to the standard muon selection. Table 5.18 lists the single muon trigger efficiencies as a function of time.

After measuring the per-muon trigger efficiencies, I apply weights derived from the acceptance in simulation to obtain average CMUP and CMX efficiencies. In doing so I consider an event which fires both triggers to have fired only the CMUP trigger. The weighting formulas are

$$\epsilon_{\mathrm{CMUP},Z} = \frac{1}{f_{\mathrm{TrigCMUP,TrigCMUP}} + f_{\mathrm{TrigCMUP,!TrigCMUP}}} \cdot \Big(f_{\mathrm{TrigCMUP,TrigCMUP}}(1-(1-\epsilon_{\mathrm{Trig,CMUP}})^2) + f_{\mathrm{TrigCMUP,!TrigCMUP}}\epsilon_{\mathrm{Trig,CMUP}} \Big)$$

$$\epsilon_{\mathrm{CMX},Z} = \frac{1}{f_{\mathrm{TrigCMX,TrigCMX}} + f_{\mathrm{TrigCMUP,TrigCMX}} + f_{\mathrm{TrigCMUP,!Trig}}} \cdot$$
$$\Big(f_{\mathrm{TrigCMX,TrigCMX}}(1 - (1 - \epsilon_{\mathrm{Trig,CMX}})^2) +$$
$$f_{\mathrm{TrigCMUP,TrigCMX}}(1 - \epsilon_{\mathrm{Trig,CMUP}})\epsilon_{\mathrm{Trig,CMX}} +$$
$$f_{\mathrm{TrigCMX,!Trig}}\epsilon_{\mathrm{Trig,CMX}} \Big)$$

where $f_{\mathrm{TrigCMUP,TrigCMUP}}$ is the fraction of reconstructed events in simulation with both muons satisfying the CMUP trigger muon selection, $\epsilon_{\mathrm{Trig,CMUP}}$ is the single-muon CMUP trigger efficiency, $f_{\mathrm{TrigCMUP,!TrigCMUP}}$ is the fraction of reconstructed events in simulation with only one muon satisfying the CMUP trigger selection, $f_{\mathrm{TrigCMX,TrigCMX}}$ is the fraction with both muons satisfying the CMX trigger muon selection, etc.

Period	CMUP	CMX
0	$0.8985^{+0.0053}_{-0.0053}$	$0.904^{+0.010}_{-0.011}$
1	$0.9035^{+0.0093}_{-0.0098}$	$0.849^{+0.019}_{-0.020}$
2	$0.9308^{+0.0072}_{-0.0077}$	$0.856^{+0.017}_{-0.018}$
3	$0.9303^{+0.0093}_{-0.0101}$	$0.848^{+0.022}_{-0.023}$
4	$0.9269^{+0.0095}_{-0.0104}$	$0.843^{+0.023}_{-0.025}$

continued on the next page...

continued from the previous page...

Period	CMUP	CMX
5	$0.9219^{+0.0075}_{-0.0079}$	$0.883^{+0.015}_{-0.015}$
6	$0.9164^{+0.0087}_{-0.0092}$	$0.887^{+0.017}_{-0.018}$
7	$0.937^{+0.013}_{-0.015}$	$0.923^{+0.023}_{-0.026}$
8	$0.9210^{+0.0062}_{-0.0065}$	$0.861^{+0.014}_{-0.015}$
9	$0.9435^{+0.0055}_{-0.0058}$	$0.868^{+0.014}_{-0.015}$
10	$0.9320^{+0.0050}_{-0.0053}$	$0.885^{+0.011}_{-0.011}$
11	$0.9380^{+0.0051}_{-0.0054}$	$0.865^{+0.013}_{-0.014}$
12	$0.9364^{+0.0060}_{-0.0063}$	$0.893^{+0.014}_{-0.015}$
13	$0.9305^{+0.0049}_{-0.0052}$	$0.875^{+0.011}_{-0.012}$
14	$0.926^{+0.014}_{-0.015}$	$0.880^{+0.030}_{-0.034}$
15	$0.9239^{+0.0068}_{-0.0072}$	$0.908^{+0.013}_{-0.014}$
16	$0.9374^{+0.0073}_{-0.0079}$	$0.883^{+0.019}_{-0.021}$
17	$0.9405^{+0.0057}_{-0.0060}$	$0.899^{+0.013}_{-0.013}$

Table 5.18: CMUP and CMX single-muon trigger efficiencies by run period.

Electron ID Scale Factors

Because my electron selection makes fewer requirements than the standard electron selection and is thus less sensitive to mismodeled electron variables, the 1.1 fb^{-1} analysis assumed perfect agreement between data and simulation. Instead, I now measure the electron identification data/simulation scale factors for each period by comparing the efficiencies of each individual ID cut in data and simulation after all other cuts have been applied. Table 5.19 lists the total scale factor for each selection and period.

Period	CEM Trigger	CEM	PEM	Track
0	1.0100 ± 0.0019	1.0083 ± 0.0019	1.0172 ± 0.0025	0.891 ± 0.015
1	1.0063 ± 0.0029	1.0084 ± 0.0026	1.0136 ± 0.0035	0.856 ± 0.022
2	1.0113 ± 0.0026	1.0107 ± 0.0025	1.0144 ± 0.0034	0.864 ± 0.022
3	1.0083 ± 0.0030	1.0077 ± 0.0028	1.0104 ± 0.0039	0.805 ± 0.024
4	1.0069 ± 0.0033	1.0043 ± 0.0033	1.0190 ± 0.0039	0.830 ± 0.025
5	1.0079 ± 0.0027	1.0089 ± 0.0025	1.0138 ± 0.0035	0.863 ± 0.022
6	1.0079 ± 0.0030	1.0069 ± 0.0029	1.0087 ± 0.0039	0.850 ± 0.024
7	1.0145 ± 0.0051	1.0149 ± 0.0044	1.0147 ± 0.0066	0.899 ± 0.047

continued on the next page...

continued from the previous page...

Period	CEM Trigger	CEM	PEM	Track
8	1.0027 ± 0.0026	1.0061 ± 0.0023	1.0112 ± 0.0031	0.846 ± 0.019
9	1.0105 ± 0.0024	1.0079 ± 0.0024	1.0096 ± 0.0033	0.870 ± 0.020
10	1.0054 ± 0.0023	1.0081 ± 0.0021	1.0068 ± 0.0029	0.847 ± 0.017
11	1.0103 ± 0.0022	1.0111 ± 0.0020	1.0099 ± 0.0029	0.857 ± 0.017
12	1.0052 ± 0.0026	1.0087 ± 0.0023	1.0090 ± 0.0033	0.830 ± 0.020
13	1.0066 ± 0.0022	1.0072 ± 0.0020	1.0064 ± 0.0028	0.838 ± 0.016
14	1.0179 ± 0.0036	1.0174 ± 0.0033	1.0182 ± 0.0054	0.826 ± 0.036
15	1.0071 ± 0.0026	1.0069 ± 0.0024	1.0062 ± 0.0034	0.841 ± 0.020
16	1.0079 ± 0.0029	1.0038 ± 0.0029	1.0077 ± 0.0038	0.830 ± 0.023
17	1.0075 ± 0.0025	1.0110 ± 0.0022	0.9980 ± 0.0034	0.845 ± 0.019

Table 5.19: The CEM trigger efficiency and the CEM, PEM, and track electron selection data/simulation scale factors, by period.

Muon ID Scale Factors

I measure muon identification data/simulation scale factors for each period in the same way as my electron scale factors. Table 5.20 lists the total scale factor for each muon selection. The trigger muon selection scale factors include

a stub reconstruction scale factor which is the dominant effect. In the later data, a drop in the d_0 cut efficiency at high luminosity drives the basic muon ID scale factor down.

Period	CMUP Trigger	CMX Trigger	Muon SF
0	0.9709 ± 0.0045	1.0372 ± 0.0051	1.0043 ± 0.0021
1	0.9591 ± 0.0079	1.0163 ± 0.0081	0.9968 ± 0.0034
2	0.9740 ± 0.0067	1.0151 ± 0.0076	1.0015 ± 0.0031
3	0.9640 ± 0.0092	1.0260 ± 0.0090	1.0016 ± 0.0040
4	0.9634 ± 0.0091	1.0195 ± 0.0093	1.0007 ± 0.0039
5	0.9606 ± 0.0070	1.0158 ± 0.0072	0.9903 ± 0.0032
6	0.9579 ± 0.0078	1.0214 ± 0.0079	0.9856 ± 0.0036
7	0.961 ± 0.014	1.015 ± 0.014	0.9981 ± 0.0060
8	0.9676 ± 0.0057	1.0111 ± 0.0066	0.9837 ± 0.0029
9	0.9665 ± 0.0060	1.0061 ± 0.0069	0.9803 ± 0.0030
10	0.9579 ± 0.0052	1.0118 ± 0.0058	0.9766 ± 0.0026
11	0.9472 ± 0.0057	0.9988 ± 0.0064	0.9678 ± 0.0029
12	0.9532 ± 0.0065	1.0054 ± 0.0073	0.9795 ± 0.0032

continued on the next page...

continued from the previous page...

Period	CMUP Trigger	CMX Trigger	Muon SF
13	0.9551 ± 0.0051	1.0027 ± 0.0061	0.9891 ± 0.0025
14	0.962 ± 0.014	1.027 ± 0.014	0.9914 ± 0.0062
15	0.9471 ± 0.0066	1.0081 ± 0.0070	0.9769 ± 0.0031
16	0.9383 ± 0.0086	0.9943 ± 0.0100	0.9667 ± 0.0042
17	0.9341 ± 0.0065	0.9946 ± 0.0072	0.9625 ± 0.0032

Table 5.20: The CMUP trigger and CMX trigger efficiencies and the data/simulation scale factor for the basic muon selection, by period.

Forward Tracking Efficiency Scale Factor

The simulation does not accurately reproduce COT superlayer occupancies, so I expect different efficiencies for backward tracking in the data and in the simulation. I study the difference by reconstructing trigger + forward ($|\eta_{trk}| > 1$) pairs of muons and comparing the dimuon yield for bins of the forward leg track η. Figure 5.15 shows that the difference between the newly-reconstructed data and the new simulation is small. When convolved with either the single Z or the graviton signal acceptances, the effect is negligible compared to other uncertainties. Thus, I ignore this scale factor.

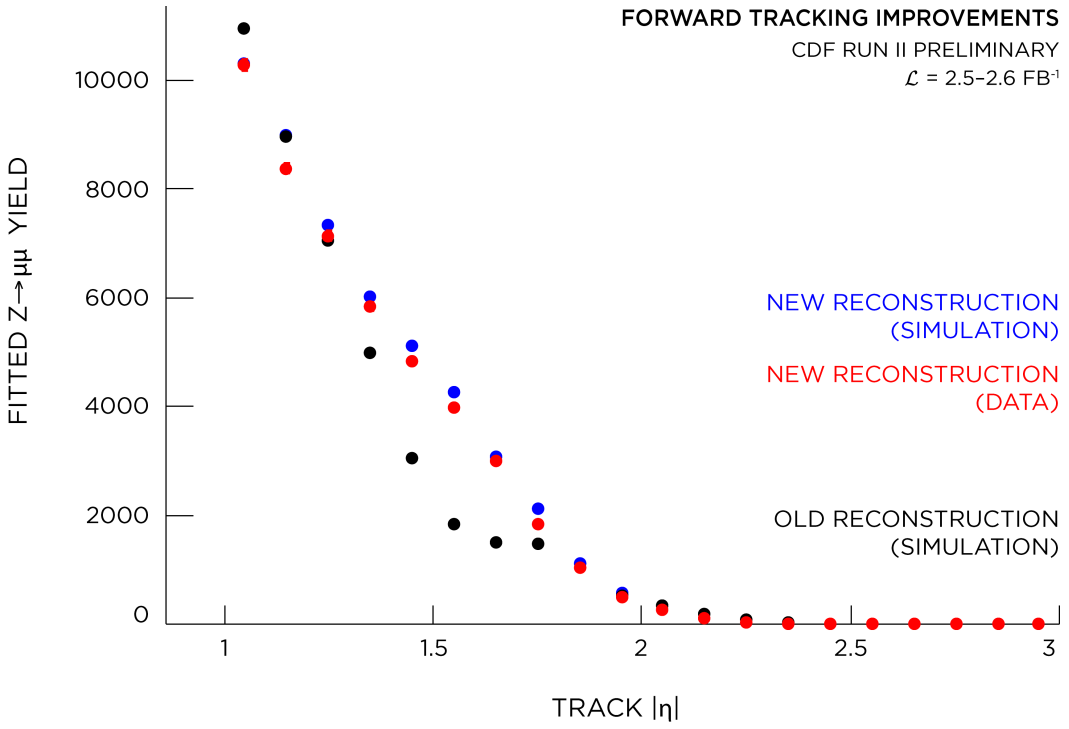

Figure 5.15: Dimuon yield per 0.1 $|\eta|$ bin vs forward track η for (black) the older 6.1 simulation (blue) "reprocessed" 7.1 simulation and (red) reprocessed 7.1 data.

z Vertex Scale Factor

Table 5.21 lists the efficiency $\epsilon^{\rm data}_{\rm ZVERTEX}$ of this cut for each period of data, evaluated using a very pure sample of Z events selected with the CDF standard muon criteria in a 5 GeV window around the Z pole mass. Table 5.22 shows the scale factor $\epsilon^{\rm data}_{\rm ZVERTEX}/\epsilon^{\rm mc}_{\rm ZVERTEX}$ comparing the data to Z simulation for each period.

Sample	Period	Efficiency	Sample	Period	Efficiency
BHEL	0	0.96643(23)	BHMU	0	0.96496(36)
BHEL	1	0.999477(55)	BHMU	1	0.99340(29)
BHEL	2	0.999461(56)	BHMU	2	0.99360(27)
BHEL	3	0.999511(63)	BHMU	3	0.99354(31)
BHEL	4	0.999563(63)	BHMU	4	0.99311(33)
BHEL	5	0.999513(53)	BHMU	5	0.99410(25)
BHEL	6	0.999583(58)	BHMU	6	0.99464(27)
BHEL	7	0.99946(11)	BHMU	7	0.99305(48)
BHEL	8	0.999363(49)	BHMU	8	0.99345(20)
BHEL	9	0.999442(50)	BHMU	9	0.99318(21)

continued on the next page...

continued from the previous page...

Sample	Period	Efficiency	Sample	Period	Efficiency
BHEL	10	0.999380(43)	BHMU	10	0.99259(17)
BHEL	11	0.999358(46)	BHMU	11	0.99264(16)
BHEL	12	0.999525(48)	BHMU	12	0.99382(19)
BHEL	13	0.999447(38)	BHMU	13	0.99543(14)
BHEL	14	0.999421(92)	BHMU	14	0.99542(28)
BHEL	15	0.999504(49)	BHMU	15	0.99349(11)
BHEL	16	0.999288(68)	BHMU	16	0.99325(12)
BHEL	17	0.999432(50)	BHMU	17	0.99307(98)
BHEL	average	0.994280(38)	BHMU	average	0.991473(48)

Table 5.21: Efficiency for $|z| < 60$cm by data period.

Sample	Period	Efficiency	Sample	Period	Efficiency
BHEL	0	1.00432(59)	BHMU	0	1.00346(66)
BHEL	1	1.03867(56)	BHMU	1	1.03304(63)
BHEL	2	1.03865(56)	BHMU	2	1.03325(63)
BHEL	3	1.03870(57)	BHMU	3	1.03318(65)
BHEL	4	1.03876(57)	BHMU	4	1.03274(66)
BHEL	5	1.03870(56)	BHMU	5	1.03377(62)
BHEL	6	1.03878(56)	BHMU	6	1.03433(63)
BHEL	7	1.03865(57)	BHMU	7	1.03267(75)
BHEL	8	1.03855(56)	BHMU	8	1.03309(60)
BHEL	9	1.03863(56)	BHMU	9	1.03281(60)
BHEL	10	1.03857(56)	BHMU	10	1.03220(59)
BHEL	11	1.03854(56)	BHMU	11	1.03225(58)
BHEL	12	1.03872(75)	BHMU	12	1.03347(59)
BHEL	13	1.03863(56)	BHMU	13	1.03515(58)
BHEL	14	1.03861(57)	BHMU	14	1.03514(63)
BHEL	15	1.03869(56)	BHMU	15	1.03313(57)

continued on the next page...

continued from the previous page...

Sample	Period	Efficiency	Sample	Period	Efficiency
BHEL	16	1.03847(57)	BHMU	16	1.03288(57)
BHEL	17	1.03862(56)	BHMU	17	1.0327(12)
BHEL	combined	1.03327(56)	BHMU	combined	1.03103(56)

Table 5.22: Scale factor $\epsilon^{\text{data}}_{\text{ZVERTEX}}/\epsilon^{\text{mc}}_{\text{ZVERTEX}}$ for $|z| < 60$cm by data period. Section 5.2.3 describes simulation of the $Z \to ee$ and $Z \to \mu\mu$ events used here. The differences between electrons and muons are small. Except for Period 0, the run dependence is negligible.

Δz_0 Scale Factor

I measure a period-dependent Δz_0 scale factor using 66–116 GeV dimuon events where all other cuts have been applied. Table 5.23 lists the measurement. This cut efficiency drops faster with luminosity than the d_0 muon ID cut.

Period	Scale Factor
0	0.9890 ± 0.0014

continued on the next page...

continued from the previous page...

Period	Scale Factor
1	0.9642 ± 0.0027
2	0.9615 ± 0.0025
3	0.9601 ± 0.0028
4	0.9559 ± 0.0033
5	0.9453 ± 0.0026
6	0.9471 ± 0.0028
7	0.9472 ± 0.0050
8	0.9361 ± 0.0023
9	0.9212 ± 0.0025
10	0.9098 ± 0.0021
11	0.9019 ± 0.0021
12	0.9027 ± 0.0026
13	0.9368 ± 0.0019
14	0.9335 ± 0.0051
15	0.9081 ± 0.0025
16	0.8955 ± 0.0031
17	0.8882 ± 0.0025

continued on the next page...

continued from the previous page...

Period	Scale Factor

Table 5.23: Scale factors for Δz_0 cut, by period.

Dielectron Cross Section

Figure 5.16 shows the dielectron cross section for individual selections and the combination of all selections as a function of run period. The final result, 249.4 ± 1.6 pb, is evidence that the constituent period-dependent efficiencies and scale factors are understood well within the overall 20% two Z acceptance systematic I assign to the combination of all periods.

Note that the PEM cross section is slightly low and that there are large variations in the trigger+track cross section. In these cases, the significant background causes the signal component of the signal+background fit to count a fraction of signal as background that varies differently in the simulation than in the data. In the track lepton case, the fit to the combination of a "Crystal Ball" radiative tail and the exponential background PDF is somewhat unstable without any other constraints. The independent fit to the combination of all selections does not have these problems.

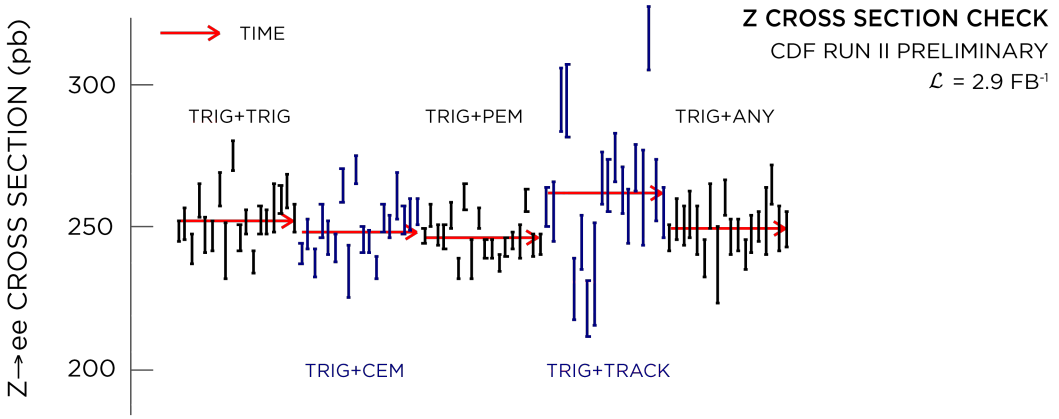

Figure 5.16: $Z \rightarrow ee$ cross sections (and averaged cross sections) for various selections. The horizontal axis indicates time, segmented into 18 CDF standard periods for five selections in succession: two CEM trigger electrons (252.1 ± 1.2 pb), a CEM trigger electron and another CEM electron (248.4 ± 1.1 pb), a CEM trigger electron and a PEM electron (246.2 ± 0.87 pb), a CEM trigger electron and a track electron (262.1 ± 2.3 pb), and, calculated separately, the combination of a CEM trigger electron and any other electron (249.4 ± 1.6 pb). Errors are statistical only with the correlated luminosity uncertainty not shown.

Dimuon Cross Section

Figure 5.17 shows the dimuon cross section for individual selections and the combination of all selections for each trigger path. The Period 0 CMX simulation acceptance includes contributions from the keystone and miniskirt regions which are not present in the early data, requiring a rescaling of that acceptance by approximately 80%. The average cross section for all combinations of CMUP trigger muons and another muon, and all CMX trigger muons and another muon, is 254.3 ± 1.0 pb. I conclude that my muon selection is sufficiently understood, and the overall 20% two Z acceptance systematic more than covers the trend toward higher cross section in the later CMX-triggered data.

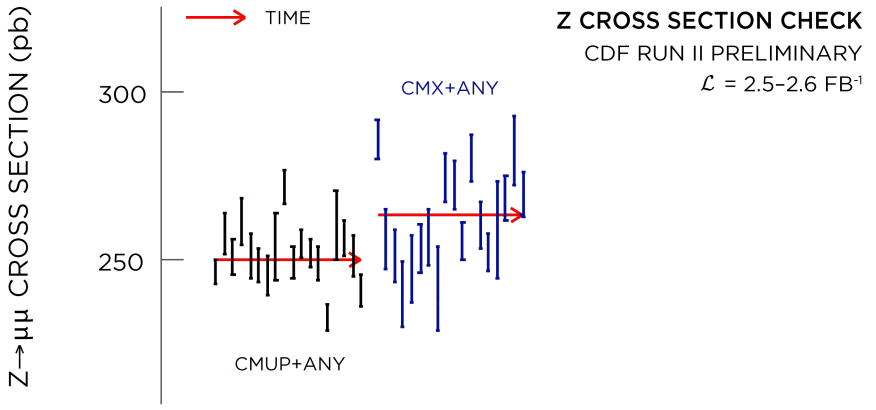

Figure 5.17: The horizontal axis indicates time for two selections in succession: a CMUP trigger muon and another muon (250.0 ± 1.2 pb) and a CMX trigger muon and another muon which did not fire the CMUP trigger (263.4 ± 1.8 pb). The vertical axis is the $Z \rightarrow \mu\mu$ cross section in pb. Errors are statistical only with the correlated luminosity uncertainty not shown. The average cross section of the trigger + inclusive muon selections is 254.3 ± 1.0pb.

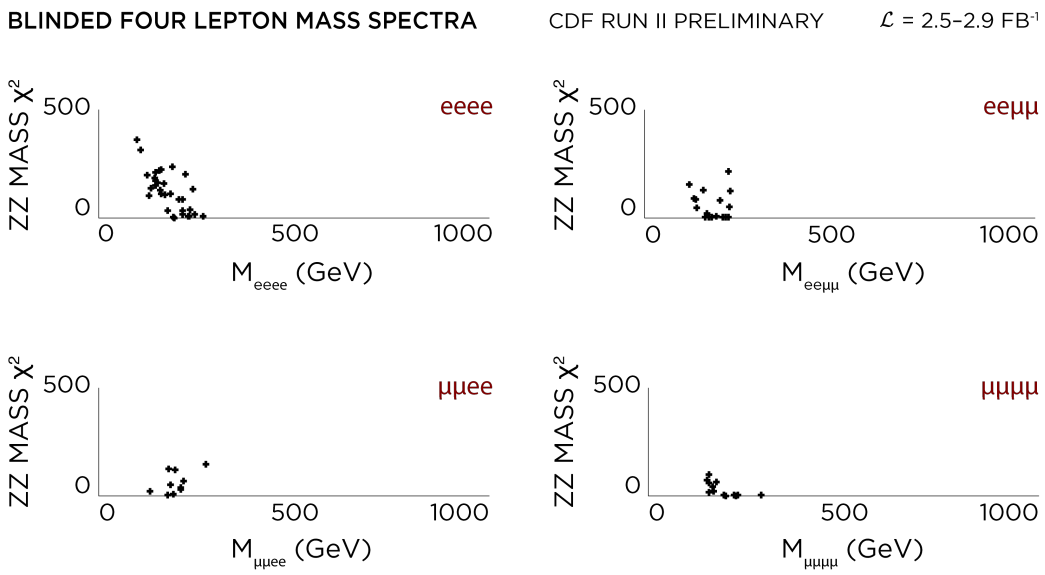

Figure 5.18: χ^2_{ZZ} vs M_X (GeV) for the $X \rightarrow ZZ \rightarrow eeee$ control region.

5.6.3 Examination of low M_X control regions

Figure 5.18 shows the χ^2_{ZZ} vs M_X distributions for $eeee$, $ee\mu\mu$, $\mu\mu ee$, and $\mu\mu\mu\mu$ channels. The data above $M_X = 300$ GeV are hidden. Above the $\approx$ 185 GeV ZZ production threshold, the low χ^2_{ZZ} region contains a noticeable population. These events are discussed in more detail in Section 5.9.1.

5.7 Background estimation

The dominant backgrounds at high M_X for both the four lepton and two lepton + two jets channels are a mixture of Z + jets, $W^{\pm}$ + jets, QCD, and various lower-rate processes resulting in one or more hadrons faking an electron or muon. Only $W^{\pm}Z \to jjll$, $ZZ \to llll$, and $ZZ \to lljj$ processes peak at $\chi^2_{ZZ} < 50$ or $65 < M_{qq} < 120$ GeV; these are so small that they have only been recently observed at the Tevatron. I use simulation to model these resonant processes and I fit the aggregate sideband data to collectively estimate all non-resonant backgrounds.

5.7.1 Four-lepton non-resonant background estimate

The sideband data I fit for the four-lepton background estimates are the $M_X < 300$ GeV four-lepton sample and three kinematically similar but orthogonal samples enriched in fakes. As the background composition and fake rate kinematic dependence varies with trigger dataset and lepton type, I fit for the $eeee$, $ee\mu\mu$, $\mu\mu ee$[1], and $\mu\mu\mu\mu$ backgrounds separately.

The procedure is as follows:

[1]The order denotes the trigger required.

1. Construct the three fake-enriched samples by building X combinations from a trigger lepton plus one, two, or three anti-selected leptons where the principal identification cuts are inverted and the remaining leptons are selected as normal. Tables 5.24, 5.25, 5.26, and 5.27 list requirements made of the anti-selected lepton candidates. Figure 5.19a shows the trigger electron + anti-selected electron single Z distribution and Figure 5.19b shows the trigger muon + anti-selected muon single Z distribution. Neither distribution indicates a large fraction of events peaking at the Z mass, implying both anti-selected lepton categories are depleted of real lepton signal.

2. Observe that the two-dimensional spectrum of χ^2_{ZZ} vs M_X above the ZZ kinematic threshold ($M_X = 185$ GeV) has the same shape amongst the three fake-enriched samples and the $M_X < 300$ GeV control portion of the four-lepton sample. Figures 5.21 and 5.22 display the χ^2_{ZZ} vs M_X distributions of these n-fake sideband samples.

3. Fit for this shape in the two- and three-fake samples, where any contamination from potential signal has a negligible effect on the shape. For each trigger dataset and combination of lepton types, I perform a simultaneous unbinned maximum-likelihood fit of the $185 < M_X < 300$ GeV and

$\chi^2_{ZZ} < 500$ data to the empirical form

$$f(\chi^2_{ZZ}, M_X) = m^{\gamma}_{llll} \cdot e^{\tau\chi^2_{ZZ}}$$

to determine the falling shape of the M_X distribution (the power law parameter γ) and the relationship of the number of events in the $\chi^2_{ZZ} < 50$ ZZ window to the off-mass sidebands (the exponential decay parameter τ).

4. Normalize the fitted shape to the number of events in the same region in four-lepton data minus the yield predicted by the ZZ simulation for this region.

5. Integrate the normalized PDF in the $M_X > 300$ GeV, $\chi^2_{ZZ} < 50$ four-lepton signal region.

Anti-selected CEM Electron Selection
CEM Cluster Only
Matching PAD Track
Fiducial = 1
$E_T^{cal} > 5$ GeV
$\lvert z_0^{trk} \rvert < 60$ cm
$E_{HAD}/E_{EM} > 0.055\,\text{GeV} + 0.00045 * E^{cal}$

Table 5.24: Anti-selected CEM electron selection. The HAD/EM cut is inverted and there is no isolation cut, but otherwise the selection is identical to Table 5.8.

Anti-selected PEM Electron Selection
PEM Cluster Only
$\lvert \eta_{det} \rvert < 2.5$
$E_T^{cal} > 5$ GeV
$E_{HAD}/E_{EM} > 0.05$ GeV

Table 5.25: Anti-selected PEM electron selection. The HAD/EM cut is inverted and there is no isolation cut, but otherwise the selection is identical to Table 5.9.

Anti-selected Track Electron Selection
PAD Track Only
Track is Not Fiducial in the CES
$\Delta r_{\eta\phi} > 0.2$ with all other electrons from Section 5.4.1
$p_T \geq 10\,\text{GeV}$
$\lvert z_0 \rvert < 60.\,\text{cm}$
Axial COT Segments ≥ 3
Stereo COT Segments ≥ 2
$\lvert d_0 \rvert < \begin{cases} 200\,\mu m & \text{if } N_{si} > 0 \\ 2\,mm & \text{if } N_{si} = 0 \end{cases}$
$TrkIsol < 0.9$

Table 5.26: Anti-selected track electron selection. The track isolation cut is inverted to ensure the anti-selected candidates are disjoint from the normal track electrons, but otherwise the selection is identical to Table 5.10.

Anti-selected Muon Selection

PAD Track Only

$p_T^{trk} > 2(10)$ GeV with(without) stub

$\kappa/\sigma_\kappa > 2.5$

$p(\chi^2, ndof) > 10^{-10}$

$|z_0^{trk}| < 60$ cm

$$|d_0| < \begin{cases} 200\,\mu m & \text{if } N_{si} > 0 \\ 2\,mm & \text{if } N_{si} = 0 \end{cases}$$

$E_{EM} > 6 + max(0, 0.0115 * (\frac{p^{trk}}{\text{GeV}} - 100))$ GeV

$E_{HAD} > 18 + max(0, 0.028 * (\frac{p^{trk}}{\text{GeV}} - 100))$ GeV

Table 5.27: Anti-selected muon selection. The isolation cut is absent and the minimum-ionizing cuts are inverted with cut values 50% larger than the otherwise identical selection in Table 5.12.

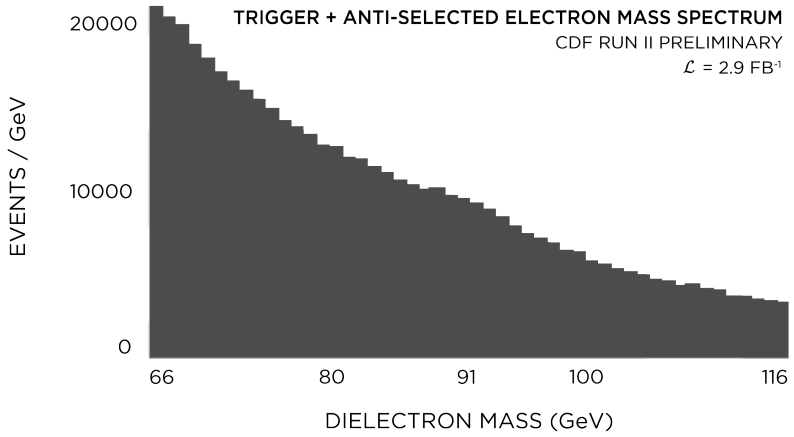

(a)

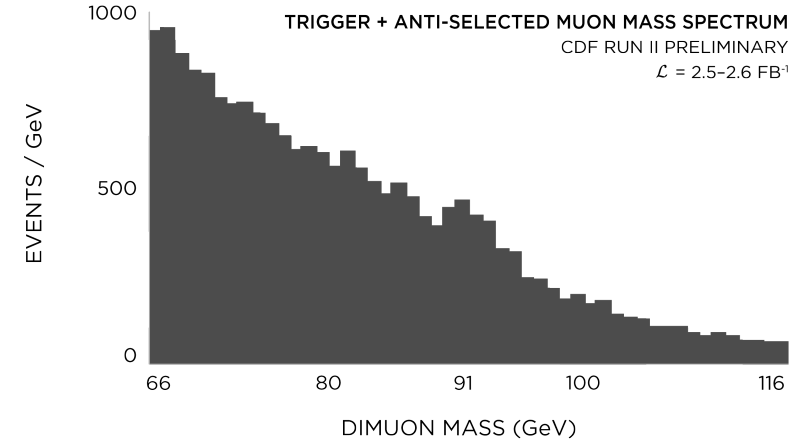

(b)

Figure 5.19: Dilepton mass distributions for (a) trigger electron + anti-selected electron selection and (b) trigger muon + anti-selected muon selection, Periods 0–17.

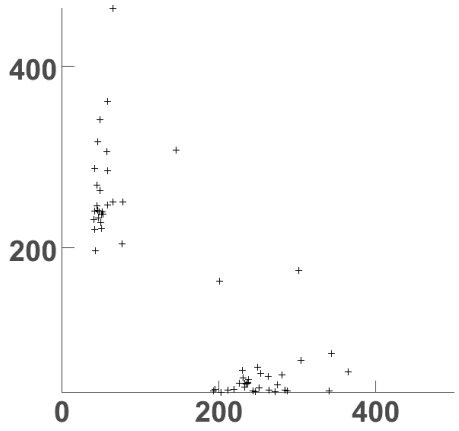

Figure 5.20: M_{Z_1} vs M_{Z_2} (randomized ordering) for $X \to ZZ \to ee\mu\mu$ 3-fake lepton events with $M_X > 200$ GeV and $\chi^2_{ZZ} > 1000$.

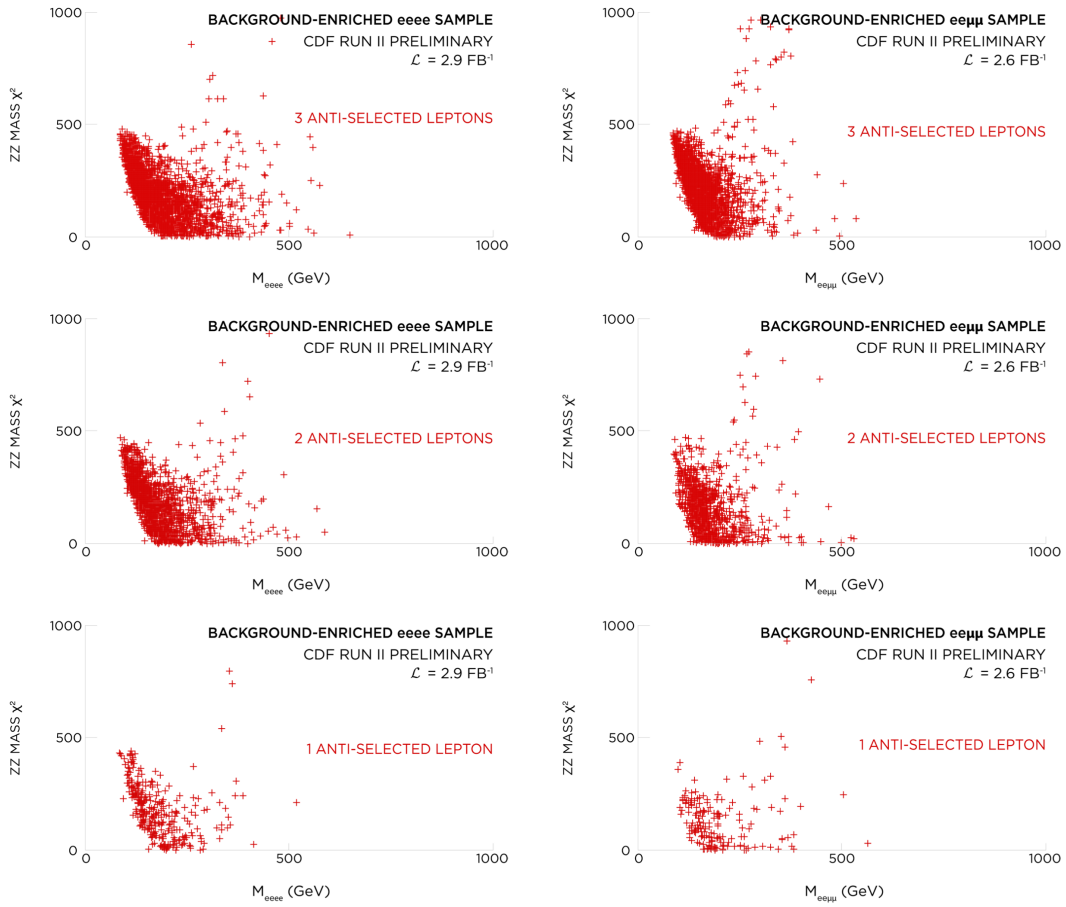

Figure 5.21: χ^2_{ZZ} vs M_X distributions for electron-triggered (left) $X \rightarrow ZZ \rightarrow eeee$ and (right) $X \rightarrow ZZ \rightarrow ee\mu\mu$ selections with three, two, and one anti-selected leptons.

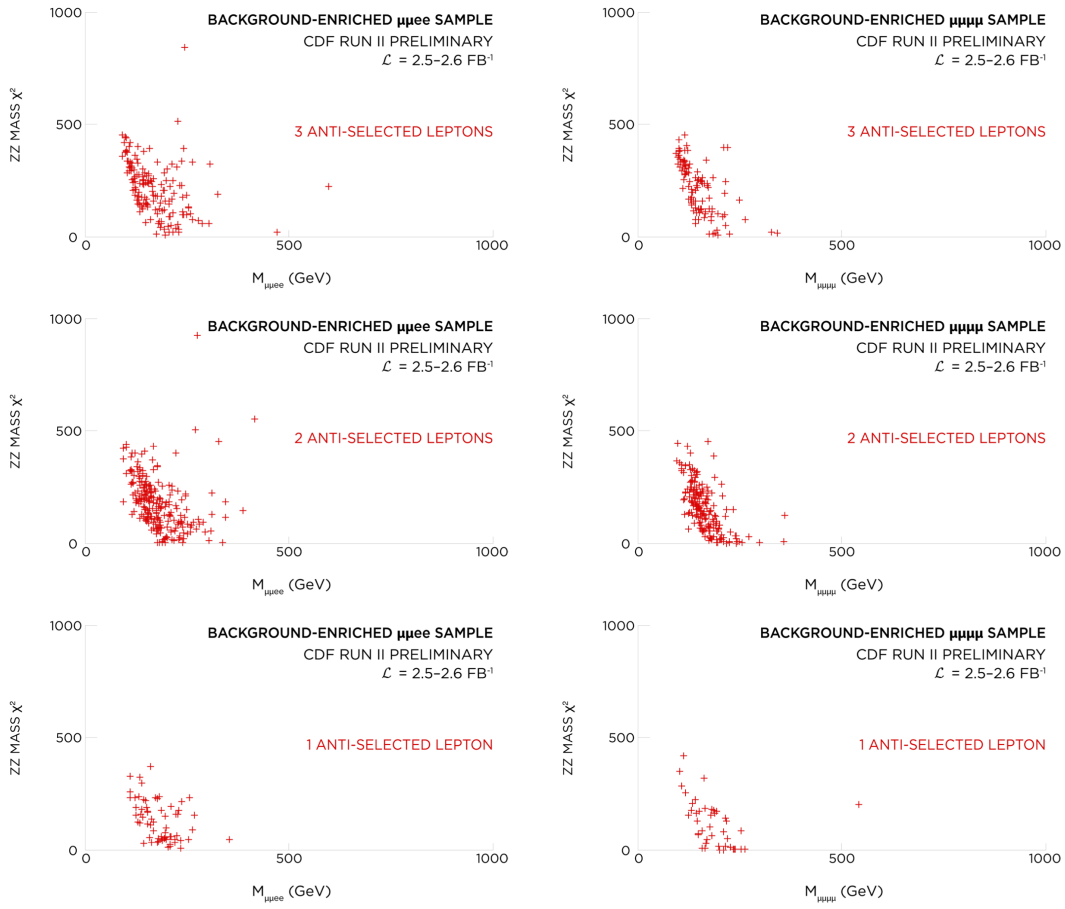

Figure 5.22: χ^2_{ZZ} vs M_X distributions for muon-triggered (left) $X \to ZZ \to \mu\mu ee$ and (right) $X \to ZZ \to \mu\mu\mu\mu$ selections with three, two, and one anti-selected leptons.

γ	-4.390(88)
τ	-0.01839(46)

Table 5.28: *eeee* non-resonant background fit parameters.

Signal Mass (GeV)	Prediction
400	1.31(31)(31)
500	0.64(15)(25)
600	0.44(10)(15)
700	0.28(07)(19)
800	0.15(04)(11)
900	0.14(03)(11)
1000	0.11(03)(10)

Table 5.29: *eeee* non-resonant background estimates.

γ	-5.42(15)
τ	-0.01605(54)

Table 5.30: $ee\mu\mu$ non-resonant background fit parameters.

Signal Mass (GeV)	Prediction
400	0.33(11)(07)
500	0.128(44)(47)
600	0.075(26)(39)
700	0.041(14)(25)
800	0.019(06)(12)
900	0.016(06)(12)
1000	0.012(04)(10)

Table 5.31: $ee\mu\mu$ non-resonant background estimates.

γ	-5.25(34)
τ	-0.0202(16)

Table 5.32: $\mu\mu ee$ non-resonant background fit parameters.

Signal Mass (GeV)	Prediction
400	0.323(13)(09)
500	0.130(50)(58)
600	0.078(30)(46)
700	0.044(17)(30)
800	0.021(08)(15)
900	0.018(07)(15)
1000	0.014(05)(12)

Table 5.33: $\mu\mu ee$ non-resonant background estimates.

γ	-6.51 $\pm$ 0.61
τ	-0.0299 $\pm$ 0.0032

Table 5.34: $\mu\mu\mu\mu$ non-resonant background fit parameters.

Signal Mass (GeV)	Prediction
400	0.207(78)(74)
500	0.063(24)(32)
600	0.031(12)(20)
700	0.015(06)(11)
800	0.0056(21)(44)
900	0.0046(17)(38)
1000	0.0031(12)(27)

Table 5.35: $\mu\mu\mu\mu$ non-resonant background estimates.

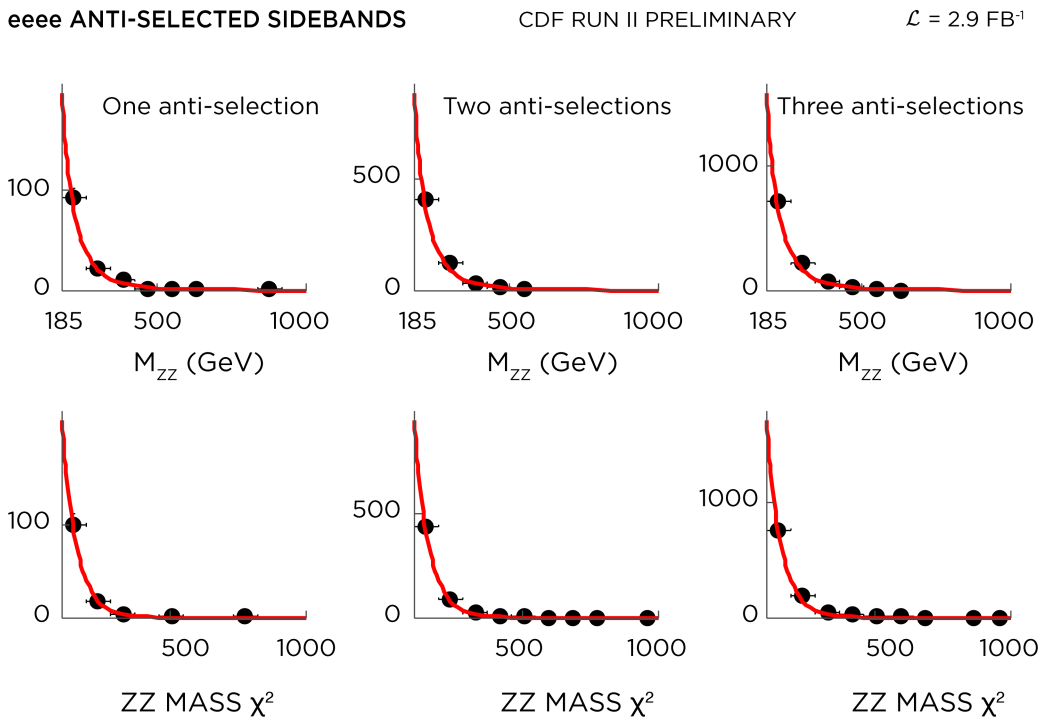

Figure 5.23: Simultaneous fit to two and three anti-selected electron $X \rightarrow ZZ \rightarrow$ *eeee* sideband samples and one-dimensional projections to fitted and unfitted M_X and χ^2_{ZZ} data. From left to right: one, two, and three anti-selected electrons.

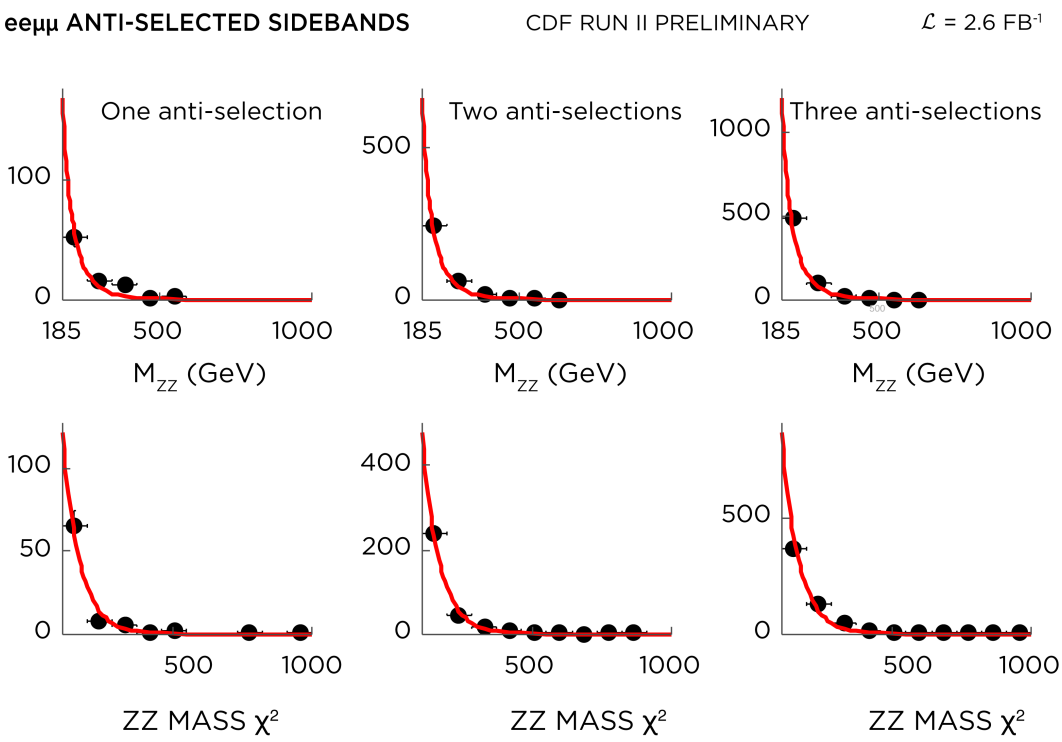

Figure 5.24: Simultaneous fit to two and three anti-selected lepton $X \to ZZ \to ee\mu\mu$ sideband samples and one-dimensional projections to fitted and unfitted M_X and χ^2_{ZZ} data. From left to right: one, two, and three anti-selected leptons.

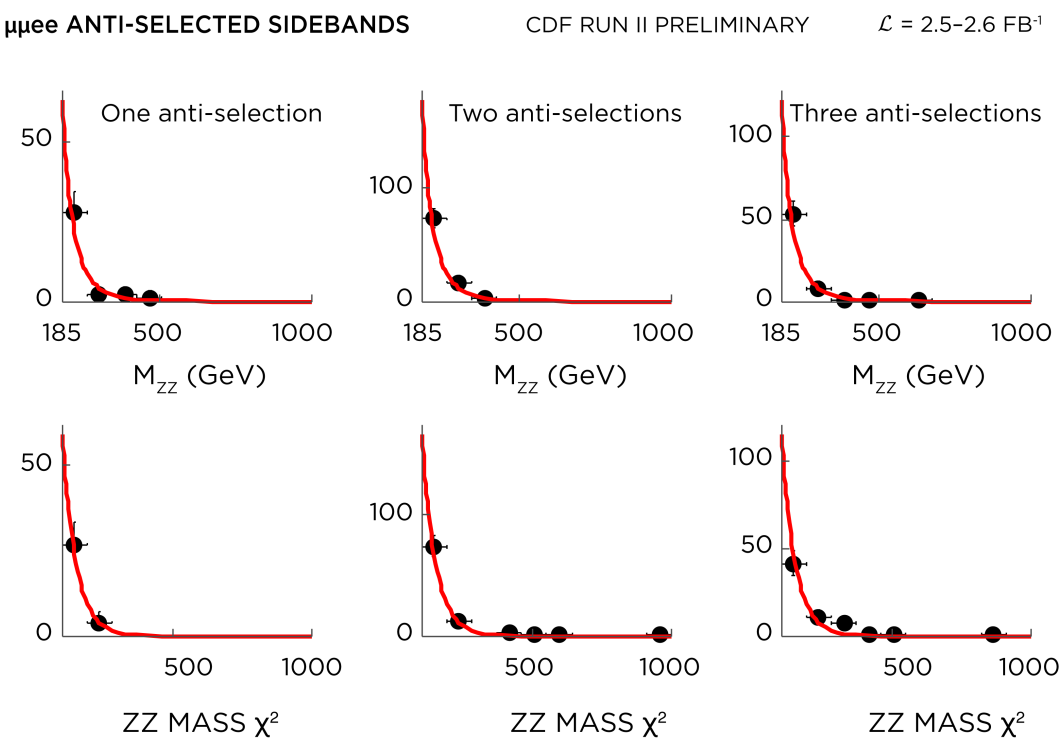

Figure 5.25: Simultaneous fit to two and three anti-selected lepton $X \to ZZ \to \mu\mu ee$ sideband samples and one-dimensional projections to fitted and unfitted M_X and χ^2_{ZZ} data. From left to right: one, two, and three anti-selected leptons.

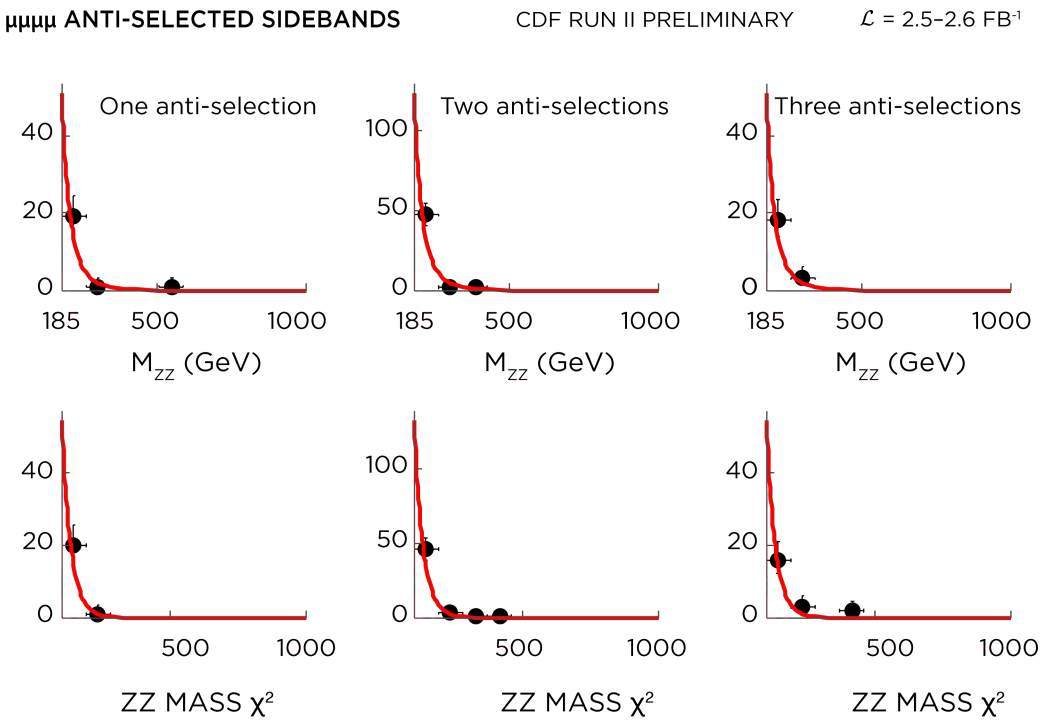

Figure 5.26: Simultaneous fit to two and three anti-selected muon $X \rightarrow ZZ \rightarrow \mu\mu\mu\mu$ sideband samples and one-dimensional projections to fitted and unfitted M_X and χ^2_{ZZ} data. From left to right: one, two, and three anti-selected muons.

5.7.2 Four-lepton background cross checks

Mass shape independence

As a check that the fitted background shape is independent of anti-lepton multiplicity, I free the power law mass parameter γ to float independently for each sample and refit to obtain the results in Table 5.36. In all but the $ee\mu\mu$ single anti-lepton case, the independent γ is statistically compatible with the simultaneous fit to the 3 and 2 anti-lepton samples, and I conclude the shape is sufficiently independent.

One can see the reason for the $ee\mu\mu$ 1 anti-lepton discrepancy in the top-left plot of Figure 5.24, where the third bin contains more events than predicted by the simultaneous fit. However, the $\mu\mu ee$ and $\mu\mu\mu\mu$ shapes in the low anti-lepton multiplicity samples are consistent with the simultaneous fit, the 0 anti-leptons $ee\mu\mu$ sample has a statistically compatible shape, and the effect of a shallower power law shape would be a higher background prediction and thus a stronger limit. I choose to retain the simple model and the conservative limit rather than to adjust the background procedure. It should also be noted that the 1 anti-lepton sample is excluded from the fit specifically because simulation studies show signal decaying into the dijet channels may make a non-negligible contribution.

Channel	$eeee$	$ee\mu\mu$	$\mu\mu ee$	$\mu\mu\mu\mu$
Simultaneous (3,2)	-4.390(88)	-5.42(15)	-5.25(34)	-6.51(61)
3 anti-leptons	-4.22(11)	-5.19(17)	-4.98(50)	-6.3(11)
2 anti-leptons	-4.50(15)	-4.70(21)	-4.96(41)	-6.60(73)
1 anti-lepton	-4.21(30)	-3.63(32)	-5.25(73)	-5.33(92)
0 anti-leptons	-5.04(94)	-3.54(78)	-5.7(16)	-4.4(13)

Table 5.36: Comparison of non-resonant background mass shape parameter γ for individual sideband samples with the simultaneous fit.

Isolation bias

At very high M_X, the two leptons from the Z decay are more likely to be boosted toward small opening angle. Though the muon calorimeter isolation should remain small, the electron isolation cut will lose efficiency. I apply this isolation cut for real electrons but remove it for anti-selected electrons to increase the fake sample size. This could lead to overestimation of the non-resonant backgrounds. To check this, I repeat the non-resonant background fits for the subset of the sideband data which passes the cut. The results are statistically compatible with the inclusive results, so I conclude that any overestimation is negligible.

	Isolated Fits	Inclusive Fits
γ	-4.32(25)	-4.390(88)
τ	-0.0186(13)	-0.01839(46)
N(350–450 GeV)	0.93(14)	0.882(47)
N(800–1200 GeV)	0.078(68)	0.070(57)

Table 5.37: Comparison of *eeee* non-resonant background fit parameters and predictions for anti-electrons with and without the isolation cut, uncorrelated uncertainties only.

	Isolated Fits	Inclusive Fits
γ	-5.38(20)	-5.42(15)
τ	-0.0181(8)	-0.01605(54)
N(350–450 GeV)	0.238(30)	0.216(20)
N(800–1200 GeV)	0.0079(64)	0.0070(54)

Table 5.38: Comparison of $ee\mu\mu$ non-resonant background fit parameters and predictions for anti-electrons with and without the isolation cut, uncorrelated uncertainties only.

	Isolated Fits	Inclusive Fits
γ	-5.88(69)	-5.25(34)
τ	-0.0175(26)	-0.0202(16)
N(350–450 GeV)	0.135(68)	0.213(48)
N(800–1200 GeV)	0.0029(27)	0.0079(68)

Table 5.39: Comparison of $\mu\mu ee$ non-resonant background fit parameters and predictions for anti-electrons with and without the isolation cut, uncorrelated uncertainties only.

5.7.3 Dijet non-resonant background estimate

The $X \to ZZ \to lljj$ background estimate for all non-resonant backgrounds starts with events containing a dilepton pair with pull($Z \to ll$) $< 5\,\sigma$ (see Section 5.6) and a dijet pair in either $40 < M_{qq} < 65$ GeV or $120 < M_{qq} < 200$ GeV sidebands.

To understand the method, consider Figure 5.27, a cartoon illustrating the kinematics of the dielectron + dijet sideband samples. With no M_X cut, Z-like events dominate and the dijet mass distribution is a familiar falling exponential. An $M_X > M_X^{\min}$ cut introduces a kinematic turn-on at $M_{qq} \approx M_X^{\min} - M_Z$. At high values of $M_X^{\min}$, the M_{qq} spectrum in the Z window and both sidebands is linear, with the artificial peak formed by the turn-on appearing above the relevant dijet mass range. One can then simply linearly interpolate between the two sidebands to estimate the background in the signal window $65 < M_{qq} < 120$ GeV when $M_X > 300$ GeV.

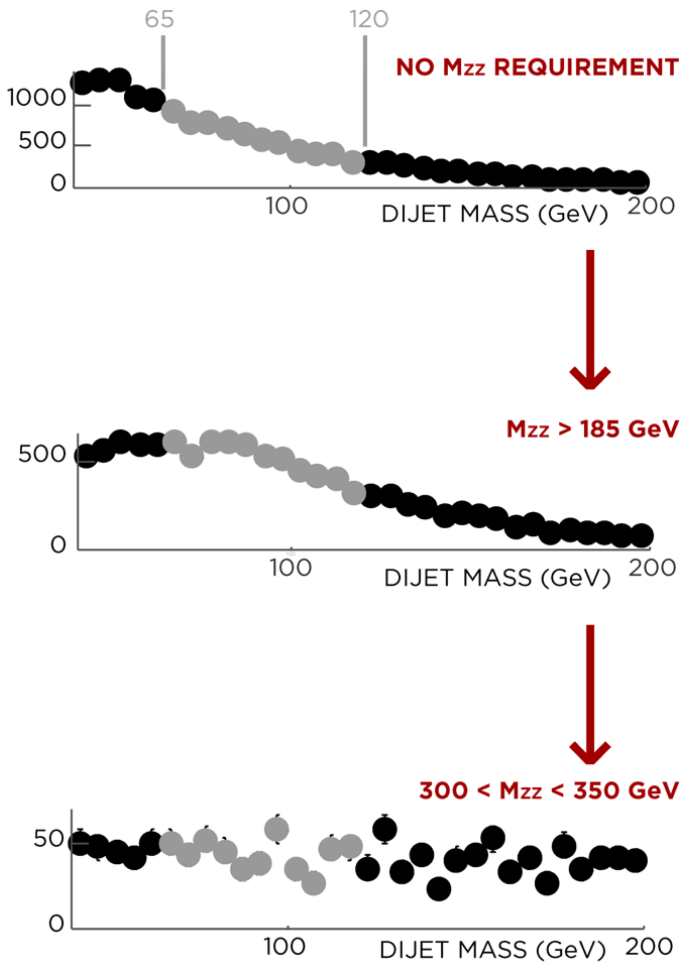

Figure 5.27: $X \to ZZ \to eejj$ sideband data as successively higher M_X requirements are imposed.

At sufficiently high $M_X^{\min}$, both sidebands will be empty and the interpolation will underpredict the background. However, as Figures 5.30 and 5.31 show, the number of events in each sideband decreases with $M_X^{\min}$ in a predictable way. Therefore I fit each sideband distribution to an exponential function of $M_X^{\min}$ for $M_X < 500$GeV and interpolate between the fit predictions (instead of the observed event counts) to determine the background.

The remaining resonant backgrounds, $W^{\pm}Z \to jjll$ and $ZZ \to lljj$, are small at large M_X and evaluated with simulation.

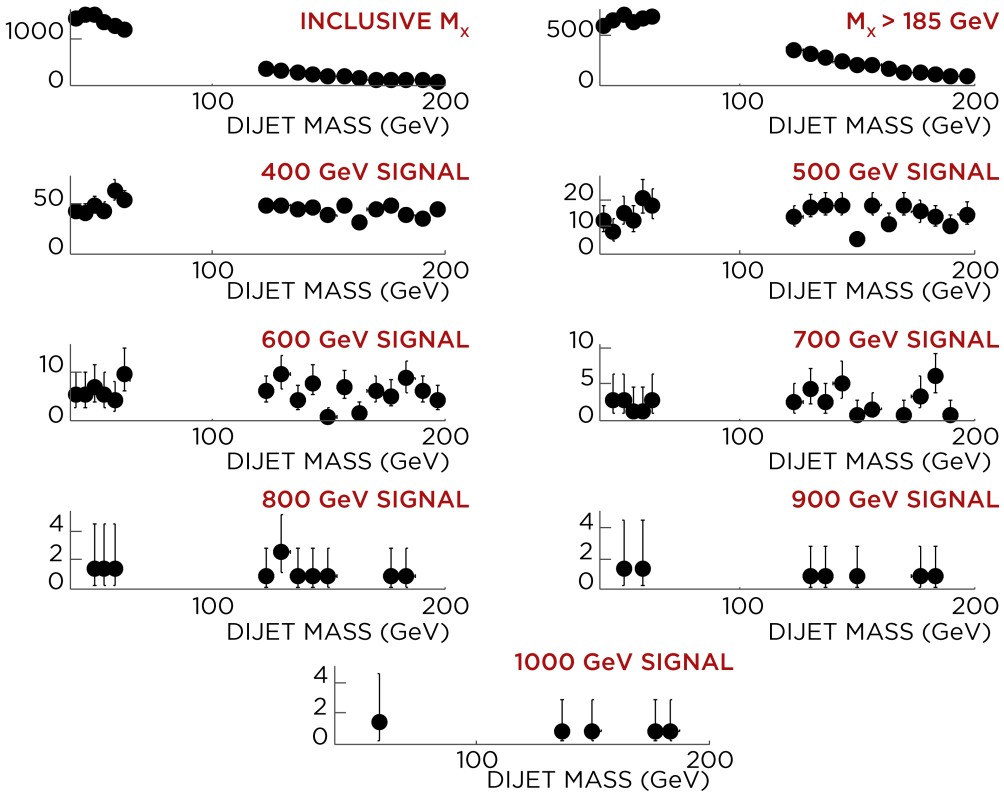

Figure 5.28: $X \rightarrow ZZ \rightarrow eejj$ sidebands for two large subsets of the data and each M_X range used to set graviton limits.

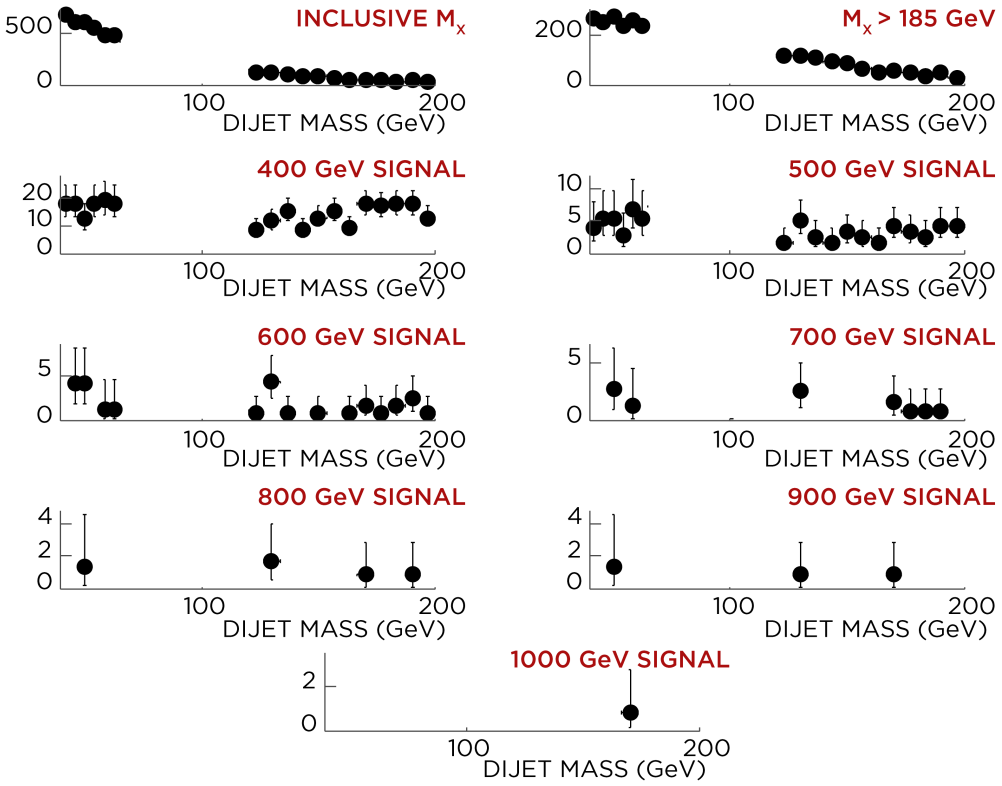

Figure 5.29: $X \to ZZ \to \mu\mu jj$ sidebands for two large subsets of the data and each M_X range used to set graviton limits.

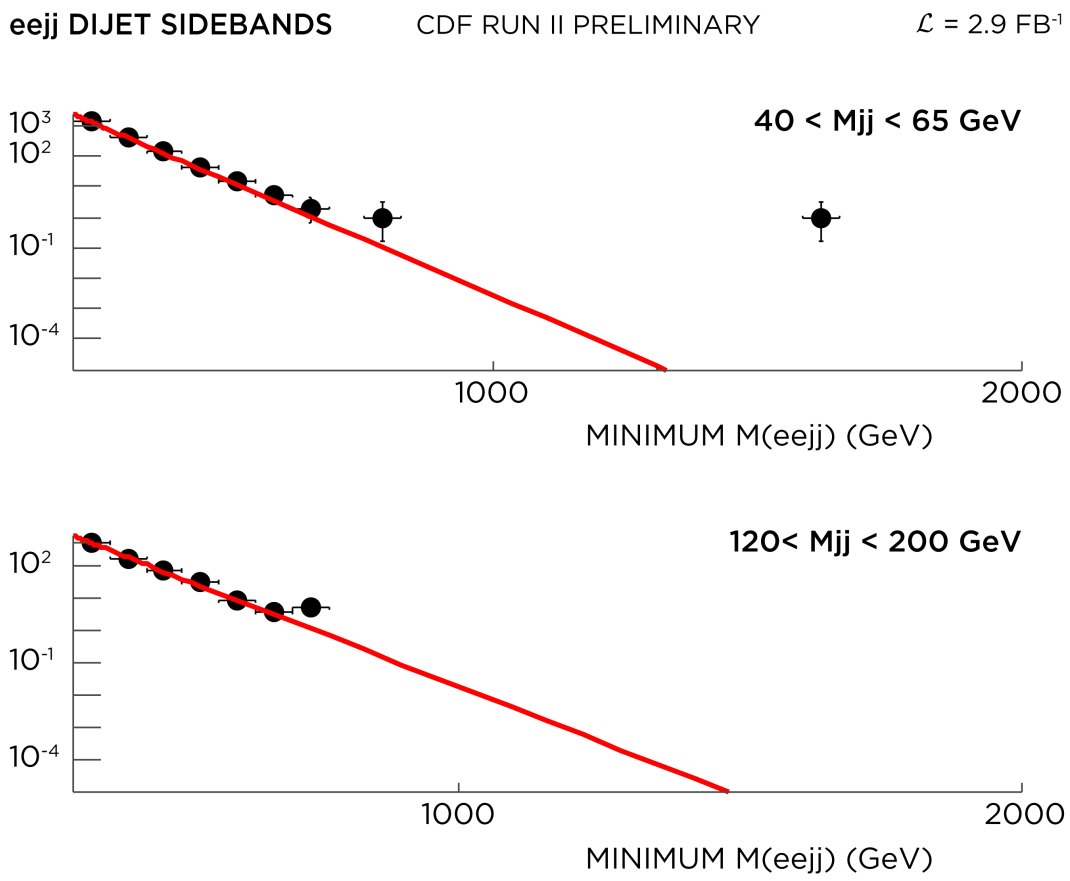

Figure 5.30: $X \to ZZ \to eejj$ event counts vs $M_X^{\min}$, (top) low M_{qq} and (bottom) high M_{qq} sidebands.

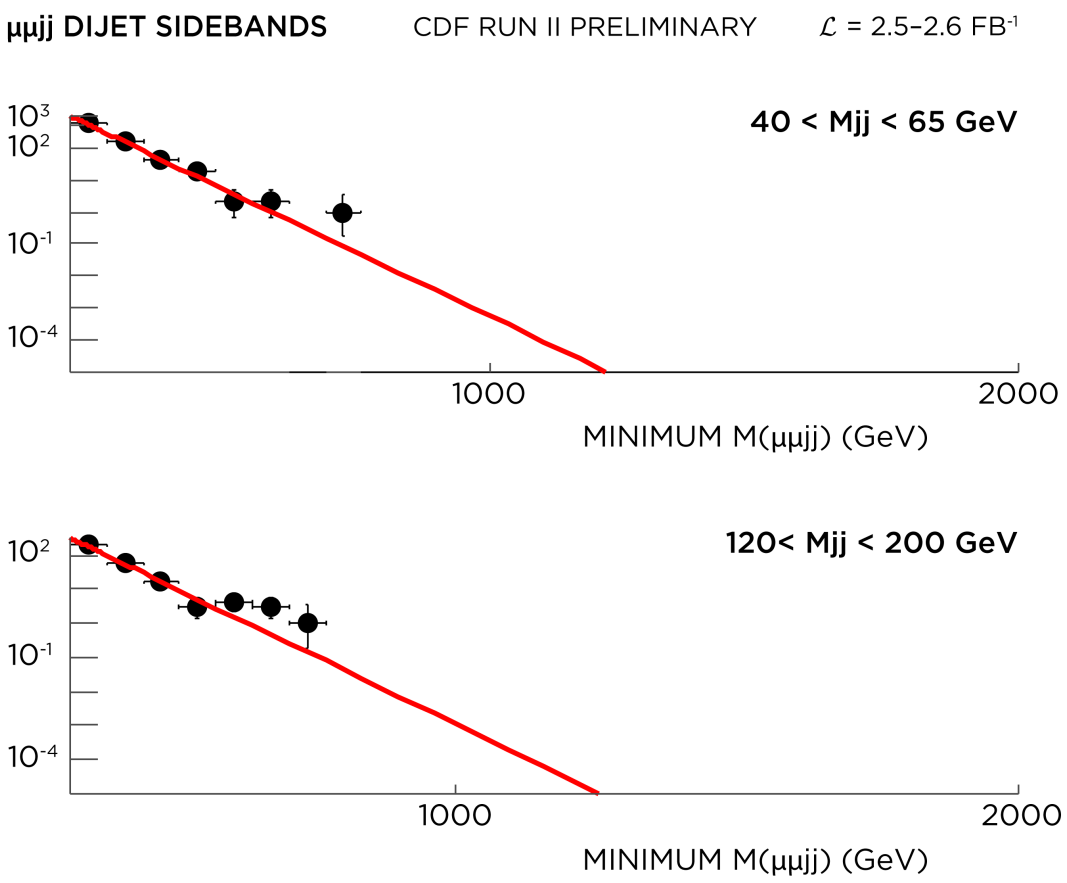

Figure 5.31: $X \to ZZ \to \mu\mu jj$ event counts vs $M_X^{\min}$, (top) low M_{qq} and (bottom) high M_{qq} sidebands.

Signal Mass (GeV)	Prediction
400	483(18)
500	128.0(82)
600	47.4(41)
700	14.9(17)
800	2.86(46)
900	1.75(31)
1000	0.77(16)

Table 5.40: Total $X \to ZZ \to eejj$ background predictions vs $M_X^{\min}$.

Signal Mass (GeV)	Prediction
400	162(11)
500	37.7(44)
600	12.6(20)
700	3.53(72)
800	0.57(16)
900	0.33(10)
1000	0.133(45)

Table 5.41: Total $X \to ZZ \to \mu\mu jj$ background predictions vs $M_X^{\min}$.

Fit cross checks

I test the method on kinematically similar control samples where the actual number of events in the Z window can be inspected:

- Events with two jets, a trigger lepton, and an anti-selected lepton with $\chi^2_Z(Z \to ll) < 5\,\sigma$ (fake M_Z sample).
- Events with two jets, a trigger lepton, and an anti-selected lepton but $40 < M_{ll} < 60$ GeV (fake low M_{ll} sample).
- Events with two jets, a trigger lepton, and an anti-selected lepton but $120 < M_{ll} < 200$ GeV (fake high M_{ll} sample).
- Events with two jets and two leptons but $40 < M_{ll} < 60$ GeV (low M_{ll} sample).
- Events with two jets and two leptons but $120 < M_{ll} < 200$ GeV (high M_{ll} sample).

Note these checks use a slightly different, earlier set of mass ranges than those used for the final limits. This does not affect the conclusion.

In all electron control samples, the method overpredicts the lowest M_X bin. This problem, which would artificially strengthen the resulting limit, comes from non-exponential behavior of the sideband counts at low M_X. To compensate for

M_X^{min} (GeV)	M_X^{max} (GeV)	Prediction	Observed
350	450	1105 ± 29	941
400	600	488 ± 21	540
500	700	95.6 ± 7.2	115
600	800	18.8 ± 2.0	18
650	950	8.31 ± 1.1	8
750	1050	1.64 ± 0.26	3
800	1200	0.73 ± 0.13	2

Table 5.42: Fake M_Z electron sample prediction comparison.

this, the numbers in Section 5.7.3 include an additional systematic uncertainty for the 350–450 GeV bin derived from the difference between the exponential predictions and the observed numbers of events in the sidebands. The interpolation for this M_X range uses the observed numbers of events in the sidebands to avoid overpredicting the background and artificially strengthening the limit [1].

[1]Neither correction is made for the results shown in this section.

M_X^{min} (GeV)	M_X^{max} (GeV)	Prediction	Observed
350	450	23.7 ± 4.0	22
400	600	9.4 ± 2.2	9
500	700	1.48 ± 0.59	2
600	800	0.23 ± 0.15	1
650	950	0.093 ± 0.072	1
750	1050	0.015 ± 0.017	0
800	1200	0.0059 ± 0.0084	0

Table 5.43: Fake M_Z muon sample prediction comparison.

M_X^{min} (GeV)	M_X^{max} (GeV)	Prediction	Observed
350	450	583 ± 26	507
400	600	207 ± 13	228
500	700	26.3 ± 2.8	22
600	800	3.34 ± 0.50	3
650	950	1.19 ± 0.20	2
750	1050	0.152 ± 0.033	0
800	1200	0.055 ± 0.013	0

Table 5.44: Fake low M_{ll} electron sample prediction comparison.

M_X^{min} (GeV)	M_X^{max} (GeV)	Prediction	Observed
350	450	10.0 ± 3.3	13
400	600	4.2 ± 2.1	9
500	700	0.81 ± 0.74	0
600	800	0.17 ± 0.24	1
650	950	0.08 ± 0.13	1
750	1050	0.016 ± 0.041	1
800	1200	0.007 ± 0.023	0

Table 5.45: Fake low M_{ll} muon sample prediction comparison.

M_X^{min} (GeV)	M_X^{max} (GeV)	Prediction	Observed
350	450	1950 ± 59	1487
400	600	1026 ± 48	993
500	700	285 ± 24	230
600	800	79.6 ± 9.9	67
650	950	42.1 ± 6.1	39
750	1050	11.8 ± 2.3	5
800	1200	6.2 ± 1.3	1

Table 5.46: Fake high M_{ll} electron sample prediction comparison.

M_X^{min} (GeV)	M_X^{max} (GeV)	Prediction	Observed
350	450	14.0 ± 3.1	18
400	600	5.8 ± 1.9	14
500	700	1.04 ± 0.62	2
600	800	0.19 ± 0.20	2
650	950	0.08 ± 0.11	2
750	1050	0.016 ± 0.034	1
800	1200	0.007 ± 0.019	0

Table 5.47: Fake high M_{ll} muon sample prediction comparison.

M_X^{min} (GeV)	M_X^{max} (GeV)	Prediction	Observed
350	450	93.0 ± 7.3	49
400	600	35.9 ± 3.9	34
500	700	5.4 ± 1.0	6
600	800	0.83 ± 0.24	3
650	950	0.33 ± 0.12	2
750	1050	0.051 ± 0.026	0
800	1200	0.020 ± 0.012	0

Table 5.48: Low M_{ll} electron sample prediction comparison.

M_X^{min} (GeV)	M_X^{max} (GeV)	Prediction	Observed
350	450	5.9 ± 2.1	4
400	600	2.1 ± 1.1	2
500	700	0.28 ± 0.27	0
600	800	0.040 ± 0.061	0
650	950	0.015 ± 0.028	0
750	1050	0.0022 ± 0.0060	0
800	1200	0.0008 ± 0.0027	0

Table 5.49: Low M_{ll} muon sample prediction comparison.

M_X^{min} (GeV)	M_X^{max} (GeV)	Prediction	Observed
350	450	390 ± 27	262
400	600	234 ± 21	177
500	700	85 ± 11	52
600	800	31 ± 5	14
650	950	18.8 ± 3.9	7
750	1050	6.9 ± 1.9	0
800	1200	4.2 ± 1.3	0

Table 5.50: High M_{ll} electron sample prediction comparison.

M_X^{min} (GeV)	M_X^{max} (GeV)	Prediction	Observed
350	450	50 ± 12	14
400	600	32.4 ± 9.9	10
500	700	13.5 ± 6.1	3
600	800	5.7 ± 3.5	1
650	950	3.7 ± 2.6	0
750	1050	1.6 ± 1.4	0
800	1200	1.01 ± 0.99	0

Table 5.51: High M_{ll} muon sample prediction comparison.

5.7.4 Background summary

Tables 5.52 through 5.57 list the non-resonant background fits and the resonant Standard Model diboson contributions to my blinded signal M_X spectra and four-lepton background normalization regions after correcting simulated events for trigger efficiencies and scale factors. These are the only significant backgrounds. I weight each simulated event by the product of the trigger efficiency and scale factors appropriate for the four-body reconstruction. For example, an event with two triggerable CMUP muons and two PEM electrons has a weight

$$(1-(1-\epsilon_{trigger}^{CMUP})^2)\mathrm{sf}_{id,CMUPtrig}\mathrm{sf}_{id,muon}\mathrm{sf}_{id,PEM}^2\mathrm{sf}_{\Delta z_0}\mathrm{sf}_{\mathrm{cosmic}}\mathrm{sf}_{\mathrm{ZVERTEX}}$$

using the period-averaged numbers obtained from the Z cross section measurements.

Remaining real lepton backgrounds are either non-resonant in the kinematic regions of interest (and thus already addressed) or negligible. For instance, simulation of $t\bar{t} \to ll + qq$ predicts a broadly peaking but negligible contribution of O(100) events to the 12,359 events in the $M_X < 300$ GeV $eeqq$ control region. In the $M_X > 300$ GeV signal region, the $t\bar{t}$ simulation prediction is a factor of 10 lower and non-resonant. Therefore, my background fit includes its contribution.

Mass Bin	SM ZZ	Non-resonant
185–300 GeV	1.9(1)	
400 GeV	0.22(2)	1.31(44)
500 GeV	0.086(7)	0.64(29)
600 GeV	0.045(4)	0.44(18)
700 GeV	0.020(3)	0.28(20)
800 GeV	0.007(1)	0.15(12)
900 GeV	0.005(1)	0.14(11)
1 TeV	0.0032(1)	0.11(10)

Table 5.52: Total *eeee* backgrounds. The 185–300 GeV prediction includes $\chi^2_{ZZ} > 50$ but the other predictions do not. The uncertainty includes the ZZ cross section uncertainty and the statistical uncertainty of the simulation.

Mass Bin	SM ZZ	Non-resonant
185–300 GeV	1.9(1)	
400 GeV	0.19(2)	0.33(13)
500 GeV	0.067(6)	0.128(64)
600 GeV	0.035(4)	0.075(47)
700 GeV	0.014(2)	0.041(29)
800 GeV	0.004(1)	0.019(13)
900 GeV	0.003(1)	0.016(13)
1 TeV	0.0013(6)	0.012(11)

Table 5.53: Total $ee\mu\mu$ backgrounds. The 185–300 GeV prediction includes $\chi^2_{ZZ} > 50$ but the other predictions do not. The uncertainty includes the ZZ cross section uncertainty and the statistical uncertainty of the simulation.

Mass Bin	SM ZZ	Non-resonant
185–300 GeV	0.68(5)	
400 GeV	0.077(7)	0.32(16)
500 GeV	0.027(3)	0.130(77)
600 GeV	0.014(2)	0.078(55)
700 GeV	0.0065(10)	0.044(34)
800 GeV	0.0018(7)	0.021(17)
900 GeV	0.0014(6)	0.018(17)
1 TeV	0.0011(5)	0.014(13)

Table 5.54: Total $\mu\mu ee$ backgrounds. The 185–300 GeV prediction includes $\chi^2_{ZZ} > 50$ but the other predictions do not. The uncertainty includes the ZZ cross section uncertainty and the statistical uncertainty of the simulation.

Mass Bin	SM ZZ	Non-resonant
185–300 GeV	1.00(7)	
400 GeV	0.090(8)	0.21(11)
500 GeV	0.036(4)	0.063(40)
600 GeV	0.018(2)	0.031(23)
700 GeV	0.0082(15)	0.015(13)
800 GeV	0.0018(7)	0.0056(49)
900 GeV	0.00011(5)	0.0046(42)
1 TeV	0.0009(5)	0.0031(30)

Table 5.55: Total $\mu\mu\mu\mu$ backgrounds. The 185–300 GeV prediction includes $\chi^2_{ZZ} > 50$ but the other predictions do not. The uncertainty includes the ZZ cross section uncertainty and the statistical uncertainty of the simulation.

Mass Bin	SM ZZ	SM $W^{\pm}Z$	Non-resonant
400 GeV	5.72(97)	9.4(11)	483(18)
500 GeV	2.43(58)	3.25(46)	128.0(82)
600 GeV	0.99(36)	1.10(22)	47.4(41)
700 GeV	0.19(18)	0.60(16)	14.9(17)
800 GeV	$0^{+0.11}$	0.158(83)	2.86(46)
900 GeV	$0^{+0.11}$	0.095(67)	1.75(31)
1 TeV	$0^{+0.11}$	$0^{+0.067}$	0.77(16)

Table 5.56: Total $eeqq$ backgrounds.

Mass Bin	SM ZZ	SM $W^{\pm}Z$	Non-resonant
400 GeV	2.90(57)	6.04(73)	162(11)
500 GeV	1.30(38)	2.06(32)	37.7(44)
600 GeV	0.57(26)	0.73(17)	12.6(20)
700 GeV	0.26(19)	0.229(93)	3.53(72)
800 GeV	0.09(13)	0.023(40)	0.57(16)
900 GeV	$0^{+0.10}$	$0^{+0.032}$	0.33(10)
1 TeV	$0^{+0.10}$	$0^{+0.032}$	0.133(45)

Table 5.57: Total $\mu\mu qq$ backgrounds.

5.8 Expected limits

Though the four-body mass spectra are my main results, I provide limits on the benchmark RS model as a convenient interpretation of the spectra. The simulated graviton samples in Table 5.4, corrected by the trigger efficiencies and other scale factors from Section 5.6.2, provide the signal expectation for masses $M_G = 200, 300, ..., 1000$ GeV and $k/M_{Pl} = 0.1$ signal. I set the limits in bins of M_X starting at 400 GeV, varying the bin width to accommodate degrading tracker and dijet resolution, along with electron bremsstrahlung, at very high masses. Table 5.58 lists the bins used for each decay channel and M_X. I continuously increase the bin width with M_X to ensure 95% coverage of events in all six channels of signal simulation. For a more precise determination of the anticipated 500 GeV RS graviton mass limit, I add cross section limit calculations at nearby masses (425, 450, and 475 GeV) and interpolate.

Table 5.59 lists the total acceptance times efficiency for each decay mode as a function of M_X. To remove overlap, the $ee\mu\mu$ events which are capable of firing both triggers are assigned to the electron-triggered mode unless only the muon trigger actually fires. I weight the simulation accordingly, using the single-lepton trigger efficiencies discussed in Section 5.6.2. Since it is possible that my signal region events may contain lepton candidates which can be interpreted as either

stubless muons or track electrons, I choose to interpret Z pairings where both leptons are ambiguous as if they are muons.

I calculate the 95%-confidence upper limit on $\sigma_X \times BR(X \to ZZ)$ assuming the number of events observed is the Poisson most probable value for each decay channel using Bayesian statistics and a flat prior ($\sigma_X > 0$), combining all six channels via multiplication of the individual channel likelihoods and treating correlated and uncorrelated systematic uncertainties. For each channel and mass point, I compute a single-channel Poisson likelihood

$$L_\alpha(n_{observed}|\mu(\sigma_{X\to ZZ}, L, \epsilon_{total}, n_{bkg})) = \frac{(\mu(\sigma_{X\to ZZ}, L, \epsilon_{total}, n_{bkg}))^{n_{observed}} e^{-\mu(\sigma_{X\to ZZ}, L, \epsilon_{total}, n_{bkg})}}{n_{observed}!}$$

where

$$\mu(\sigma_{X\to ZZ}, L, \epsilon_{total}, n_{bkg}) = \sigma_{X\to ZZ} L \epsilon_{\text{total}} + n_{\text{bkg}}$$

and α labels the channel. To account for uncertainties, I numerically convolve this likelihood with one Gaussian noise function for each uncertainty, obtaining a smeared mean of

$$\mu(\sigma_{X\to ZZ}, L, \epsilon_{total}, n_{bkg}) = (1+f_1)(1+f_2)...(1+g_1)(1+g_2)...\sigma_{X\to ZZ} L \epsilon_{\text{total}} + n_{\text{bkg}}$$

where f_i (g_i) denotes a Gaussian variate for the i^{th} uncorrelated (correlated) uncertainty and n_{bkg} is Poisson-distributed for the (smeared) mean background

prediction from Section 5.7. The combined likelihood for the six channels is the product

$$L(n^{\alpha}_{observed}|\sigma_{X\to ZZ}, L, \{\epsilon^{\alpha}_{\rm total}\}, \{n^{\alpha}_{\rm bkg}\}) = \prod_{\alpha} \frac{(\mu^{\alpha})^{n^{\alpha}_{observed}} e^{-\mu^{\alpha}}}{n^{\alpha}_{observed}!}$$

of the likelihoods for the individual channels. When evaluating the combined likelihood, the variates $\{g_i\}$ are drawn once per Monte Carlo point and then used for all channels, whereas the variates $\{f_i\}$ are drawn separately for each channel. I then numerically solve

$$\int_0^{\sigma_{95}} L(n^{\alpha}_{observed}|\sigma_{X\to ZZ}, ...)d\sigma_{X\to ZZ} = 0.05 \times \int_0^{\infty} L(n^{\alpha}_{observed}|\sigma_{X\to ZZ}, ...)d\sigma_{X\to ZZ}$$

to obtain the cross section limit σ_{95}.

Tables 5.67 through 5.69 list the expected limits with no systematic uncertainties for certain modes and for the combination. The dijet channels have the highest branching ratio and so dominate the combination at higher M_X where their backgrounds are low. While the four lepton modes add little to the limit at higher M_X, any signal events observed there would be of much more interest than a handful of signal events in the dijet modes. The table also provides the expected limits after including a 5.9% luminosity uncertainty, an uncorrelated 20% acceptance · efficiency uncertainty for each channel, and both Gaussian smearing of the mean background prediction and Poisson fluctuation of the background expectation.

The component systematic acceptance uncertainties have relatively little effect on the limit. For example, the 1.1fb^{-1} *eeee* analysis found the 500 GeV graviton acceptance PDF uncertainty to be 0.4% and the ISR/FSR uncertainty to be 1.0%. I therefore choose to ignore the details of these uncertainties and instead retain the assumption of a 20% uncorrelated uncertainty for each channel (accounting for the combination of PDF, ISR/FSR, lepton/Z ID, and forward tracking uncertainties). I check the uncertainties at 200 and 1000 GeV to ensure they remain small, but otherwise ignore them.

M_X (GeV)	$\lvert\Delta M\rvert$ (GeV)	M_X^{min} (GeV)	M_X^{max} (GeV)
400	70	330	470
425	70	355	495
450	70	380	520
475	70	405	545
500	90	410	590
600	130	470	730
700	160	540	860
800	160	640	960
900	230	670	1130
1000	280	720	1280

Table 5.58: Signal binning.

M_X	A_{eeee}	$A_{ee\mu\mu}$	$A_{\mu\mu ee}$	$A_{\mu\mu\mu\mu}$	A_{eeqq}	$A_{\mu\mu qq}$
400	0.5038(87)	0.3773(61)	0.0596(30)	0.3862(85)	0.3712(58)	0.2923(54)
425	0.5089(84)	0.4024(59)	0.0621(29)	0.3898(83)	0.3790(58)	0.2861(54)
450	0.5295(85)	0.4104(58)	0.0565(27)	0.4150(84)	0.3804(58)	0.2996(55)
475	0.5121(84)	0.4083(59)	0.0577(28)	0.4194(84)	0.3937(59)	0.3214(56)
500	0.5269(88)	0.4293(61)	0.0618(30)	0.4296(87)	0.4089(61)	0.3470(59)
600	0.5519(87)	0.4628(62)	0.0508(27)	0.4700(88)	0.4473(67)	0.3899(66)
700	0.5448(95)	0.4798(68)	0.0481(29)	0.5014(95)	0.4298(61)	0.3834(60)
800	0.5266(85)	0.4719(60)	0.0361(22)	0.4970(84)	0.3895(61)	0.3358(58)
900	0.4860(96)	0.4746(67)	0.0398(26)	0.5230(95)	0.3010(57)	0.2552(54)
1000	0.3767(87)	0.4031(64)	0.0386(25)	0.5137(92)	0.2035(50)	0.2018(50)

Table 5.59: Graviton signal acceptances, with statistical uncertainties only.

Mass (GeV)	Limit (no sys.)				Limit (sys.)
	eeee	$\mu\mu\mu\mu$	*llqq*	Six-Channel Combination	Six-Channel Combination
400	2.2 pb	2.2 pb	515 fb	332 fb	484 fb
500	1.7 pb	2.0 pb	237 fb	181 fb	253 fb
600	1.6 pb	1.9 pb	127 fb	107 fb	153 fb
700	1.6 pb	1.8 pb	84 fb	75 fb	102 fb
800	1.7 pb	1.8 pb	47 fb	43 fb	52 fb
900	1.8 pb	1.7 pb	49 fb	45 fb	53 fb
1000	2.2 pb	1.7 pb	56 fb	50 fb	53 fb

Table 5.60: Expected cross section limits on various graviton masses, for specific channels and the six-channel combination. The six-channel limits are provided without and with smearing the likelihood to account for systematic uncertainties.

5.9 Observed limits

I have unblinded the analysis, observe no significant excess of events in any of the bins from Table 5.58, and so set limits on the RS model. Figures 5.32 through 5.34 show the unblinded mass spectra. Tables 5.61 through 5.66 list the total background predictions and numbers of observed events for the limit-setting bins.

Figure 5.40 displays the observed limit along with the $k/M_{Pl} = 0.1$ RS graviton cross section. Linearly interpolating between the 475 and 500 GeV results, I exclude this graviton below 491 GeV at 95% confidence. Table 5.67 compares the observed and expected limits. Tables 5.68 and 5.69 compare the limits while excluding the dijet and four-lepton channels, respectively.

To aid comparison between the expected and observed limits at each signal mass, I simulate 10,000 experiments using a Poisson-distributed number of pseudo-data drawn from a smooth parameterization of the background expectation as a function of M_X, then construct the interval which contains at least 95% of the resultant limits. Figure 5.39 shows the pseudo-experiment outcomes, and the band shown in Figure 5.40 indicates the intervals.

The observed limit is weaker than the expected limit at the largest masses. The four-lepton limits agree with expectation except for the influence of the

Mass (GeV)	Predicted	Observed
400	1.53(44)	0
500	0.73(29)	0
600	0.49(18)	0
700	0.30(20)	0
800	0.16(12)	0
900	0.15(11)	0
1000	0.11(10)	0

Table 5.61: Predicted and observed *eeee* candidates.

single four-muon signal candidate at 577 GeV and three events at very low M_X, all of which increase the combined limit at several signal masses. The dijet channel limits at higher masses are substantially higher than expectation because of a slight, broad excess of ZZ-like events at most signal masses, appearing predominantly in the electron-triggered channel. To remove correlations between the overlapping signal bins in the observed data, Figures 5.41 and 5.42 show the total background prediction integrated across a set of resolution-dependent but non-overlapping M_X bins, the total background uncertainty, and the observed data.

Mass (GeV)	Predicted	Observed
400	0.52(13)	2
500	0.195(64)	0
600	0.110(47)	0
700	0.055(29)	0
800	0.023(13)	0
900	0.019(13)	0
1000	0.013(11)	0

Table 5.62: Predicted and observed $ee\mu\mu$ candidates.

Mass (GeV)	Predicted	Observed
400	0.397(16)	0
500	0.157(77)	0
600	0.092(55)	0
700	0.050(34)	0
800	0.023(17)	0
900	0.019(17)	0
1000	0.015(13)	0

Table 5.63: Predicted and observed $\mu\mu ee$ candidates.

Mass (GeV)	Predicted	Observed
400	0.30(11)	1
500	0.099(40)	1
600	0.049(23)	1
700	0.023(13)	1
800	0.0074(49)	0
900	0.0047(42)	0
1000	0.0040(30)	0

Table 5.64: Predicted and observed $\mu\mu\mu\mu$ candidates. The same signal candidate appears in the three highest-mass (overlapping) bins.

Mass (GeV)	Predicted	Observed
400	498(18)	456
500	133.7(82)	142
600	49.5(41)	69
700	15.7(17)	28
800	3.02(48)	7
900	1.84(34)	5
1000	0.77(21)	2

Table 5.65: Predicted and observed $eeqq$ candidates.

Mass (GeV)	Predicted	Observed
400	171(11)	143
500	41.1(44)	41
600	13.9(20)	19
700	4.02(75)	4
800	0.68(21)	2
900	0.33(14)	2
1000	0.13(11)	1

Table 5.66: Predicted and observed $\mu\mu qq$ candidates.

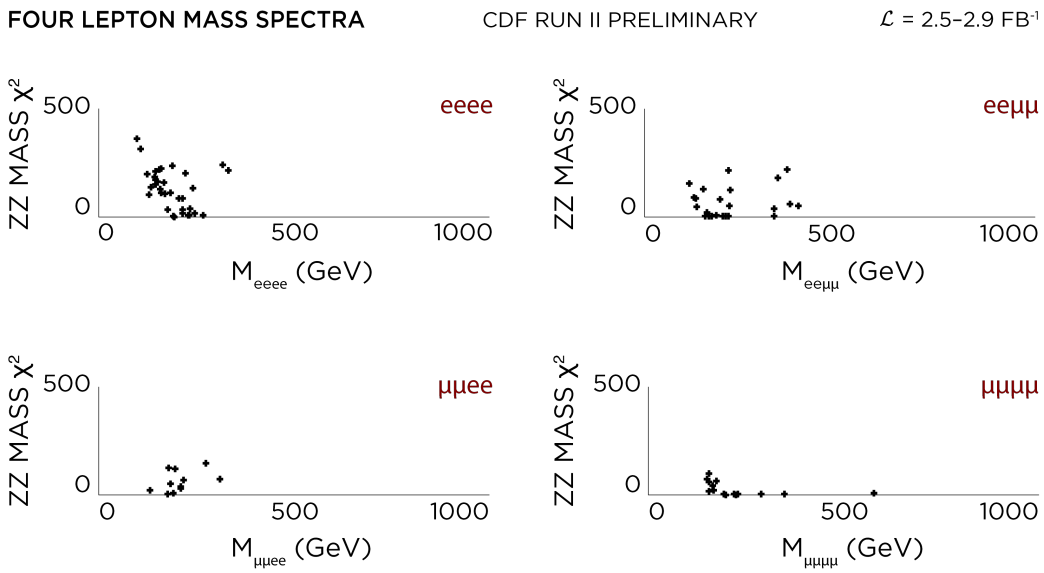

Figure 5.32: Unblinded *llll* χ^2_{ZZ} vs M_{eeee} spectra.

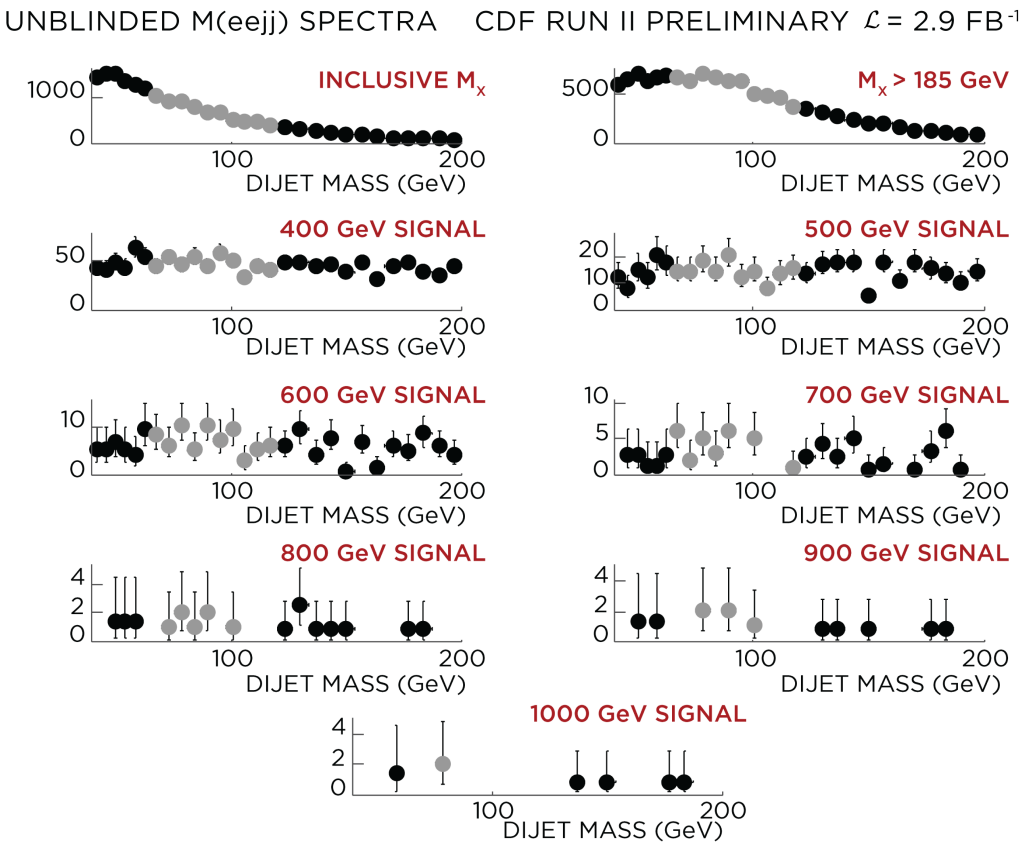

Figure 5.33: Unblinded *eeqq* dijet spectra.

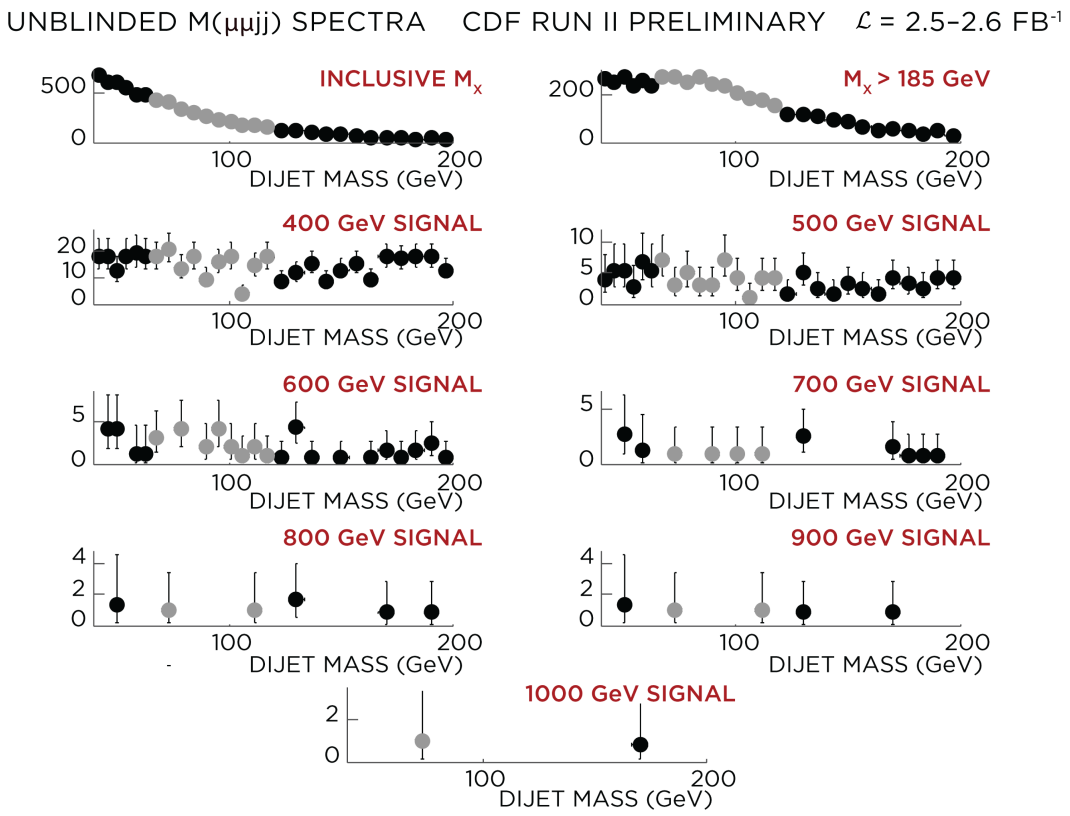

Figure 5.34: Unblinded $\mu\mu qq$ dijet spectra.

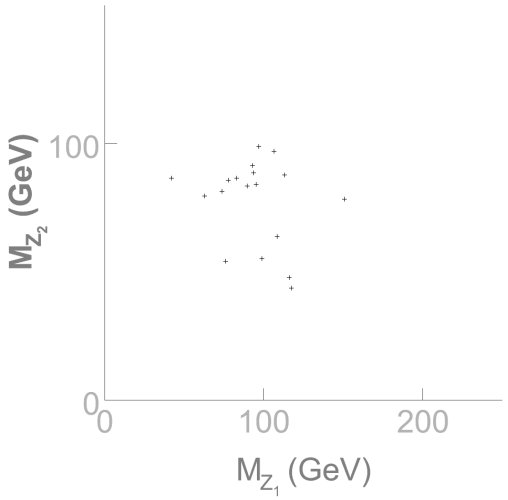

Figure 5.35: Unblinded $eeee$ M_{Z_1} vs M_{Z_2} for $M_X > 185$ GeV.

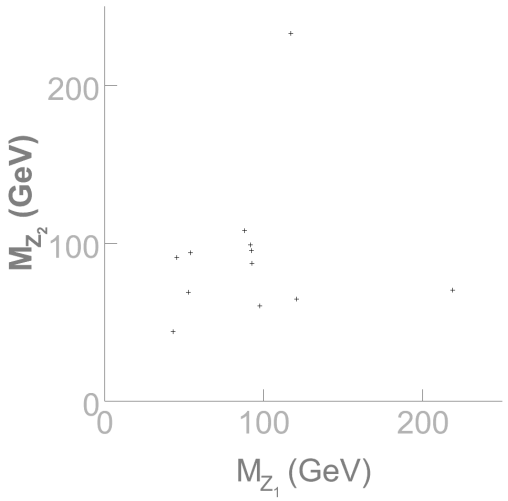

Figure 5.36: Unblinded $ee\mu\mu$ M_{Z_1} vs M_{Z_2} for $M_X > 185$ GeV.

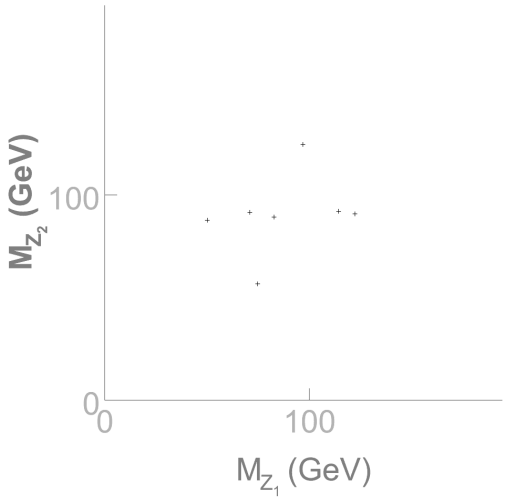

Figure 5.37: Unblinded $\mu\mu ee$ M_{Z_1} vs M_{Z_2} for $M_X > 185$ GeV.

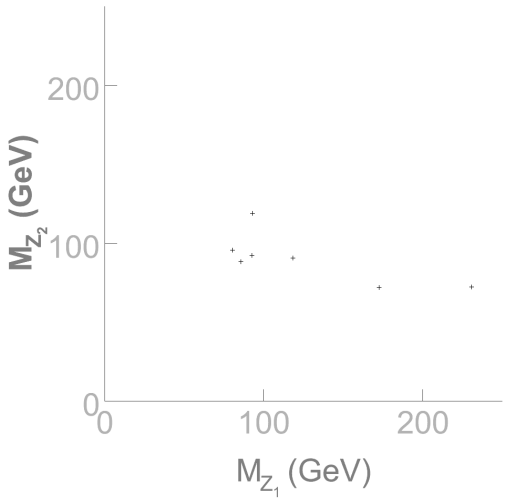

Figure 5.38: Unblinded $\mu\mu\mu\mu$ M_{Z_1} vs M_{Z_2} for $M_X > 185$ GeV.

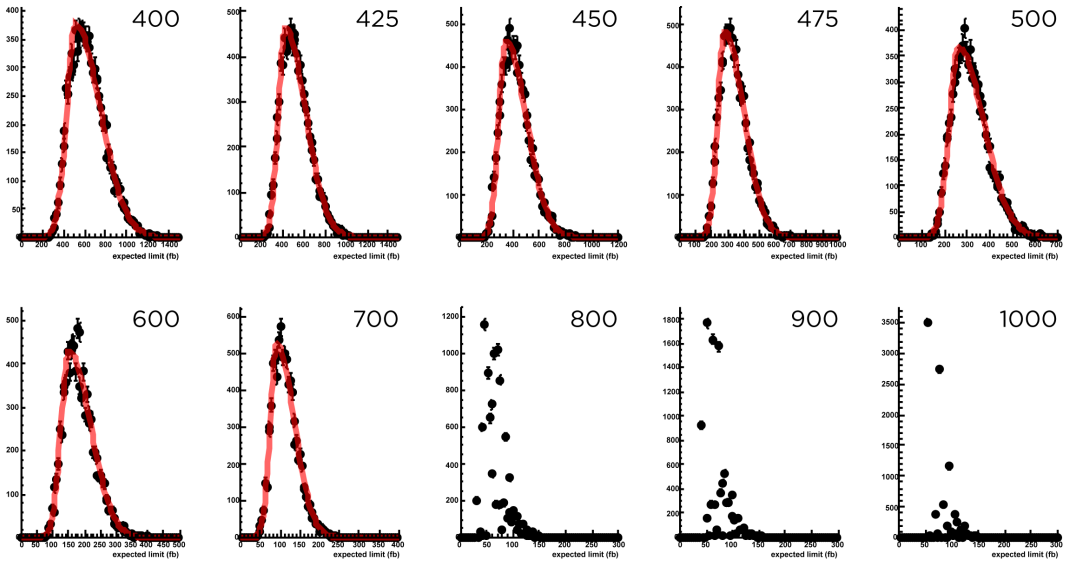

Figure 5.39: Expected limit pseudo-experiments, as described in the text.

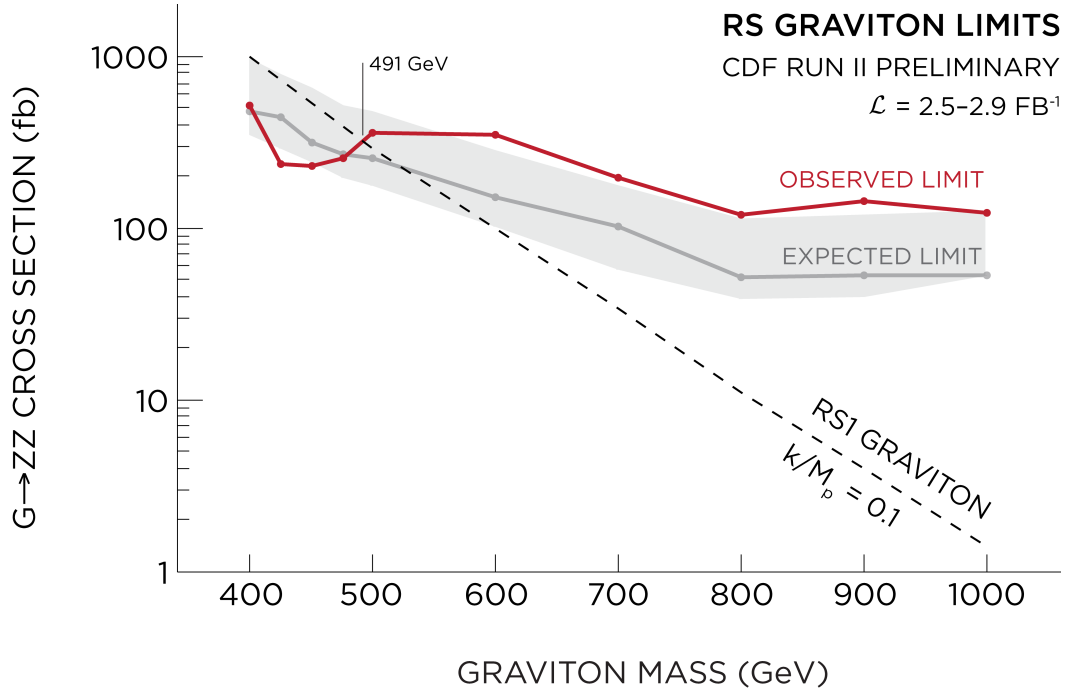

Figure 5.40: Comparison of (red) the observed limit, (blue) the expected limit, and (black) the cross section for a RS graviton with $k/M_p = 0.1$.

Mass (GeV)	Expected Limit	Observed Limit
400	484 fb	525 fb
425	440 fb	236 fb
450	319 fb	232 fb
475	271 fb	258 fb
500	253 fb	361 fb
600	153 fb	348 fb
700	102 fb	197 fb
800	52 fb	120 fb
900	53 fb	143 fb
1000	53 fb	124 fb

Table 5.67: Expected and observed limits.

Mass (GeV)	Four-Lepton Expected Limit	Four-Lepton Observed Limit
400	692 fb	1271 fb
425	687 fb	517 fb
450	503 fb	503 fb
475	507 fb	507 fb
500	488 fb	755 fb
600	462 fb	727 fb
700	451 fb	715 fb
800	464 fb	464 fb
900	465 fb	465 fb
1000	533 fb	533 fb

Table 5.68: Expected and observed limits for the four-lepton channels, including uncertainties.

Mass (GeV)	Dijet Expected Limit	Dijet Observed Limit
400	892 fb	497 fb
425	723 fb	396 fb
450	560 fb	375 fb
475	419 fb	396 fb
500	383 fb	426 fb
600	195 fb	389 fb
700	118 fb	192 fb
800	57 fb	134 fb
900	58 fb	162 fb
1000	59 fb	149 fb

Table 5.69: Expected and observed limits for the dijet channels, including uncertainties.

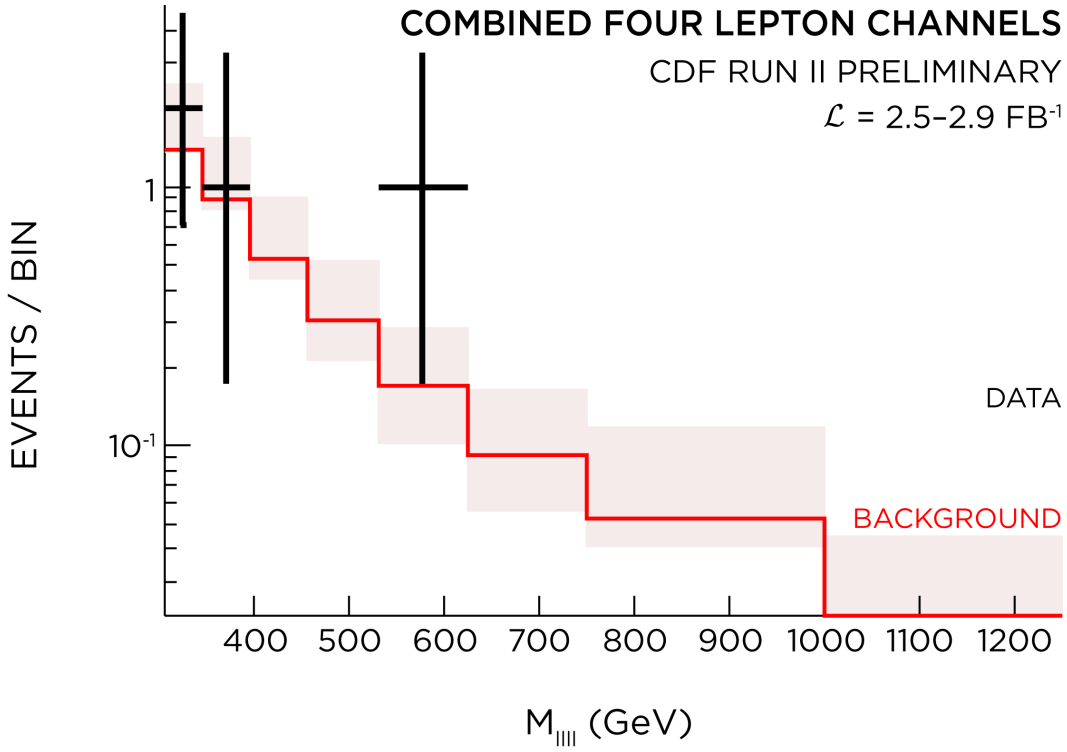

Figure 5.41: Background prediction and observed events, all four-lepton channels combined.

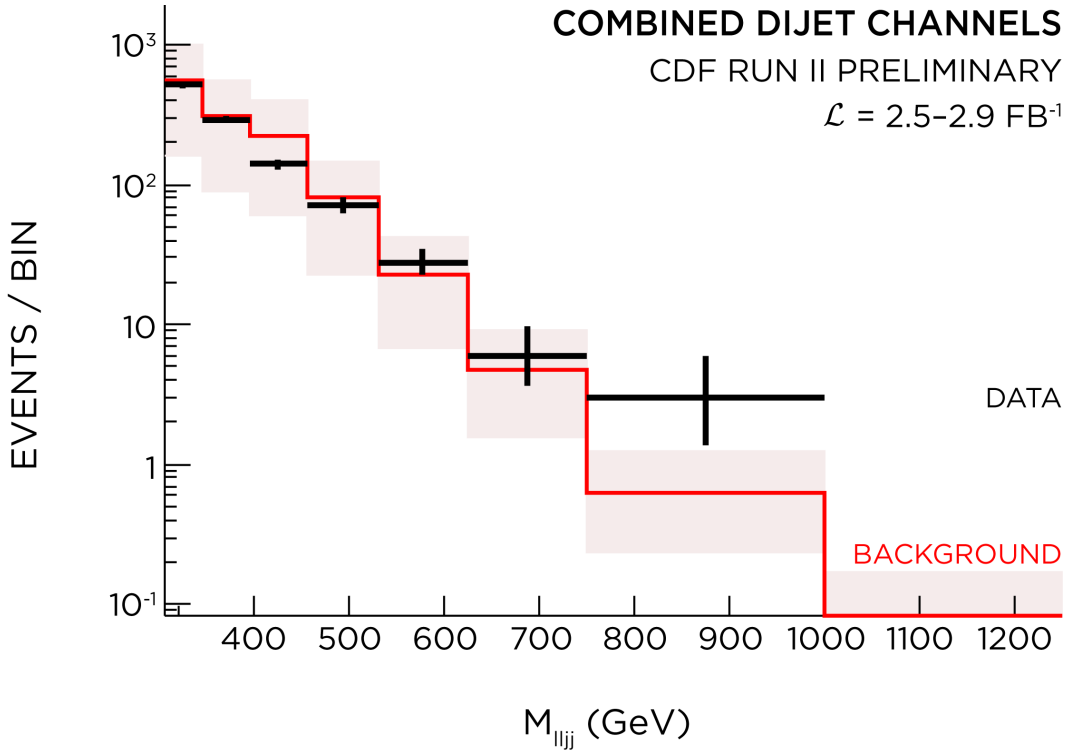

Figure 5.42: Background prediction and observed events, both dijet channels combined.

5.9.1 Investigation of signal candidates

The highest M_X four-lepton candidate is a four-muon candidate with $M_X \approx$ 577 GeV which falls in three limit-setting bins (see Table 5.64) and is consistent with the non-resonant background estimate[1] in all of the three. Inspection does not support a signal hypothesis. The trigger muon is a well-measured central Outside-In track, two of the tracks are backward tracks, and the remaining leg of the recoil Z candidate[2] is a silicon-driven Inside Out track with $p_T = 280$ GeV (see Figure 5.43). While the COT, ISL, and SVX hit data are compatible with the existence of this track, the track fit covariance matrices for this and the other two forward tracks in the event indicate they are poorly measured. Moreover, the analysis selection yields no other objects that could balance the IO track's conspicuously large transverse momentum. Thus, the high M_X is likely the result of mismeasuring the IO track.

One should also note the population of events with $300 < M_X < 350$ GeV. These do not resemble signal either. Figure 5.44 shows the highest M_X event from the $ee\mu\mu$ channel in Figure 5.32 (the $M_X = 393$ GeV and $\chi^2_{ZZ} = 50.2$

[1]Note that the anti-selected lepton samples automatically include the appropriate contribution from mismeasured tracks.

[2]The "recoil" Z candidate does not contain the trigger lepton.

candidate). The two muon candidates have $|\Delta\eta| = 2.71$ but also have $|\Delta\phi_0| = 0.06$ and the same charge.

Several subsequent figures show additional interesting high-M_X or low χ^2_{ZZ} candidates.

All signal events are consistent with my background prediction and, upon close inspection, none of the high M_X four-lepton candidates resemble signal.

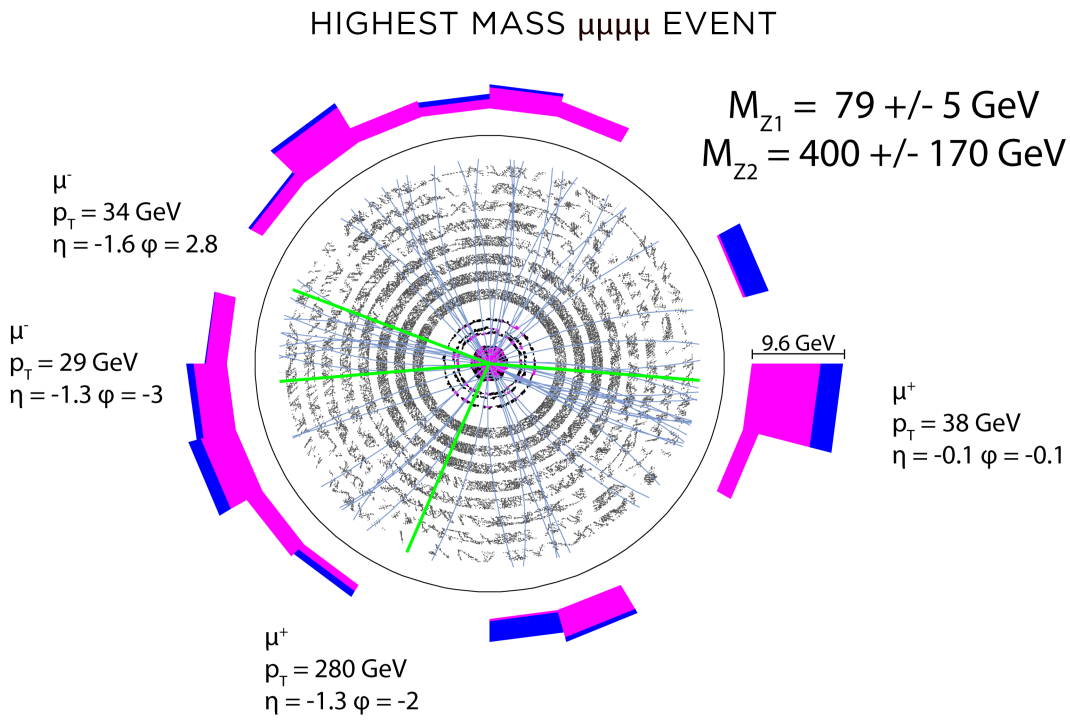

Figure 5.43: Highest mass four muon event. Tracks with $p_T < 1$ GeV are not shown.

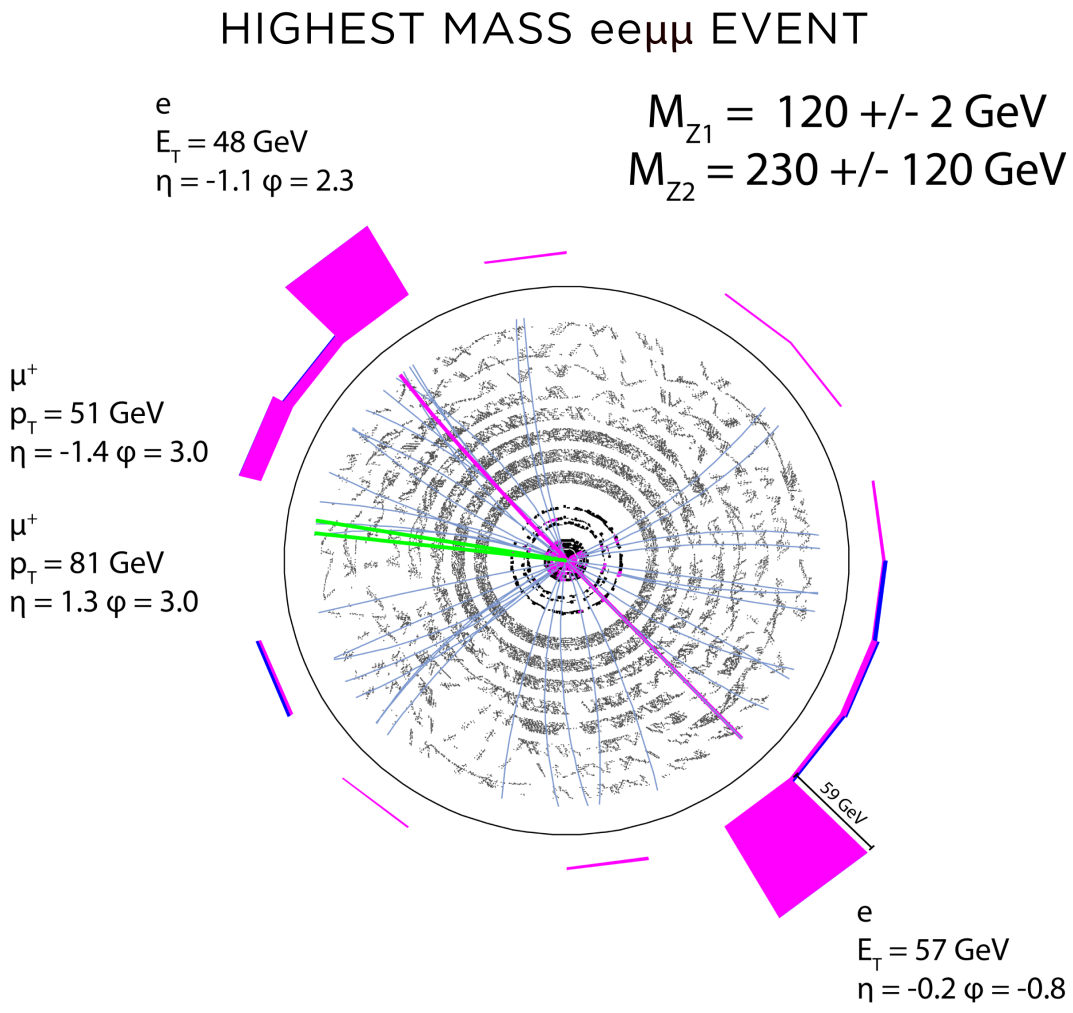

Figure 5.44: Highest mass $ee\mu\mu$ event. Tracks with $p_T < 1$ GeV are not shown.

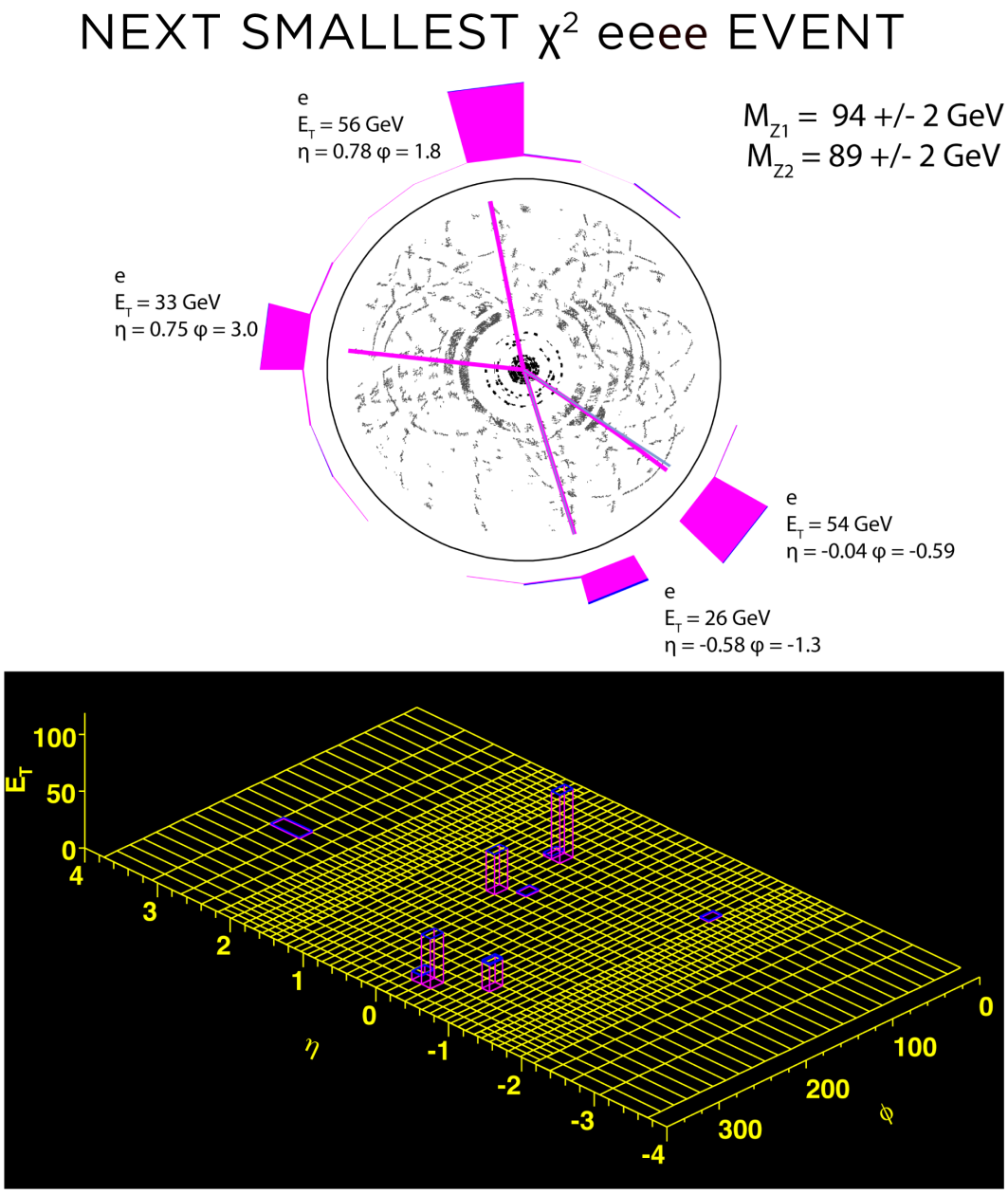

Figure 5.45: A four electron control sample event with $\chi^2_{ZZ} = 0.94$. Towers with $E_T < 1$ GeV and tracks with $p_T < 1$ GeV are not shown.

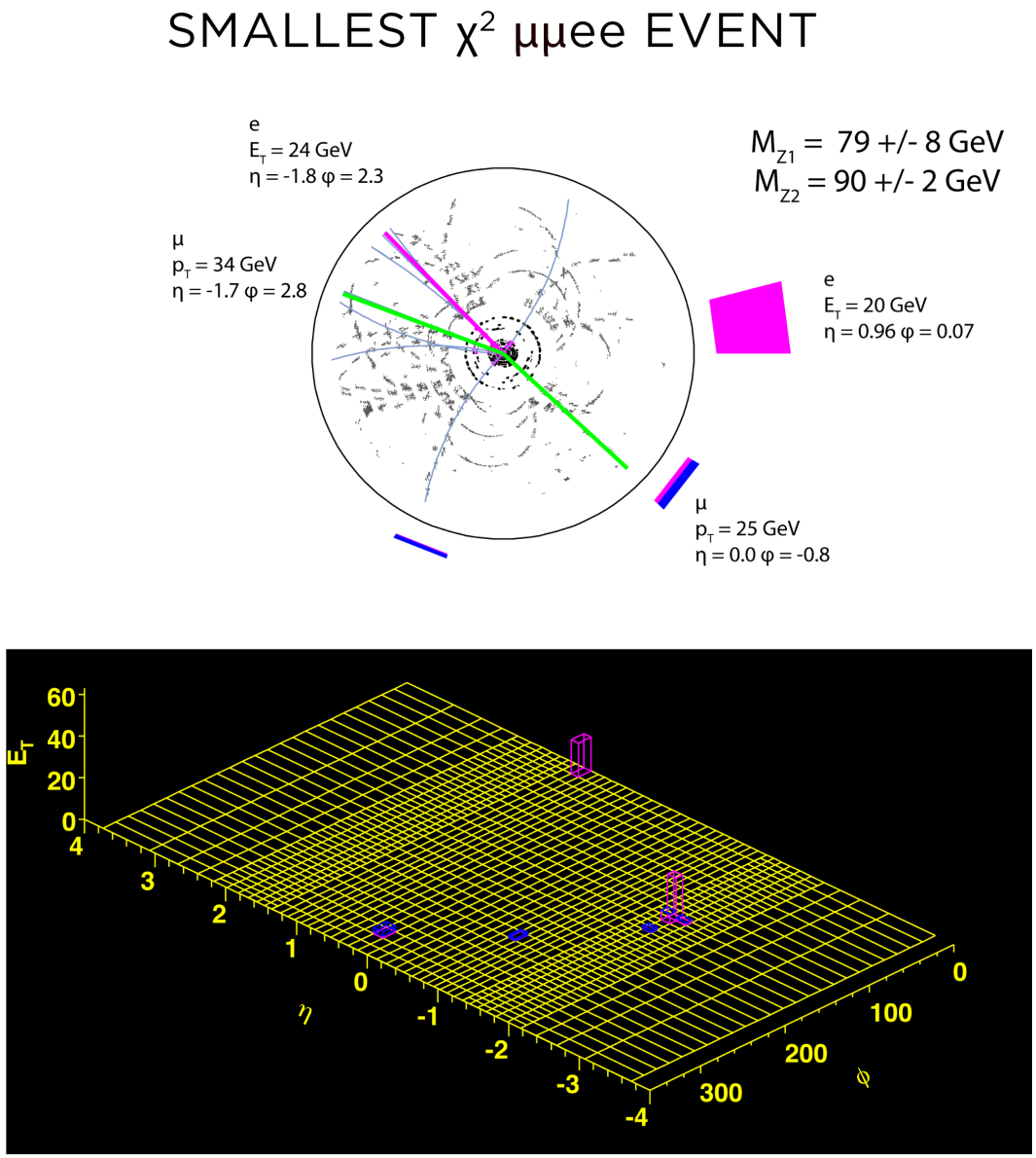

Figure 5.46: A muon-triggered $\mu\mu ee$ control sample event with $\chi^2_{ZZ} = 2.0$. Towers with $E_T < 1$ GeV and tracks with $p_T < 1$ GeV are not shown.

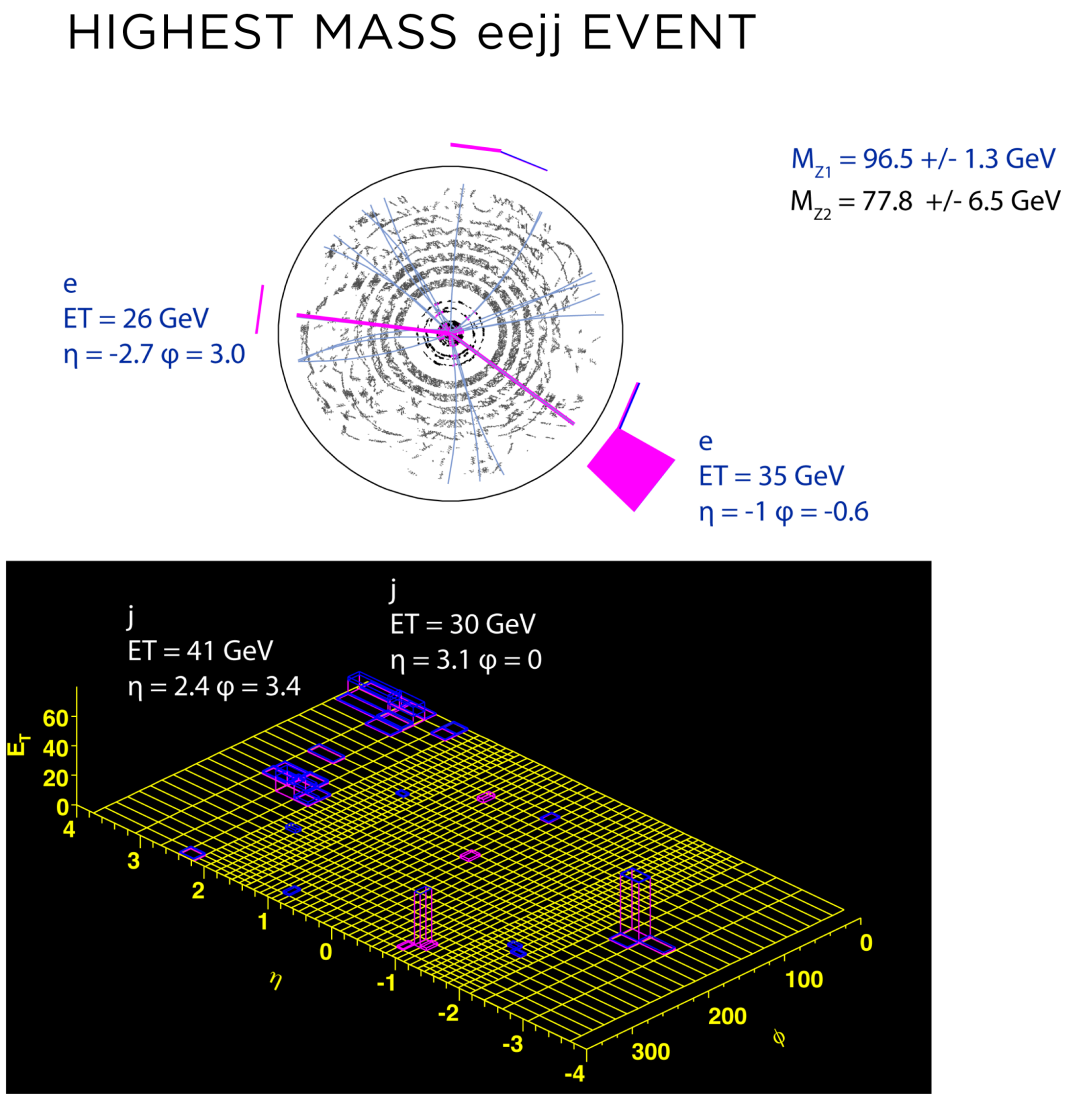

Figure 5.47: The highest M_X electron-triggered dijet candidate. Towers with $E_T < 1$ GeV and tracks with $p_T < 1$ GeV are not shown.

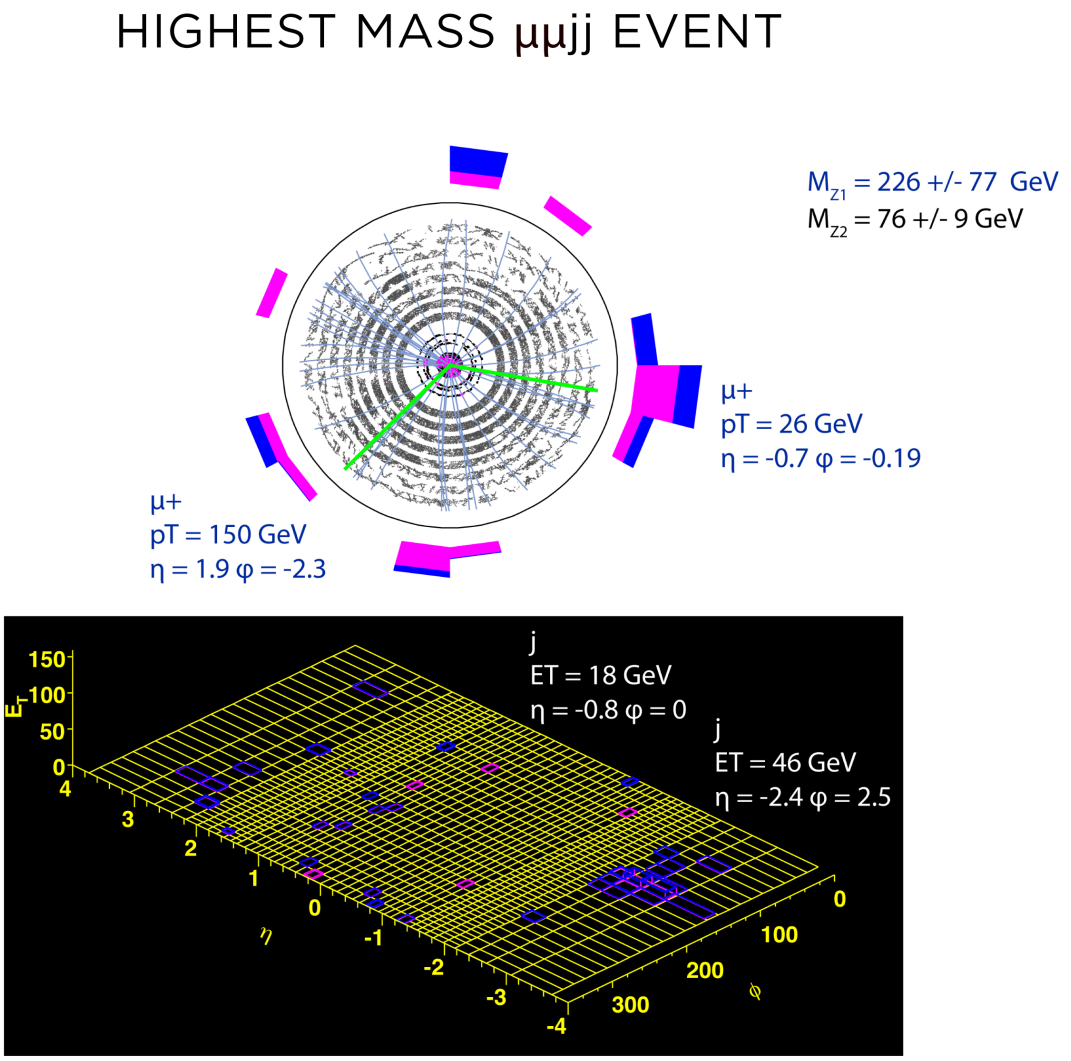

Figure 5.48: The highest M_X muon-triggered dijet candidate. Towers with $E_T <$ 1 GeV and tracks with $p_T < 1$ GeV are not shown.

SM-like low χ^2_{ZZ} candidates

I note in passing that my low M_X control samples contain several excellent newly-identified SM ZZ candidates. For example, after the 1.1 fb^{-1} event noted in the previous iteration of this analysis, the next-smallest χ^2_{ZZ} four-electron candidate is the excellent one shown in Figure 5.45. Combined with the three four-lepton events identified by the published CDF ZZ measurement [33] (and also found in this analysis), these control samples contain more low χ^2_{ZZ} candidates than expected from the SM diboson predictions in Tables 5.52 through 5.55.

Since my analysis does not attempt to predict the background to SM ZZ in the $185 < M_X < 300$ GeV samples, I am not prepared to fully understand whether fake lepton backgrounds can explain the observed numbers of candidates. I leave interpretations of events such as Figure 5.46 to a future dedicated SM ZZ analysis. However, as a crude estimate, I attempt a sideband fit using the same method as the $llqq$ non-resonant background prediction. I select the optimum four lepton combination differently, by minimizing the "trigger Z" pull with the nominal Z boson mass and selecting a "recoil Z" from the remaining two highest E_T leptons, to avoid potentially biasing the recoil Z mass spectrum. Since the dilepton mass resolution is better than the dijet mass resolution, I expand the low sideband to $40 < M_{ll}^{\text{recoil}} < 76$ GeV and the high

sideband to $106 < M_{ll}^{\text{recoil}} < 200$ GeV but otherwise repeat the fit procedure in Section 5.7.3 with the observed numbers of events to obtain a prediction for the $M_X > 185$ GeV, $76 < M_{ll}^{\text{recoil}} < 106$ GeV SM ZZ signal region. Figure 5.49 shows the sideband and signal data. Table 5.70 compares the resulting predictions and the numbers of observed events. The prediction method produces large uncertainties within which the observed results can be considered compatible.

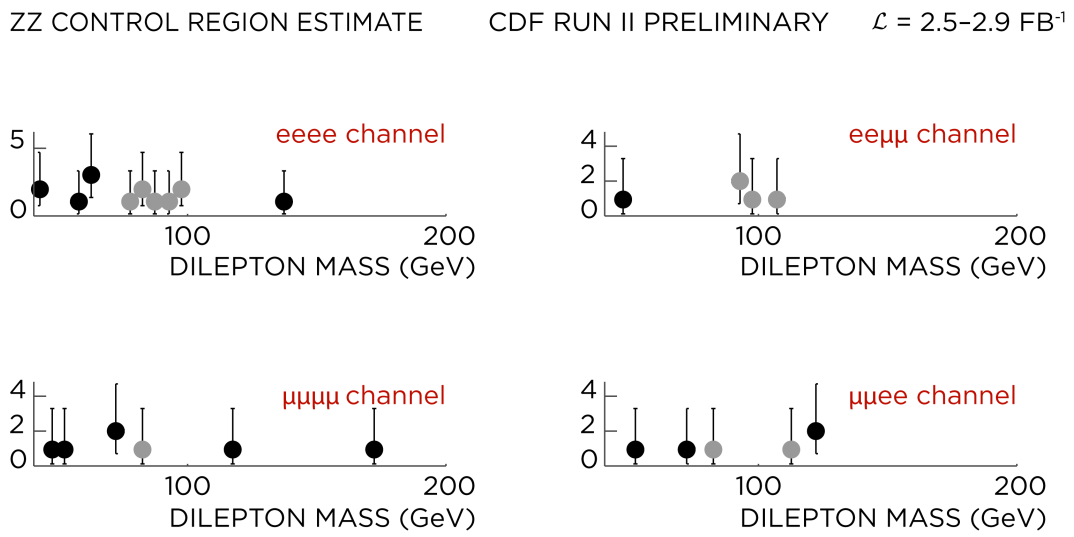

Figure 5.49: Four-lepton sideband and signal data for a crude non-resonant background estimate.

Channel	Non-resonant	ZZ	Total Prediction	Observed
$eeee$	4.3(19)	1.8(1)	6.1(19)	7
$ee\mu\mu$	0.69(78)	1.8(1)	2.49(79)	4
$\mu\mu ee$	1.7(11)	0.64(4)	2.3(11)	2
$\mu\mu\mu\mu$	3.1(16)	0.88(6)	4.0(16)	1

Table 5.70: Four-lepton sideband-method predictions for the $M_X > 185$ GeV, $76 < M_{ll}^{\text{recoil}} < 106$ GeV SM ZZ region and observed numbers of events.

Chapter 6

Conclusion

This thesis documents a search for a narrow ZZ resonance in 2.5–2.9 fb^{-1} of CDF data via decays to electrons, muons, and jets. I find no evidence for the resonance. Using the acceptance of a benchmark model (massive gravitons), I set limits on resonances which are 8–34 times stronger than 1.1 fb^{-1} published result, itself a product of this thesis work and previously the world's best direct limit on high mass ZZ resonances. I exclude RS graviton resonances below 491 GeV at 95% confidence. For uniform graviton couplings, this limit is not competitive with similar searches in the diphoton and dilepton final states because of the $O(10^{-1})$ branching fraction penalty incurred in $Z \to ll$ decays, but, as a widely-available benchmark, it serves as a convenient way to communicate the result to

the broader community. The limit also augments the other searches in bulk RS scenarios with modified graviton couplings.

The analysis described herein also serves to pioneer use of the heavily-revised suite of CDF tracking software. In particular, it validates the software with key physics signals, demonstrates its use, and measures the increased efficiency for $1.3 < |\eta| < 1.7$ tracking with the new backward algorithm.

Bibliography

[1] Particle Data Group. Review of particle physics. *Physics Letters B*, 667:1, Sep 2008.

[2] CDF Collaboration. Global search for new physics with 2.0/fb at CDF. *arXiv*, hep-ex, Sep 2008.

[3] J J Thomson. *Philosophical Magazine*, 44:293, 1897.

[4] J J Thomson. *The Electrician*, 39:104, 1897.

[5] Carl D Anderson. The positive electron. *Physical Review*, 43:491, Mar 1933.

[6] J C Street and E C Stevenson. New evidence for the existence of a particle of mass intermediate between the proton and electron. *Physical Review*, 52:1003, Nov 1937.

[7] M L Perl et al. Evidence for anomalous lepton production in e^+ e^- annihilation. *Physical Review Letters*, 35:1489, Dec 1975.

[8] C L Cowan, F Reines, F B Harrison, H W Kruse, and A D McGuire. Detection of the free neutrino: A confirmation. *Science*, 124:103, Jul 1956.

[9] G Danby, J-M Gaillard, K Goulianos, L M Lederman, N Mistry, M Schwartz, and J Steinberger. Observation of high-energy neutrino reactions and the existence of two kinds of neutrinos. *Physical Review Letters*, 9:36, Jul 1962.

[10] DONUT Collaboration. Observation of tau neutrino interactions. *Physics Letters B*, 504:218, Apr 2001.

[11] M Gellmann. A schematic model of baryons and mesons. *Physics Letters*, 8:214, Feb 1964.

[12] H R Rubinstein and H Stern. Nucleon-antinucleon annihilation in the quark model. *Physics Letters*, 21:447, Jun 1966.

[13] C G Callan and David J Gross. High-energy electroproduction and the constitution of the electric current. *Physical Review Letters*, 22:156, Jan 1969.

[14] J Chadwick. Possible existence of a neutron. *Nature*, 129(3252):312, Jul 1932.

[15] C Lattes, G Occhialini, and C Powell. Observations on the tracks of slow mesons in photographic emulsions. *Nature*, 160(4067):486–492, May 1947.

[16] C Lattes, G Occhialini, and C Powell. Observations on the tracks of slow mesons in photographic emulsions. *Nature*, 160(4066):453–456, May 1947.

[17] G D Rochester and C C Butler. The penetrating particles in cosmic-ray showers: I. heavily-ionizing particles. *Proceedings of the Physical Society*, 61:307, Oct 1948.

[18] J J Aubert, U Becker, P J Biggs, J Burger, M Chen, G Everhart, P Goldhagen, J Leong, T McCorriston, T G Rhoades, M Rohde, Samuel C Ting, Sau Lan Wu, and Y Y Lee. Experimental observation of a heavy particle *J*. *Physical Review Letters*, 33:1404, Dec 1974.

[19] J-E Augustin et al. Discovery of a narrow resonance in e^+e^- annihilation. *Physical Review Letters*, 33:1406, Dec 1974.

[20] S W Herb et al. Observation of a dimuon resonance at 9.5 GeV in 400-GeV proton-nucleus collisions. *Physical Review Letters*, 39:252, Aug 1977.

[21] CDF Collaboration. Observation of top quark production in $p\bar{p}$ collisions with the Collider Detector at Fermilab. *Physical Review Letters*, 74:2626, Apr 1995.

[22] D0 Collaboration. Search for high mass top quark production in $p\bar{p}$ collisions at $\sqrt{s} = 1.8$ TeV. *Physical Review Letters*, 74:2422, Mar 1995.

[23] Mark Srednicki. Quantum field theory. *Cambridge Univ. Press*, 2007.

[24] Michael Peskin and Daniel Schroeder. An introduction to quantum field theory. *Westview*, 1995.

[25] Steven Weinberg. The quantum theory of fields. *Cambridge Univ. Press*, 1995.

[26] S Glashow. Partial-symmetries of weak interactions. *Nuclear Physics*, 22:579, Feb 1961.

[27] Steven Weinberg. A model of leptons. *Physical Review Letters*, 19:1264, Nov 1967.

[28] F J Hasert et al. Observation of neutrino-like interactions without muon or electron in the Gargamelle neutrino experiment. *Physics Letters B*, 46:138, Sep 1973.

[29] UA1 Collaboration. Experimental observation of lepton pairs of invariant mass around 95 GeV/c^2 at the CERN SPS collider. *Physics Letters B*, 126:398, Jul 1983.

[30] Sidney D Drell and Tung-Mow Yan. Massive lepton-pair production in hadron-hadron collisions at high energies. *Physical Review Letters*, 25:316, Aug 1970.

[31] CDF Collaboration. Measurements of inclusive W and Z cross sections in $p\bar{\mathrm{p}}$ collisions at $\sqrt{s} = 1.96$ TeV. *Journal of Physics G*, 34:2457, Dec 2007.

[32] J M Campbell and R K Ellis. Update on vector boson pair production at hadron colliders. *Physical Review D*, 60:113006, Dec 1999.

[33] CDF Collaboration. Strong evidence for ZZ production in $p\bar{\mathrm{p}}$ collisions at $\sqrt{s} = 1.96$ TeV. *Physical Review Letters*, 100:201801, May 2008.

[34] D0 Collaboration. Observation of ZZ production in $p\bar{\mathrm{p}}$ collisions at $\sqrt{s} = 1.96$ TeV. *Physical Review Letters*, 101:171803, Oct 2008.

[35] The LEP Collaborations. A combination of preliminary electroweak measurements and constraints on the standard model. *arXiv*, hep-ex, Dec 2006.

[36] H Davoudiasl, J L Hewett, and T G Rizzo. Phenomenology of the Randall-Sundrum gauge hierarchy model. *Physical Review Letters*, 84:2080, Mar 2000.

[37] CDF Collaboration. Search for new heavy particles decaying to $z_0 z_0 \rightarrow eeee$ in $\mathrm{p}\bar{\mathrm{p}}$ collisions at $\sqrt{s} = 1.96$ TeV. *Physical Review D*, 78(1), Jul 2008.

[38] Peter J Mohr, Barry N Taylor, and David B Newell. CODATA recommended values of the fundamental physical constants: 2006. *Rev. Mod. Phys.*, 80:633, Apr 2008.

[39] Yung-Su Tsai. Pair production and bremsstrahlung of charged leptons. *Review of Modern Physics*, 46:815, Oct 1974.

[40] E D Bloom, D H Coward, H Destaebler, J Drees, G Miller, L W Mo, R E Taylor, M Breidenbach, J I Friedman, G C Hartmann, and H W Kendall. High-energy inelastic e-p scattering at 6 ° and 10 °. *Physical Review Letters*, 23:930, Oct 1969.

[41] UA2 Collaboration. Observation of very large transverse momentum jets at the CERN $p\bar{p}$ collider. *Physics Letters B*, 118:203, Dec 1982.

[42] Jeffrey Goldstone. *Nuovo Cimento*, 19:154, 1961.

[43] Jeffrey Goldstone, Abdus Salam, and Steven Weinberg. Broken symmetries. *Physical Review*, 127:965, Aug 1962.

[44] P W Higgs. Broken symmetries, massless particles and gauge fields. *Physics Letters*, 12:132, Sep 1964.

[45] Peter W Higgs. Spontaneous symmetry breakdown without massless bosons. *Physical Review*, 145:1156, May 1966.

[46] Peter W Higgs. Broken symmetries and the masses of gauge bosons. *Physical Review Letters*, 13:508, Oct 1964.

[47] F Englert and R Brout. Broken symmetry and the mass of gauge vector mesons. *Physical Review Letters*, 13:321, Aug 1964.

[48] G S Guralnik, C R Hagen, and T W Kibble. Global conservation laws and massless particles. *Physical Review Letters*, 13:585, Nov 1964.

[49] Chris Quigg. Electroweak symmetry breaking and the Higgs sector. *Acta Phys. Polon.*, B30:2145–2192, May 1999.

[50] ALEPH Collaboration, DELPHI Collaboration, L3 Collaboration, OPAL Collaboration, and The LEP Working Group For Higgs Boson Searches. Search for the Standard Model Higgs boson at LEP. *Physics Letters B*, 565:61, Jul 2003.

[51] The LEP Collaborations. Precision electroweak measurements and constraints on the Standard Model. *arXiv*, hep-ex, Dec 2007.

[52] Tevatron New Phenomena and Higgs Working Group, CDF Collaboration, and D0 Collaboration. Combined CDF and dzero upper limits on Standard Model Higgs boson production at high mass (155-200 GeV/c^2) with 3 fb$^-$1 of data. *arXiv*, hep-ex, Aug 2008.

[53] M Herndon for the Babar and CDF and D0 Collaborations. Searches for the higgs boson. *arXiv*, hep-ex, Oct 2008.

[54] F Zwicky. On the masses of nebulae and of clusters of nebulae. *Astrophysical Journal*, 86:217, Oct 1937.

[55] Vera C Rubin and W Kent Ford. Rotation of the Andromeda Nebula from a spectroscopic survey of emission regions. *Astrophysical Journal*, 159:379, Feb 1970.

[56] Douglas Clowe, Maruša Bradač, Anthony H Gonzalez, Maxim Markevitch, Scott W Randall, Christine Jones, and Dennis Zaritsky. A direct empirical proof of the existence of dark matter. *Astrophysical Journal*, 648:L109, Sep 2006.

[57] Adam G Riess et al. Observational evidence from supernovae for an accelerating universe and a cosmological constant. *Astronomical Journal*, 116:1009, Sep 1998.

[58] S Perlmutter et al. Measurements of Omega and Lambda from 42 high-redshift supernovae. *Astrophysical Journal*, 517:565, Jun 1999.

[59] D N Spergel et al. First-year Wilkinson Microwave Anisotropy Probe (WMAP) observations: Determination of cosmological parameters. *Astrophysical Journal Supplement Series*, 148:175, Sep 2003.

[60] Bruce T Cleveland, Timothy Daily, Raymond Davis, James R Distel, Kenneth Lande, C K Lee, Paul S Wildenhain, and Jack Ullman. Measurement of the solar electron neutrino flux with the Homestake Chlorine Detector. *Astrophysical Journal*, 496:505, Mar 1998.

[61] Super-Kamiokande Collaboration. Measurement of atmospheric neutrino oscillation parameters by Super-Kamiokande I. *Physical Review D*, 71:112005, Jun 2005.

[62] K2K Collaboration. Measurement of neutrino oscillation by the K2K experiment. *Physical Review D*, 74:72003, Oct 2006.

[63] MINOS Collaboration. Study of muon neutrino disappearance using the Fermilab Main Injector neutrino beam. *Physical Review D*, 77:72002, Apr 2008.

[64] CDF Collaboration. Search for new particles leading to Z+jets final states in $p\bar{p}$ collisions at $\sqrt{s} = 1.96$ TeV. *Physical Review D*, 76:72006, Oct 2007.

[65] CDF Collaboration. Search for heavy toplike quarks using lepton plus jets events in 1.96 TeV $p\bar{p}$ collisions. *Physical Review Letters*, 100:161803, Apr 2008.

[66] L3 Collaboration. Search for heavy neutral and charged leptons in e^+e^- annihilation at LEP. *Physics Letters B*, 517:75, Sep 2001.

[67] Steven Weinberg. Implications of dynamical symmetry breaking. *Physical Review D*, 13:974, Feb 1976.

[68] Richard P Feynman. The Feynman lectures on gravitation. *Westview*, 1995.

[69] Lisa Randall and Raman Sundrum. An alternative to compactification. *Physical Review Letters*, 83:4690, Dec 1999.

[70] Lisa Randall and Raman Sundrum. Large mass hierarchy from a small extra dimension. *Physical Review Letters*, 83:3370, Oct 1999.

[71] D J Kapner, T S Cook, E G Adelberger, J H Gundlach, B R Heckel, C D Hoyle, and H E Swanson. Tests of the gravitational inverse-square law below the dark-energy length scale. *Physical Review Letters*, 98:21101, Jan 2007.

[72] E G Adelberger, B R Heckel, S Hoedl, C D Hoyle, D J Kapner, and A Upadhye. Particle-physics implications of a recent test of the gravitational inverse-square law. *Physical Review Letters*, 98:131104, Mar 2007.

[73] S Schlamminger, K-Y Choi, T A Wagner, J H Gundlach, and E G Adelberger. Test of the equivalence principle using a rotating torsion balance. *Physical Review Letters*, 100:41101, Feb 2008.

[74] K Dienes. Anomaly-induced gauge unification and brane/bulk couplings in gravity-localized theories. *Nuclear Physics B*, 567(1-2):111–132, Feb 2000.

[75] Benjamin C Allanach, Kosuke Odagiri, Matt J Palmer, M Andy Parker, Ali Sabetfakhri, and Bryan R Webber. Exploring small extra dimensions at the Large Hadron Collider. *Journal of High Energy Physics*, 12:039, Dec 2002.

[76] CDF Collaboration. Search for high-mass diphoton states and limits on Randall-Sundrum gravitons at CDF. *Physical Review Letters*, 99:171801, Oct 2007.

[77] CDF Collaboration. Search for new physics in high-mass electron-positron events in $p\bar{p}$ collisions at $\sqrt{s} = 1.96$TeV. *Physical Review Letters*, 99:171802, Oct 2007.

[78] CDF Collaboration. A search for high-mass resonances decaying to dimuons at CDF. *arXiv*, hep-ex, Oct 2008.

[79] Liam Fitzpatrick, Jared Kaplan, Lisa Randall, and Lian-Tao Wang. Searching for the Kaluza-Klein graviton in bulk RS models. *Journal of High Energy Physics*, 09:013, Sep 2007.

[80] The CDF II Detector Technical Design Report. *FERMILAB-Pub-96/390-E*, 1996.

[81] J D Cockcroft and E T S Walton. Experiments with high velocity positive ions. *Proceedings of the Royal Society of London A*, 129(811):477–489, Nov 1930.

[82] J D Cockcroft and E T S Walton. Experiments with high velocity positive ions. II. the disintegration of elements by high velocity protons. *Proceedings of the Royal Society of London A*, 137(831):229–242, Jul 1932.

[83] J D Cockcroft and E T S Walton. Experiments with high velocity positive ions. I further developments in the method of obtaining high velocity positive ions. *Proceedings of the Royal Society of London A*, 136(830):619–630, Jun 1932.

[84] CDF Collaboration. Measurement of the J/ψ meson and b-hadron production cross sections in p$\bar{p}$ collisions at $\sqrt{s} = 1960$GeV. *Physical Review D*, 71(3), Feb 2005.

[85] A Sill. CDF Run II silicon tracking projects. *Nuclear Instruments and Methods in Physics A*, 447:1, Jun 2000.

[86] Christopher S Hill. Operational experience and performance of the CDFII silicon detector. *Nuclear Instruments and Methods in Physics A*, 530:1, Sep 2004.

[87] A Affolder et al. Intermediate silicon layers detector for the CDF experiment. *Nuclear Instruments and Methods in Physics A*, 453:84, Oct 2000.

[88] T Affolder et al. CDF Central Outer Tracker. *Nuclear Instruments and Methods in Physics A*, 526:249, Jul 2004.

[89] L Balka et al. The CDF central electromagnetic calorimeter. *Nuclear Instruments and Methods in Physics A*, 267:272, May 1988.

[90] S Bertolucci et al. The CDF central and endwall hadron calorimeter. *Nuclear Instruments and Methods in Physics A*, 267:301, May 1988.

[91] M Albrow et al. The CDF plug upgrade electromagnetic calorimeter: test beam results. *Nuclear Instruments and Methods in Physics A*, 480:524, Mar 2002.

[92] S Kuhlmann, H Frisch, M Cordelli, J Huston, R Miller, S Lami, R Paoletti, N Turini, M Iori, D Toback, and F Ukegawa. The CDF calorimeter upgrade

for Run IIb. *Nuclear Instruments and Methods in Physics A*, 518:39, Feb 2004.

[93] G Apollinari, K Goulianos, P Melese, and M Lindgren. Shower maximum detector for the CDF plug upgrade calorimeter. *Nuclear Instruments and Methods in Physics A*, 412(2-3):515–526, Aug 1998.

[94] G Ascoli, L E Holloway, I Karliner, U E Kruse, R D Sard, V J Simaitis, D A Smith, and T K Westhusing. CDF central muon detector. *Nuclear Instruments and Methods in Physics A*, 268:33, May 1988.

[95] D Acosta, S Klimenko, J Konigsberg, A Korytov, G Mitselmakher, A Nguyele, A Nomerotski, A Safonov, R Stanek, D Tsybychev, R Vidal, S M Wang, and M Wong. The CDF cherenkov luminosity monitor. *Nuclear Instruments and Methods in Physics A*, 461:540, Apr 2001.

[96] A Boveia. Status and performance of the CDF Run II silicon detector. *PoS HEP2005*, 377, Jan 2005.

[97] R J Tesarek, S D'Auria, A Hocker, K Kordas, S McGimpsey, and S Worm. A measurement of the radiation environment in the CDF tracking volume. *Nuclear Instruments and Methods in Physics A*, 514:188, Nov 2003.

[98] A Boveia. Radiation damage to the CDF silicon detectors. *FNAL All Experimenters Meeting*, 2005.

[99] Stephen D Ellis and Davison E Soper. Successive combination jet algorithm for hadron collisions. *Physical Review D*, 48(7):3160–3166, Oct 1993.